A TIME-SHARED DUAL OPTICAL TRAP WITH SUB-NANOMETER IMAGE-BASED POSITION RESOLUTION FOR HYBRID INSTRUMENTS

A Dissertation
Presented to the Faculty of the Graduate School
of Cornell University
in Partial Fulfillment of the Requirements for the Degree of
Doctor of Philosophy

by
Jessica Killian
January 2017

A TIME-SHARED DUAL OPTICAL TRAP WITH SUB-NANOMETER IMAGE-BASED POSITION RESOLUTION FOR HYBRID INSTRUMENTS

Jessica Killian, Ph.D.
Cornell University 2017

Optical trapping is a powerful and sensitive technique that enables the direct measurement and manipulation of biological samples on the piconewton and nanometer scales. In examining the evolution and maturation of optical trapping instrumentation in the field of single-molecule biophysics, two main thrusts become apparent: a subset of instruments have aimed to push the limits of resolution, seeking to capture the finest details of biomechanical processes, while a second subset of instruments have explored the integration of optical trapping with other measurement techniques, with the goal of creating multidimensional, hybrid instruments. Unfortunately, many hybrid trapping instruments are forced to sacrifice measurement resolution, or relinquish their measurement capabilities entirely, when the combination of techniques cannot accommodate the stringent demands of traditional optical trapping detection methods. Thus, the full potential of hybrid optical trapping instruments has remained elusive. We have taken on this challenge by developing a highly-versatile optical tweezers instrument that can achieve sub-nanometer position resolution without the use of a second microscope objective, making high-resolution optical trapping measurements uniquely compatible with a broad array of bulky and/or opaque sample-side devices. Our instrument consists of a time-shared, dual

optical trap implemented in an entirely custom-built, free-standing fluorescence microscope, with camera-based position detection. We have developed a robust and accurate set of tracking techniques that allow us to make the first direct measurements of relative bead displacement within an optical trap with sub-nanometer resolution using image tracking. These capabilities pave the way for the next generation of optical tweezer hybrids, which we envision as versatile tools that can integrate multiple measurement modalities and complex substrates without sacrificing resolution, to expand the breadth and clarity of our window into the microscopic and sub-microscopic biological worlds.

BIOGRAPHICAL SKETCH

Jessica Lynn Killian was born in 1984 in San Rafael, CA, and was raised in the small town of Nicasio, CA. She began college at San Jose State University in 2001 but dropped out after one semester. Over the next several years, Jessica became a semi-professional pocket billiards player before foregoing a profession career to return to University in 2004. While completing her undergraduate degrees, Jessica worked in the lab of Dr. Cattien Nguyen at NASA Ames in Mountain View, CA, where she researched the field emission properties of carbon nanotubes. Jessica graduated Cum Laude from SJSU in 2008 with a Bachelor of Science in physics, a Bachelor of Science in chemistry, and a minor in mathematics. Jessica continued her study of physics through the PhD program at Cornell University beginning in the fall of 2008, and joined the laboratory of Dr. Michelle Wang in 2009, specializing in the field of single molecule biophysics and instrumentation. She completed her Master of Science degree in physics in 2012, and graduated with a Doctorate in Philosophy in physics January 2017.

To Alita

ACKNOWLEDGEMENTS

When I decided to join Michelle Wang's lab in 2009, it was in part because of my interest in the exciting research taking place, and in part because I sensed in Michelle a genuine interest in my success, both professionally and personally. Despite a long and often difficult graduate career, that support has always been there, and I am deeply grateful. Her exceptional intelligence, enthusiasm, intuition, and ethic has guided my project and my development as a researcher, and I emerge from my tenure in her lab confident that I have received a scientific training second to none.

My research was accomplished with the support of the other members of the Wang Lab, and it has been a great pleasure to work, grow, and learn with these wonderful young scientists. I must thank Ben Smith and Maxim Sheinin, who mentored my transition into the lab and introduced me to optical trapping instrumentation. James Inman provided years of technical support, and in doing so, equipped me with invaluable practical knowledge in circuits, optics, hardware, and machining. I am tremendously grateful for his help. I also give my sincere thanks to Robert Forties and Lucy Brennan for teaching me most of what I know about molecular biology. Through their help, I learned the skills and assays required to troubleshoot in the wetlab. I thank Mohammad Soltani for his inspiration, kindness,

and support, and Ryan Badman for the same. Tung Le, Fan Ye, and Chuang Tan have all been beyond generous with their time and assistance, and I thank them as well.

The friends I've made during my time in Ithaca have enriched my life in ways I couldn't have imagined when I decided to move three thousand miles away from home. Their companionship and support has seen me through some of the most difficult years of my life. You know who you are. Thank you.

Finally, to my family, who has loved, supported, cheered, and inspired me, I cannot express how much you mean to me. Thank you to my aunts Mary, Marjorie, Melanie, and Margaret, to Memo, to Laura, to Kate, Danny, and Alita, to my sister Jennifer, and most of all to my parents, whom I try every day to be more like.

TABLE OF CONTENTS

LIST OF FIGURES

LIST OF TABLES

1. Introduction

1.1. Optical Trapping

Since optical trapping was first used to manipulate a single strand of DNA in 1994 [Perkins et al. 1994], it has developed into a premier technique in the young field of single-molecule biophysics, owing to its superlative sensitivity, versatility, and speed. An optical trap enables the direct manipulation and measurement of individual biological structures on the piconewton and nanometer scales, a prospect considered fantastical just 50 years ago [Hinterdorfer and Van Oijen 2009]. Complementing traditional ensemble methods, optical traps have yielded groundbreaking discoveries on diverse topics in molecular and cell biology including the mechanochemistry of molecular motors [Mehta et al. 1999; Svoboda et al. 1993], DNA and chromatin mechanics [Bennink et al. 2001; Wang et al. 1997; Wang et al. 1997], DNA enzymatic repair [Bianco et al. 2001], transcription and replication [Johnson et al. 2007; Wang et al. 1998; Yin et al. 1995], and genetic and epigenetic regulation [Hall et al. 2009; Killian et al. 2012].

Briefly, an optical trap refers to the stable potential well formed in three dimensions when a dielectric particle interacts with the large electric field gradient of a tightly-focused beam of light. The resulting force that directs a trapped object towards its energy minimum at the trap center is described in the ray optics regime by

momentum transfer between the trapping light and the particle, in the Rayleigh regime by the interactions between an induced dipole and the surrounding electric field, and in the intermediate regime by Mie scattering theory [Woerdemann 2012]. The trapping potential is harmonic in the vicinity of its energy minimum, and thus within this area, the force F exerted by the trap on a particle scales linearly with the particle's displacement x from the trap center as $F = -kx$, where k is called the trap stiffness. Accordingly, a measurement of a particle's displacement in an optical trap informs on not only the particle's location, but on the forces that are acting upon it to draw it from the trap center.

The principle of optical trapping is applied to the study of biomolecules via the optical tweezers instrument (figure 1.1). In this instrument, a collimated laser beam is directed into the back aperture of a high-numerical-aperture microscope objective lens, creating an optical trap in the microscope's sample plane where the beam is focused to a diffraction-limited spot. Biomolecules of interest are attached to a reporter particle that can be trapped and monitored, typically a polystyrene microsphere, and the biomolecule-reporter-particle system is introduced to the optical trap via a fluid chamber. Figure 1.1 illustrates an example experimental configuration, in which a molecular motor translocating along a strand of DNA is fixed to a microscope coverslip, and one end of the DNA strand is attached to a polystyrene bead held in an optical trap. The motion of the protein relative to the DNA strand is

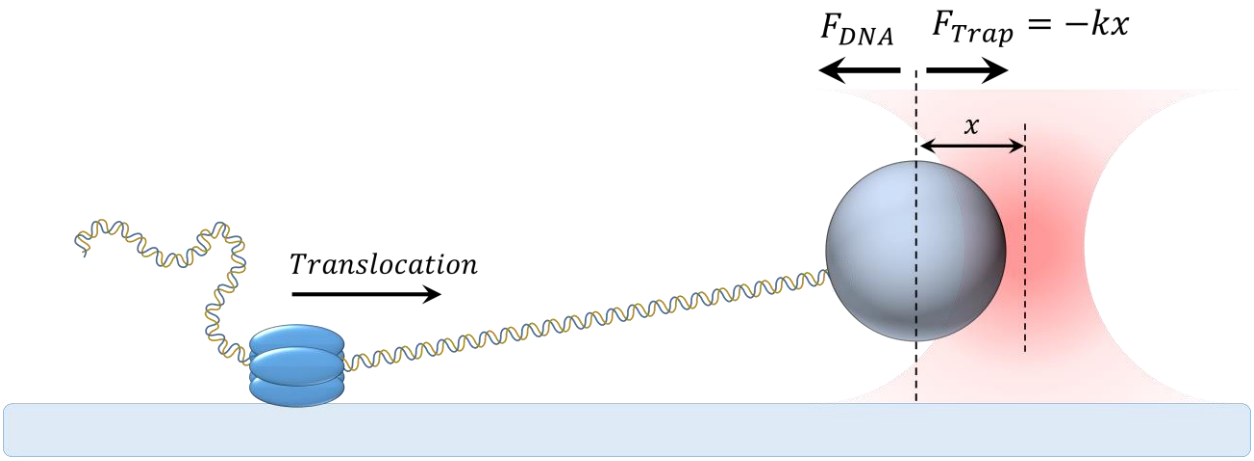

Figure 1.1 – An Experimental Configuration in an Optical Tweezers Instrument
In this cartoon (not to scale), a protein of interest which is translocating along a strand of DNA is shown fixed to a coverslip in a fluid chamber on a microscope. One end of the DNA strand is attached to a polystyrene bead, which is held in an optical trap formed by the microscope's objective lens. The protein converts the chemical energy released during ATP hydrolysis into mechanical work to move along the DNA strand, which acts to draw the bead from the trap center towards the protein. The position of the bead in the trap thus relays the force exerted by the protein on the DNA, and the size of its steps along its DNA substrate.

translated into motion of the bead in the trap, which in turn relays the force exerted by the protein on the DNA, and the size of its steps along its DNA substrate.

It is clear that obtaining a force measurement from an optical trap requires 1) a measurement of the position of a trapped particle relative to the trap center, and 2) a measurement of the trap stiffness k. The first task is traditionally accomplished via the method of back focal plane interferometry (BFPI) [Gittes and Schmidt 1998]. The interactions between the trapping laser and a trapped particle create an interference pattern which registers in the back focal plane of the microscope objective, and in this technique, this pattern is subsequently imaged onto a position sensing photodetector. The resulting signal can be sampled at tens of kilohertz and is sensitive to angstrom-level changes in bead position. Consequently, BFPI has become ubiquitous in the

field [Moffitt et al. 2008]. Once the first task has been met, the second task can be accomplished using one of several different techniques. Perhaps the most straightforward is the application of the equipartition theorem, which dictates that we equate a particle's thermal energy $\frac{1}{2}k_BT$ to its time-averaged harmonic potential energy $\frac{1}{2}k\langle x^2\rangle$ for each axis, where $\langle x^2\rangle$ is the variance of a particle's displacement from equilibrium along the specified axis. If the variance is measured, the trap stiffness is then given by $k = k_BT/\langle x^2\rangle$. This represents the distilled essence of optical trapping; readers interested in a more thorough exposition are directed to a few of the many excellent review articles that have been written on this topic [Neuman and Block 2004].

The last twenty years has seen the application of these principles through instrumentation mature and evolve, both shaping and being shaped by the dynamic field of single-molecule biophysics, with an ever-expanding list of implementations and capabilities. In examining the history of optical trapping instrumentation in single-molecule biophysics, two significant thrusts become apparent: a subset of instruments have aimed to push the limits of resolution and sensitivity, seeking to capture and clarify the finest details of a biological process, while a second subset of instruments have explored the integration of optical trapping with other measurement techniques, creating hybrid instruments capable of yielding complex, multidimensional data on

complex, multidimensional systems. We examine the results of these efforts in the following two sections.

1.2. Dual Optical Trapping: Pushing the Limits of Resolution

The impetus behind the drive towards high resolution optical trapping originates in the characteristic length scales of the systems under investigation. Optical trapping, being a form of force spectroscopy, lends itself particularly to the study of molecular biomechanics occurring on the order of angstroms to nanometers. A common benchmark for the resolution of an optical trap is 3.4 Å, which is the axial length along a double-stranded DNA segment of a single base pair. An instrument that achieves this benchmark can measure the discrete steps taken by the many motor proteins that translocate along DNA one base pair at a time [Abbondanzieri et al. 2005].

Although the method of detection employed by most optical traps, BFPI, is capable of resolving bead displacements on this scale, the measurement may be obscured by the cumulative sources of noise present in an experimental apparatus. Of particular concern among these sources is the mechanical instability between the various physical elements of an instrument, known as "drift." Drift appears as a low-frequency meandering of the laser trap position on the detector at speeds around one

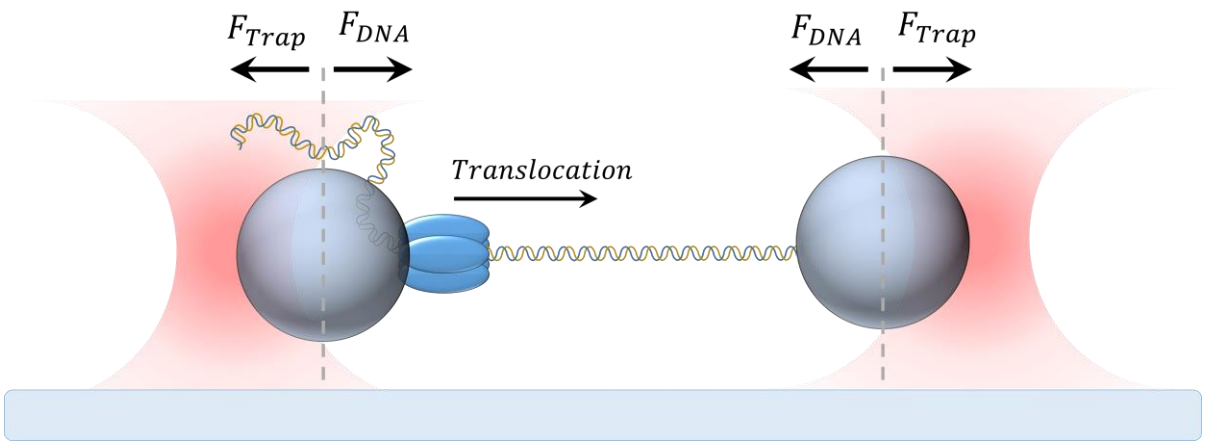

Figure 1.2 – An Experimental Configuration in a Dual Trapping Instrument
A dual optical trap decouples the sample form the drifting microscope stage, improving resolutions and offering more flexibility and control in experimental configurations. Because changes in DNA extension result in antisymmetric bead motion in their respective traps, dual trapping also lowers the noise floor set by Brownian motion. A differential measurement of bead position discards any noise that couples into symmetric bead motion.

nanometer per second, and is indistinguishable from the relative motion of a bead within a trap that an instrument is trying to detect. Because it is not randomly distributed about the mean on the measurement timescales of interest (seconds to minutes), it not only cannot be averaged out, but sets a maximum timescale over which other, higher frequency noise sources can be averaged. In this manner, high frequency noise and low frequency drift act concertedly to globally limit precision.

A dual optical trap describes an optical tweezers instrument in which two traps are formed in the microscope sample plane. A biological sample is held suspended between the traps (figure 1.2), isolating the subject of interrogation from the drifting microscope stage and resulting in a dramatic improvement in stability and measurement resolution. By subtracting out any correlated motion between the

trapped bead pair via a differential measurement, the effects of laser pointing instabilities are mitigated. Moreover, when the trapped beads are connected through a physical linkage such as a DNA strand under tension, the random Brownian motion undergone by each bead within their respective traps becomes partially correlated, lowering the noise floor set by thermal fluctuations [Moffitt et al. 2006]. Dual traps provide greater spatial control of a specimen, promoting more flexibility in experimental arrangements, and providing the opportunity to transport a sample through different buffer conditions. Lastly, by orienting the sample within a plane that is normal to the microscope's optical axis, data analysis is simplified.

The formation of multiple optical trapping centers in the sample plane is most commonly accomplished either by splitting a laser into two orthogonally-polarized beams and sending each into the objective, timesharing a single laser rapidly between two or more positions in the sample plane, or using a spatial light modulator to create and manipulate arbitrary trapping patterns in the sample plane, known as a holographic optical trap (HOT), via programmable phase modulation. While HOT's allow for novel trapping patterns, they remain apart from polarization and timesharing multi-trap techniques in that they cannot achieve the resolution requirements of the more demanding single-molecule measurements [Butterfield et al. 2013].

The formation of a high-resolution dual trap based on polarization, meanwhile, can be implemented with relatively standard equipment (although some employ a

piezo scanning mirror rather than an AOM for enabling spatial control of the traps) and the two traps can be re-separated by polarization for concurrent detection on two standard photodiode sensors. On the other hand, no polarizer possesses an infinite extinction ratio, and the objective lens itself induces a degree of de-polarization, and so crosstalk remains between the orthogonal beams [Mangeol and Bockelmann 2008]. Recombining and aligning the two beams after separation is also nontrivial, and the method cannot accommodate the creation or detection of more than two traps. On the other hand, timesharing eliminates cross-talk between the two beams and simplifies the alignment task, but requires advanced equipment both to modulate the traps at tens of kHz, and to synchronize the modulated traps with a high-bandwidth detector. The oscillatory motion of a sample under tension that results from a time-shared trap also demands consideration.

The lowered noise and improved resolution of dual optical tweezers enabled the first direct measurements of single base-pair stepping in DNA-translocating enzymes [Abbondanzieri et al. 2005; Chemla 2010; Cheng et al. 2011], and has become the gold standard wherever high precision is called for. It has been shown that the absolute noise floor is lower in a differential, dual trap measurement than in its single-trap counterpart for all experimental parameters, and the lower limit to this noise floor set by Brownian motion has been achieved [Moffitt et al. 2006].

1.3. Hybrid Instruments and the Future of Optical Tweezers

The prospect of combining two or more instrumental techniques to provide additional functionalities and complementary measurement modalities has spurred the development of hybrid optical tweezers instruments. Among the first were those combining optical trapping with the visualization of single fluorescent labels [Ishijima et al. 1998]. Figure 1.3 provides a diagram showing how these two techniques may be implemented concurrently on a microscope through the use of dichroic filters. The union of these two preeminent techniques in single-molecule biophysics is natural, as each adds capabilities that the other technique lacks; optical tweezers provide direct mechanical manipulation and measurements of forces and displacements, while single-molecule fluorescence enables additional objects of interest at any point along a DNA template or along a third dimension to be localized and tracked nondestructively, and further lends itself to the study of protein conformational dynamics and binding events [Roy et al. 2008]. Though natural, the combination is not trivial, as the proximity of a trapping laser to an emitting fluorophore is detrimental to fluorophore lifetime. Consequently, the fluorophore is usually separated from the trapping center either spatially via a long DNA template, temporally via interlacing, or both [Joo et al. 2008].

Despite these challenges, both base-pair resolution and single-fluorophore sensitivity have been demonstrated, in one instance using a dual optical trap combined

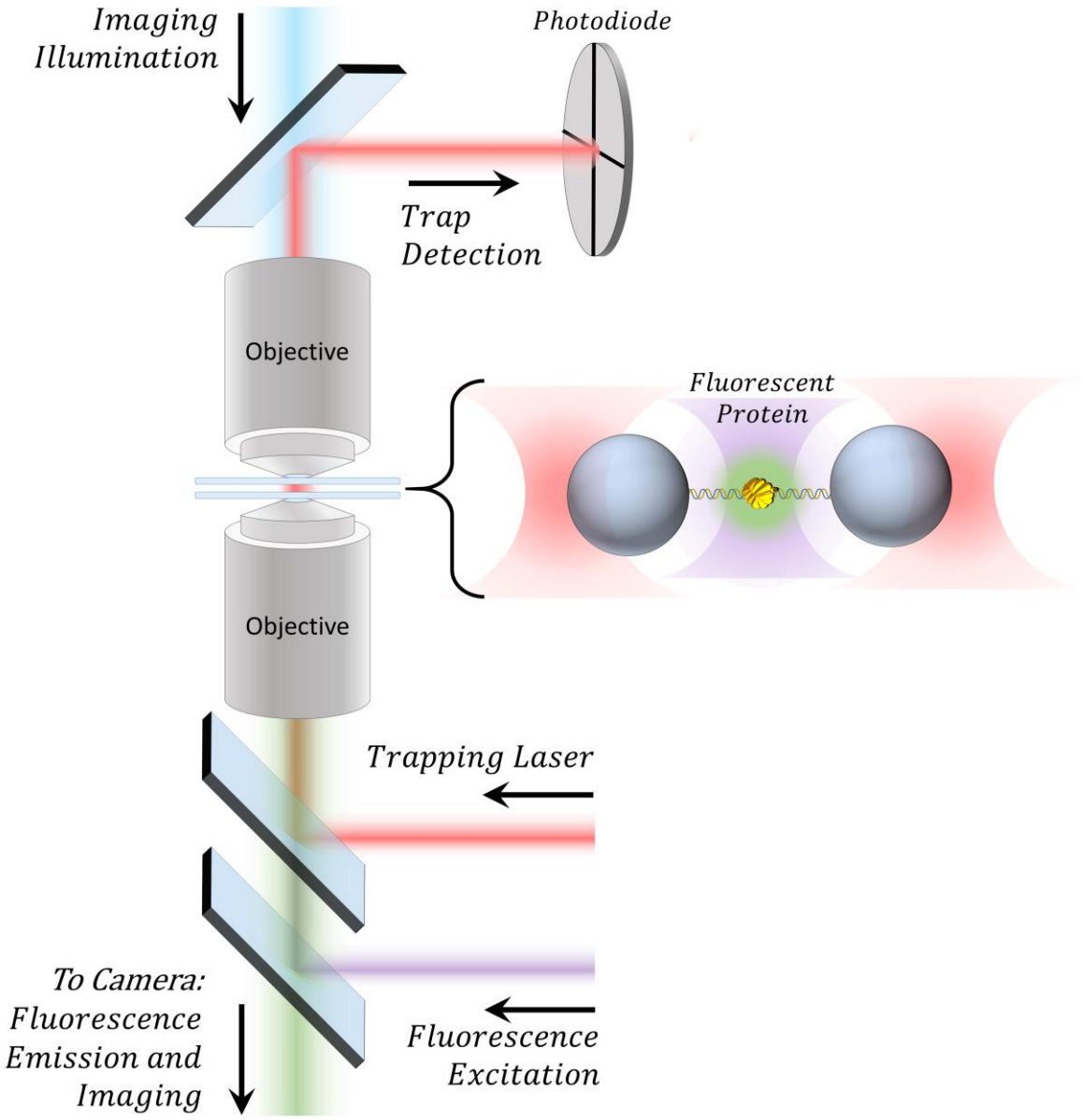

Figure 1.3 – Integrating Microscopy Techniques with Optical Trapping
The IR trapping laser can be combined with and separated from visible wavelengths using dichroic filters which transmit certain wavelengths and reflect others. In standard optical trapping, position and force detection of the trapped beads is performed using the transmitted trapping light. Thus, transmission microscopy techniques like fluorescence are generally compatible with optical trapping with relatively minimal modifications to either configuration.

with confocal fluorescence microscopy [Comstock et al. 2011], and many other advanced combinations such as optical trapping with 3-color Fluorescence Resonance Energy Transfer (FRET) microscopy [Lee and Hohng 2013], and with stimulated

emission depletion (STED) fluorescence microscopy [Heller et al. 2013], have been realized. Indeed, most transmission microscopy techniques are readily combined with optical trapping, as the basic equipment for each is the same, and the IR trapping laser is easily separated from visible microscopy wavelengths via dichroic filters. The integration candidates, however, need not be limited to other microscopy techniques. The array of possible instrument combinations increases exponentially if the spatial constraints imposed by the presence of a second microscope objective are removed.

One such category of hybrid instruments combines the manipulation capabilities of optical tweezers with other spectroscopic techniques. Raman spectroscopy and optical trapping were first combined to study an active biological sample in 2002 [Xie et al. 2002], where it was demonstrated that the Raman spectrum of two different types of live, trapped cells could be distinguished. Since that time, so-called "Raman optical tweezers" have developed into a powerful technique to identify and study cells and other biological samples via flow cytometry [Ahlawat et al. 2016; Casabella et al. 2016]. Other spectroscopic combinations including absorption spectroscopy [Alrifaiy et al. 2015], acoustic force spectroscopy [Thalhammer et al. 2016], and atomic force spectroscopy [van Rosmalen et al. 2015] have been realized. Many of these unique instruments additionally require the concurrent use of advanced microfluidics for introducing and sorting a sample species, or modifying the surrounding buffer environment [Burger et al. 2015; Landenberger et al. 2012].

Another very promising area of integration looks to combine optical tweezers with devices fabricated using lithographic techniques, particularly in the areas of nanophotonics and plasmonics. The ability of such structures to confine, enhance, and guide light into sub-diffraction-limited volumes is of great interest and stands to revolutionize our ability to manipulate and measure sub-microscopic samples [Juan et al. 2011]. Recently, optical tweezers have been integrated with nanofibers to investigate the interactions between particles and evanescent fields [Daly et al. 2016; Gusachenko et al. 2014], and it was shown that optical nanofibers permit the trapping of nanometer-sized particles more readily than standard optical traps. The ability of evanescent fields produced by waveguides [Yang et al. 2009] and plasmonics structures such as bowtie nanoantennas [Berthelot et al. 2014] and photonic crystals [Jing et al. 2016] to trap or move objects has also been of great interest. Previously limited to static trapping or unidirectional transport, full spatiotemporal control of trapped particles along a waveguide has recently been achieved using a Nanophotonic Standing Wave Array Trap (NSWAT), and is already being implemented to manipulate biological samples [Ye et al. 2016].

The integration of optical tweezers with visualization methods like fluorescence is facilitated by the fact that both techniques have native implementations on a standard transmission microscope. The traditional manner of force detection in optical tweezers via the transmitted trapping light through a second microscope

objective is not compromised by the pairing. In contrast, most of the more exotic combinations, including spectroscopic techniques, microfluidics, and plasmonics, require an implementation that directly excludes the use of BFPI for detection, due either to physical constraints (the sample is too large to fit between a pair of objectives) or optical constraints (the sample is opaque or otherwise unconducive to transmission detection). Consequently, the role of optical tweezers in the majority of these hybrid instruments is purely to trap and transport, and their ability to make high-resolution force and position measurements is sacrificed.

Clearly it would be advantageous for a hybrid optical tweezers instrument to retain the full capabilities of the optical trapping technique to resolve sub-piconewton changes in force as well as sub-nanometer displacements. When the use of a second microscope objective is excluded, a different manner of force detection needs to be used. The two prominent alternatives are backscatter detection, which performs BFPI using the light reflected from trapped particles, and direct image tracking with video microscopy.

Backscatter detection is more resistant to drift than the forward-scattered signal, particularly in the axial direction, as a result of the measurement and detection paths sharing an objective and being partially coincident [Sischka et al. 2008]. Aside from this advantage, however, there are several critical obstacles that limit the utility of this technique, particularly for high resolution measurements. The primary culprit is a

simple lack of light; only a small fraction of the trapping laser's power is reflected by a trapped microsphere, leading to a drastic reduction in the signal to noise ratio of a photodiode measurement. This weak signal, furthermore, must be separated efficiently from the incoming trapping laser, as well as from potentially detrimental reflections off any nearby surfaces, before it can be measured [Volpe et al. 2007].

Video microscopy is a flexible option that requires minimal equipment to implement, can more readily track numerous particles, and is not adversely affected by nearby reflective surfaces. However, it has historically been limited to low-bandwidth, low-resolution applications due to the prohibitive costs of high speed cameras, the non-trivial data processing demands, and an overall reduced detection sensitivity [Keen et al. 2007]. The coming-of-age of complementary metal-oxide-semiconductor (CMOS) technologies, however, has made the cost of kilohertz-frame-rate cameras very accessible, and the remaining challenges lie in appropriate illumination to achieve high image quality, and data processing throughput for real-time implementations at ultra-short exposures [Otto et al. 2010]. Video microscopy has recently been demonstrated in the tracking of multiple particles at angstrom resolution and kHz frame rates [Huhle et al. 2015], and can match the performance of BFPI when these conditions are met [Otto et al. 2010].

Multiple groups have implemented these alternative force detection methods when the use of traditional BFPI is excluded. Keyser et al. integrated a single optical

trap with a solid state nanopore and used spatial filtering to enable position detection via the backscattered light, however their accuracy was limited to 5 nm [Keyser et al. 2006]. Although pinhole spatial filtering in reflection-based setups have achieved resolutions as good as 2 nm [Sischka et al. 2008], this configuration cannot match the versatility and precision of a dual trapping instrument. A dual optical trap may be used in opaque samples near reflective surfaces if a slit is used for spatial filtering instead of a pinhole [van Loenhout et al. 2013], but this cannot be extended to additional off-axis particle tracking and is limited in resolution by the low amount of reflected light from the sample relative to interfering reflections from the nearby surface. Although video microscopy has been shown capable of high-bandwidth, angstrom-level detection for fixed objects, it has thus far not been able to resolve nanometer or sub-nanometer displacements of an optically trapped particle relative to its trapping center, nor realized at high resolution in an entirely reflection-based optical trapping instrument. Thus, each of these demonstrated implementations is limited either in their ability to resolve nanometer displacements of trapped objects, or in their ability to be flexibly implemented with a variety of configurations and/or substrates, or both. A truly versatile solution that is compatible with any type of sample-side device while simultaneously incorporating the full spectrum of optical trapping abilities is needed.

As a single-molecule biophysics laboratory, our advanced optical trapping instruments lie at the heart of our research, and our history of innovative

instrumentation and techniques [Inman et al. 2010; Koch et al. 2002; La Porta and Wang 2004; Soltani et al. 2014] keeps us at the forefront of scientific discovery in our field. We see opportunities for the future of optical tweezers instrumentation in the combination of fully-functional, high-resolution dual optical trapping with the burgeoning field of nanophotonics and plasmonics. Therefore, we have developed a unique, highly versatile, and integration-ready dual optical trapping platform that, for the first time, achieves sub-nanometer resolution of optically-trapped particle displacement without the use of a second objective, and is therefore compatible with a vast range of large and/or opaque sample-side devices.

The remainder of this work is organized as follows: in chapter 2, we go over the construction of this instrument in detail, describing the optical layout and addressing important design considerations. In chapter 3, we describe various methods for generating fluorescently-labeled DNA templates for dual-trapping assays. Chapter 4 culminates with a presentation of the instrument implementation, including calibrations, a novel, bias-free detection algorithm to enable highly-accurate image-based particle tracking, an analysis of noise and stability in optical trap position measurements, and a demonstration of instrument data through DNA stretching and unzipping traces.

2. Construction of a Time-shared Dual Optical Trap

We constructed a time-shared, dual optical trap with single-fluorophore sensitivity that uses image tracking to measure sub-nanometer displacements without the use of forward scattered light. The following sections will describe in detail the design and assembly of the instrument. We begin with the physical construction of the optical layout, first of the traps and then of the microscope, including a novel illumination technique for achieving simultaneous ultra-darkfield imaging, optical trapping, and fluorescence. We describe the generation of time-shared optical traps via FPGA modulation of an acousto-optic deflector (AOD) at 50 kHz, and discuss the implications of trap modulation on trap stiffness and measurement resolution. We detail the feedback-stabilization of trap power via a synchronized, high bandwidth photodiode, then outline our techniques for performing highly accurate relative displacement measurements of an optically-trapped particle using video microscopy. We wrap up the chapter with a discussion of our software architecture for enabling independent yet coordinated parallel processing of instrument control and acquisition tasks.

2.1. Constructing the Optical Traps

The Optical Layout

The optical layout is shown in figure 2.1. The optical traps are sourced from a 5 Watt fiber-coupled Nd:YAG laser (IPG Photonics YLR-5-1064-LP). The fiber outputs a linearly-polarized, continuous-wave, zero-order Gaussian beam at 1064 nm with a width of 1.6 mm. The beam first passes through a half-lambda wave plate (HWP) and polarizing beam-splitting cube (PBSC) in order to introduce p-polarized light to an acousto-optic deflector (AOD), which is responsible for creating the two optical traps as well as modulating their amplitudes and positions.

An AOD consists of a crystal and attached piezoelectric transducer. An RF acoustic wave is generated within the crystal by the piezoelectric transducer, creating a sinusoidally-varying index of refraction within the crystal, which acts as a phase grating for an incident laser beam to create a diffraction pattern at the crystal output. When the laser beam is incident at the Bragg angle with respect to the axis normal to the traveling acoustic wave, higher order diffraction spots are minimized and the majority of the deflected light is directed into the first order deflection spot. Modulating the frequency of the RF drive signal applied to the crystal modulates the spacing of the internal diffraction "grating", and thus determines the angle of the deflected beam, and modulating the amplitude of the RF drive signal modulates the

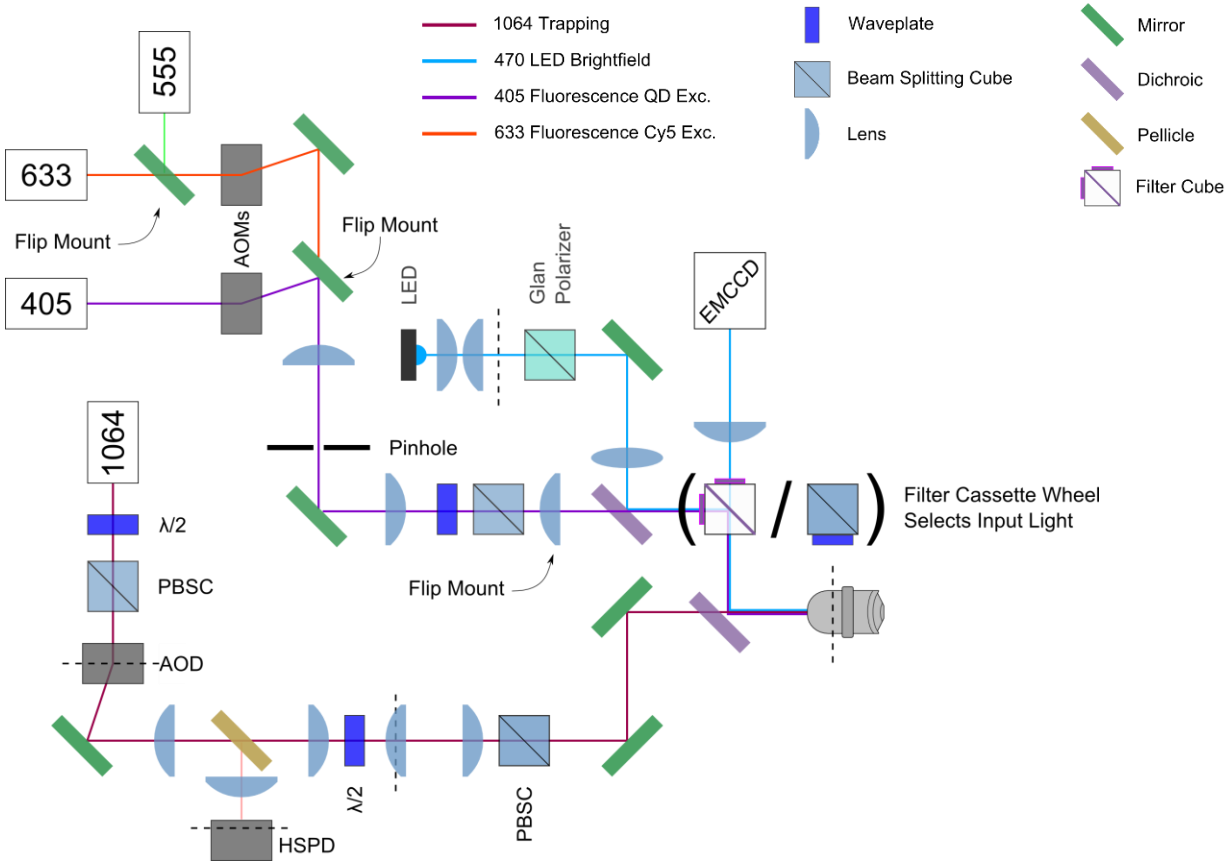

Figure 2.1 – The Optical Layout
The full optical layout of the instrument, built in an entirely free-standing setup without the use of a commercial microscopy body. The 1064 nm trapping laser is modulated by an AOD to create the timeshared optical traps. Power measurements are made by a high speed InGaAs photodiode (HSPD) synchronized to the trap modulation. Position detection is accomplished using video microscopy in either transmission or reflection illumination mode. The setup is also equipped with three fluorescence excitation lasers and an EMCCD camera for single-molecule fluorescence imaging.

fraction of incident light that diffracts into the first order beam, from 0% to a maximum efficiency typically between 80 and 90% of the incident power.

Our AOD [Gooch and Housego (previously Neos) 45035-3-6.5DEG-1.06] accepts an RF signal between 25 and 45 MHz to deflect the beam through an angular range of 32 mrad corresponding to ~18.2 μm of total displacement range in the sample plane. A pair of optical traps is created from a single laser beam via time-

sharing, in which the position of the beam is rapidly switched between two locations in the sample plane. If the trapping laser returns to a given location before a trapped particle leaves the trapping radius, a stable trapping center results with an effective laser power equal to the time-averaged power experienced at that location. This is discussed in more detail in section 2.3.

The angular deflection of the trapping laser produced by the AOD must be transformed into a spatial translation at the trapping location. This is accomplished by mapping the image of the AOD deflection plane to the back focal plane (BFP) of the microscope objective that is used to form the optical traps [Nikon CFI Plan Apo IR SR 60xWI, N.A. 1.27]. An objective lens produces at its front focal plane the Fourier transform of the light incident upon its back focal plane, thus translating variations in the wavevectors k of the incident light into variations in the locations of the resulting focal points in the focal plane. To produce a single optical trap at any given time, the incident light should be collimated so as to be well-described by a single wavevector. To produce the smallest focal point and the stiffest optical trap possible, the collimated incident light should also possess a beam width comparable in size to the back aperture of the high-NA objective in use [Neuman and Block 2004]. Thus the optics between the AOD and microscope objective must map the AOD to the objective BFP, expand the trapping beam to fill or slightly overfill the back aperture

of the objective, create the desired polarization in the trapping beam, and facilitate proper alignment of the trapping beam with respect to the objective.

Expansion, collimation, and mapping are accomplished using a pair of Keplerian telescopes. The first telescope (TS1) collimates the beam and expands it by a factor of 1.4X. TS1 additionally projects an image of the AOD plane 114 mm ahead of its second lens. The first lens of the second telescope is placed at this conjugate plane, and can be translated in the conjugate plane via micrometer screws. Translation of this lens rotates the beam at the objective back focal plane and thus affects the absolute positions of the traps within the sample plane. The second lens of telescope 2 collimates the beam at an expansion factor of 3.9X for a total expansion of 5.5X, bringing the beam diameter from 2.0 mm at the AOD to 11.0 mm at the objective BFP. This provides an overfill factor of 1.1X to the 10-mm objective back aperture. TS2 additionally projects the AOD conjugate plane from its first lens to a plane 498 mm ahead of its second lens, where the objective back focal plane is placed. We verified the locations of both AOD conjugate planes with a quadrant photodiode.

A second HWP and PBSC cleans up the polarization from the AOD and provides polarization control of the traps. To reduce distortion, these optics should be placed where the beam divergence is minimal. Between TS2 and the objective, a periscope is used to direct the expanded and collimated trapping laser into the vertically-oriented objective, giving full control of the lateral displacement and angular

orientation of the trapping beam relative to the objective. The last element the trapping lasers encounter before reaching the objective is a dichroic mirror which is responsible for combining and separating the trapping laser with the imaging and fluorescence paths.

The microscope portion of the setup including the dichroic mirror, objective, and sample stages are held by a vertical breadboard and machined aluminum tabletop. The objective mount is attached to the breadboard by a linear micrometer stage (Newport 460A-X) allowing coarse focus in Z. Above the objective sits the microscope stages. A wide-range translation stage was outfitted with motorized actuators (Zaber T-NA08A25-KT01) with 25 mm of travel along both horizontal axes. Above the wide-range motorized stage, a high precision piezo stage (Physik Instrumente P-517.3CL and driver E-710.4CL) provides 100 μm fine motion control in X and Y with 1-nm precision, and 20 μm motion with 0.1-nm precision in Z. Samples for experiment are mounted atop the PI piezo stage.

2.2. Illumination, Imaging, and Fluorescence

The microscope is equipped with three fluorescence excitation sources, and can operate in fluorescence imaging mode, transparent imaging mode, reflection imaging mode, and a new ultra-darkfield imaging mode using what we have named "Extra-

Objective Oblique Illumination". The microscope can also perform interlaced ultra-darkfield and fluorescence image acquisition.

Fluorescence

The instrument is equipped with a frequency and intensity-stabilized helium-neon laser (Research Electro-Optics, Inc. 32734) providing up to 2.5 mW of power at 633 nm, and two diode-pumped solid state lasers (CrystaLaser CL555-075-O, DL405-120-O) providing up to 20 mW at 405 and 555 nm. The laser outputs are modulated by two AOMs (the HeNe and 555 nm lasers through an Isomet model 1201E with Neos N64010 driver and the 405 nm laser through an IntraAction Corp. model ASM-1202B67 modulator with ME-1204 driver) to control their output power, and to interlace their output with the optical traps if desired. The modulation signals are timed and sourced by the FPGA before being sent through a pair of custom-built voltage followers (figure 2.2) to provide enough current for the 50-Ω impedance of the AOM driver inputs. Identical voltage followers also buffer our AOD and LED modulation signals. A flip-mount mirror allows the operator to select which of the AOM outputs is directed into the objective. Two fixed iris diaphragms are in place in the fluorescence excitation pathway to aid in alignment when switching between fluorescence laser sources.

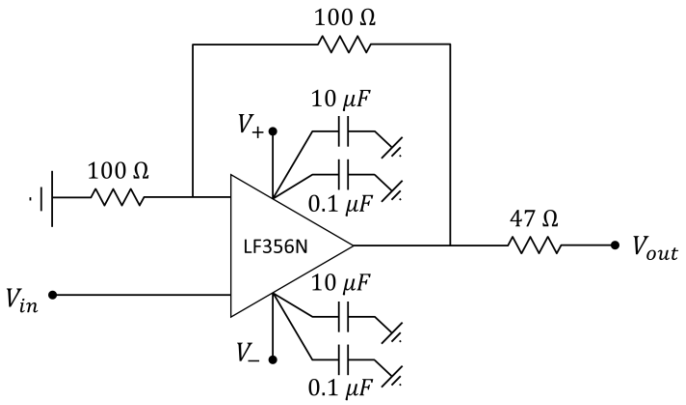

Figure 2.2 – Voltage Follower for High Speed Modulation
The circuit schematic of our voltage follower, which is based around a low-noise JFET operational amplifier (Texas Instruments LF356N). A high input impedance is compatible with the low current output of our FPGA board (10 mA). Typically op-amps for voltage followers are operated with unity gain, however by implementing a gain of 2 followed by a ½ voltage divider, the circuit is more stable with less noise, but still very fast (op-amps perform better with an applied gain, but gain reduces speed proportionally). The output square wave, for amplitudes between 0 and 1V and speeds up to 1 MHz, has a rise time of 250 ns, 0.4% noise peak-to-peak, and no ringing. We power the op-amp with a ±5V linear AC/DC converter (Bel Power HAA5-1.5-OVP-AG) with 0.1% ripple noise.

The selected excitation source is expanded, spatially filtered through a pinhole to produce a roughly Gaussian profile, and then a final lens on another flip-mount mirror allows for either collimated or focused laser illumination to be incident on the objective back focal plane for focused, or epi-fluorescence excitation, respectively.

Transparent Imaging Illumination

Imaging of transparent samples is enabled via a standard 20 W halogen lamp located on a axial translation stage enabling the positioning of the lamp one to eight inches above the sample. A collection lens roughly collimates the lamp illumination to a half-centimeter diameter width so that a greater portion of the lamp's output is collected by the objective after passing through the sample.

Reflection Imaging Illumination

Illumination for reflection imaging is provided by an LED (Luxeon MR-B0040-20S) emitting up to 70 lumens at a wavelength of 470 nm. We collect and focus the LED light using a condenser, then map the condenser's focal point to the back focal plane of the objective for plane-wave imaging in the sample plane. A 50/50 beam splitter housed in a Nikon filter cube allows a portion of the LED light to be sent to the sample and a portion of the reflected light to reach the camera. A significant amount of light passes through the beam splitter en route to the objective, and this extra light isn't entirely absorbed by the beam block within the filter cube wheel housing. Scattered light that is not completely absorbed in the beam block will reflect on the back side of the 50/50 beam-splitter and be directed onto the camera, saturating the pixels and obscuring the image signal originating from the sample.

To overcome this, we implemented an optical isolator using a Glan-Thompson polarizer and quarter wave plate. We direct S-polarized light onto the beam splitter, which reflects S-polarized light at 67%. The wave plate converts the S-polarized light into circularly polarized light, the axis of which changes direction upon reflection and is converted to P-polarized light by the wave plate on the way back. This polarization is preferentially transmitted by the beam splitter at 66% and helps to minimize the occurrence of and isolate the camera from unwanted scattered light.

Ultra-Darkfield Imaging by Extra-Objective Oblique Illumination

There are certain applications of optical trapping combined with fluorescence where it is desirable to visualize both fluorescence emission and the surrounding environment, for example to visually confirm the location of a tagged protein relative to an experimental construct [Inman et al. 2014], to translocate a labeled template within a narrow microfluidic channel, or to manipulate a dye into the vicinity of an external probe. Furthermore, image-based force and position measurements in an optical trap are incompatible with simultaneous fluorescence measurements in the traditional configuration.

Inman et al. recently developed a creative two-channel imaging solution to this problem by modulating an LED via a custom-built LED controller for bright-field illumination so as to interlace bright field and fluorescence images in successive camera frame exposures. The LED wavelength is chosen to match the emission wavelength of the dye in question in order to pass through the fluorescence filter cube to the CCD camera un-attenuated. The images can be combined in real-time or in post-processing to yield a simultaneous view of brightfield features and fluorescence emission.

In this implementation, the LED light must be introduced from the side of the objective opposite the fluorescence excitation, and the method is therefore not compatible with opaque samples. Because fluorescence filter cubes are specifically

designed to isolate emission wavelengths from excitation wavelengths, there is no way to introduce light to the objective from the excitation side that will also pass through the fluorescence filter to the camera. Instead, we built a ring-LED device that mounts around the rim of the objective to illuminate a sample from the side, directly at the sample/objective interface. This technique allows darkfield illumination with any wavelength for which an SMD-mount LED may be purchased, is compatible with opaque samples, and does not require modifying the optical path, additional filters which would be detrimental to fluorescence collection efficiency, or blocking any part of the objective aperture. Shown in figure 2.3a, this device represents, to our knowledge, the first concurrent implementation of darkfield imaging and optical trapping through the same objective.

Side-emitting at 625-nm, surface-mount LEDs with a footprint of 2.1 by 0.6 mm (Kingbright APA2106SECK/J3-PRV) were purchased from Mouser and soldered to PCB board fragments fixed to a copper ring which rests along the nose of the objective, and angles the LEDs slightly upward into the sample/objective interface. The LED ring sits just below the surface of a sample and does not interfere with the objective-sample spacing. The LEDs were wired into three parallel series and driven by a Thorlabs LED driver (LEDD1B) via a TTL (transistor-transistor logic) input sourced from the FPGA board described in section 2.3. The FPGA can drive the LEDs in 2-channel mode, in which the LED is synchronized to alternating camera

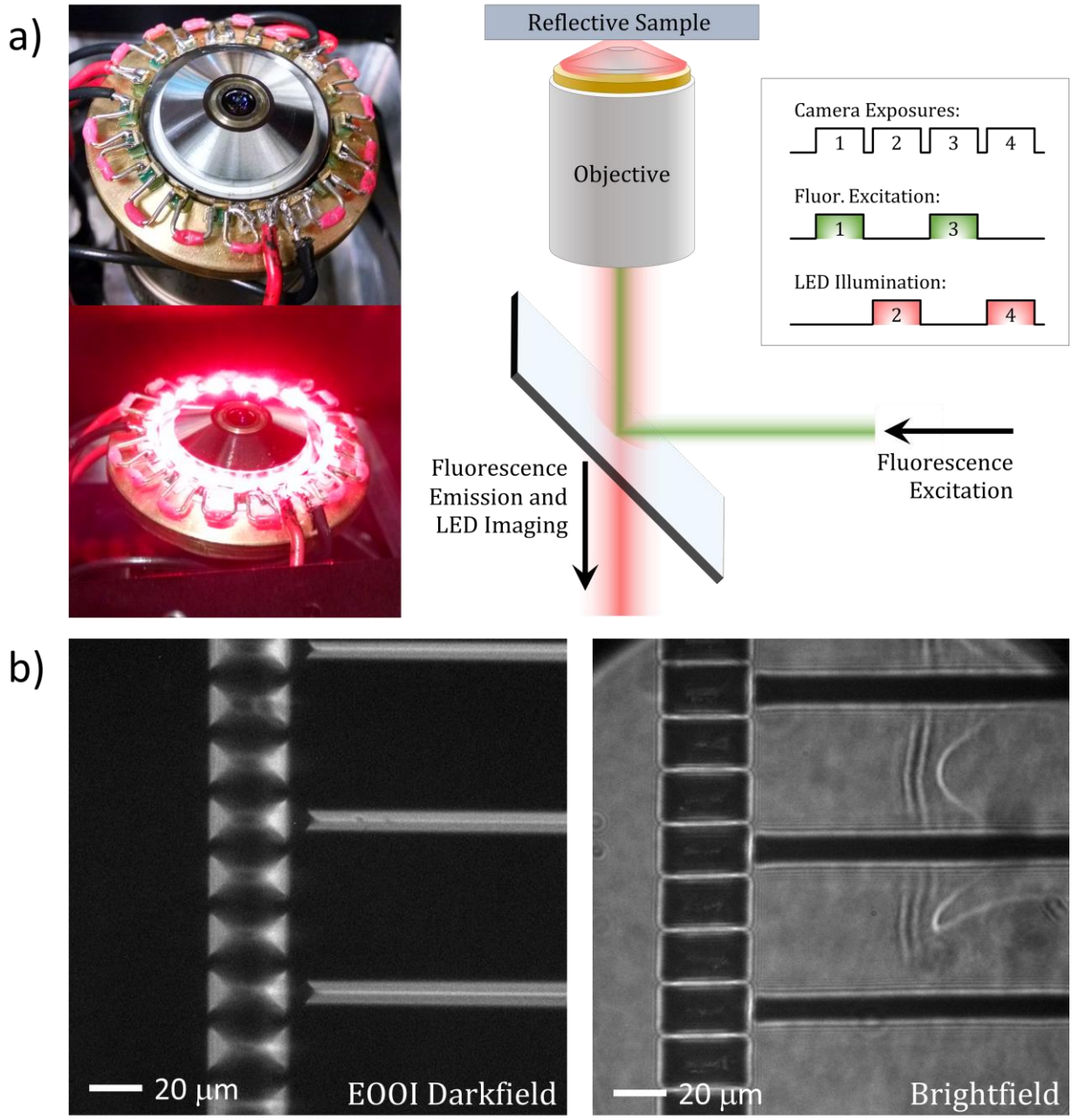

Figure 2.3 – Extra-Objective Oblique Illumination for Ultra-Darkfield Imaging
a) Side-emitting surface-mount LEDs are assembled on a ring that sits at the objective nosepiece. The LEDs are angled slightly upwards to illuminate the sample, and do not interfere with the objective-sample spacing. The LED emission is chosen to emit at the fluorescence wavelength so it passes through the dichroic fluorescence filter. LED illumination and fluorescence excitation can be interlaced on alternating camera exposures which are then combined in software to visualize structures and fluorescence simultaneously. **b)** An image of gold wedges fabricated on silicon is shown using the EOOI illumination technique (left) and using regular brightfield illumination (right). The technique provides excellent contrast for axially-oriented, reflective structures that are typically dark with standard brightfield illumination.

frames to interlace with fluorescence images (figure 2.3a), or in CW mode for regular darkfield imaging. Figure 2.3b shows an example EOOI image taken of gold wedges fabricated on silicon, along with a corresponding brightfield image of the same structures. The oblique illumination provides excellent contrast along the axial dimension of reflective structures.

2.3. Timesharing

Timesharing describes the rapid modulation of trap position in the sample plane in order to create multiple trapping centers from a single laser beam source. Compared to polarization-based dual traps, timesharing setups are easier to align, provide innately symmetric traps, eliminate cross-talk, and more readily enable full and independent control of power and position for two or more traps. However, they require more advanced equipment to achieve high-bandwidth modulation and detection, and the effects of trap modulation must be taken into account for high-resolution applications. With only one active trap in the sample plane at any given time, the instantaneous forces on a stretched tether are always imbalanced, resulting in an oscillatory motion of a dumbbell tether system along its axis at the modulation frequency. We will begin this section by detailing our timesharing implementation

from both a hardware and software standpoint, then discuss the implications of timesharing on trap stiffness and measurement precision.

Trap Modulation

The magnitude of any adverse effects resulting from timesharing scales inversely with the trap modulation frequency, and so for precision trapping applications, it is always advisable to modulate the traps as rapidly as is feasible [Visscher et al. 1996]. Acousto-optic devices outshine mechanical devices like piezoelectric or scanning galvanometer mirrors in terms of speed and accuracy, while offering a superior deflection range to electro-optic modulators, and are therefore the implementation of choice for high-speed, large-angle modulation applications. The speed of an acousto-optic device is limited fundamentally by the speed of sound within the crystal; when a new frequency and amplitude is sent to the AOD transducer, the resulting acoustic wave takes a finite amount of time to propagate through the beam width. The resulting rise time is expressed as

$$\tau_r = \frac{d}{1.5v}$$

where d is the $1/e^2$ beam diameter and v is the acoustic wave velocity in the crystal. Our AOD (Gooch and Housego (previously Neos) 45035-3-6.5DEG-1.06) uses a TeO_2 crystal in shear wave mode, for which the acoustic velocity is 0.66 mm/μs,

resulting in a rise time for our system of around 2 μs. Our chosen modulation rate of 50 kHz thus gives us a predicted duty cycle of 40%. Additionally, since our crystal is larger than the beam propagating through it, the acoustic velocity contributes to a time lag between the driving signal and the AOD response.

Our AOD accepts an RF driving signal of up to 2 W of power between 25 and 45 MHz to deflect the beam through an angle of 32 mrad, which corresponds to ~18.2 μm in the sample plane. This driving signal is generated by a 30-bit digital RF frequency synthesizer (Gooch and Housego (previously Neos) N64010-200-2ASDFS-2). The amplitude of the RF output is controlled by an analog input between 0 and 1 V, and the frequency of the RF output is specified through a 37-pin connector, where 30 of the pins are used to represent the target frequency as a binary TTL signal. In order to modulate our traps at 50 kHz, we use an FPGA (NI PCIe-7852R) to generate our input signal to the RF synthesizer, and to coordinate other control and acquisition tasks to the trap modulation. An FPGA allows these tasks to be hardware-time to a precision of 25 nanoseconds as determined by the 40 MHz onboard FPGA clock.

We programmed our FPGA using LabVIEW 2015. To control the frequency, the FPGA writes the value of 30 digital output lines which feed into the 37-pin frequency input on the RF synthesizer, and one analog output which feeds the amplitude input on the RF synthesizer. The FPGA outputs are written by a timed loop structure whose period of execution is dynamically designated in each loop

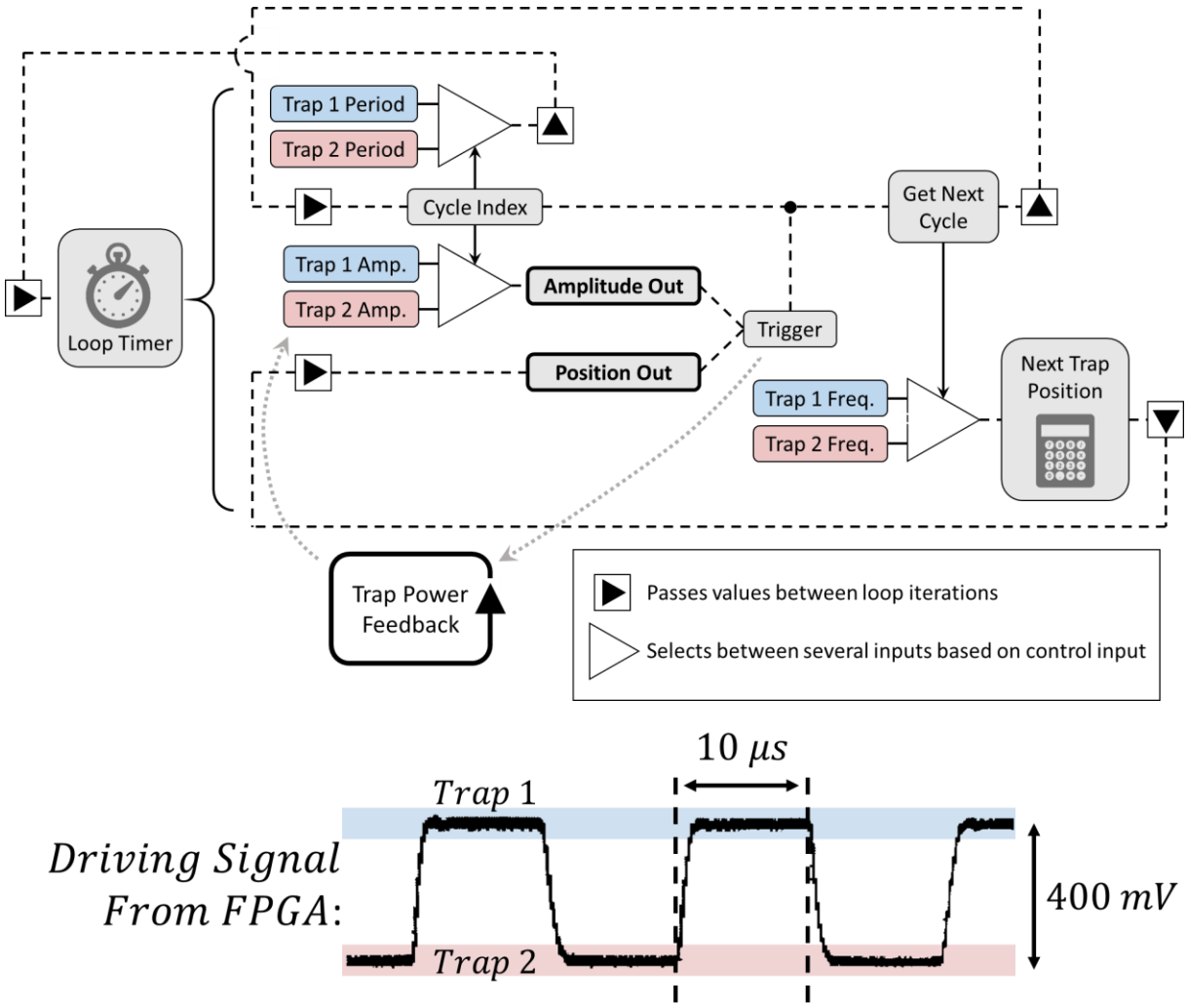

Figure 2.4 – FPGA Trap Modulation at 50 kHz
a) Schematic showing the control and data flow in the FPGA trap modulation software. **b)** The analog voltage signal output by the FPGA to control trap power is shown, after passing through the voltage follower shown in figure 2.2. The signal was sampled on an oscilloscope.

iteration. A schematic of the modulation loop is shown in figure 2.4a. When the timed loop initiates, a new trap frequency and amplitude are first written to the RF synthesizer, and then an internal trigger is generated which alerts other loops responsible for measuring trap power that a new trap value has been written, so that trap power measurement may be synchronized to each trap (see section 2.4 for more details).

Next, calculations are performed to determine the output frequency to write for the next loop cycle, as well as how long the loop should wait before the next iteration. This final stage of the modulation loop also controls a cycle index variable, which determines the modulation sequence. If either trap 1 or trap 2 is on in single-trap mode, the cycle index will be 1 or 2, respectively, for each loop iteration. When both traps are on, the cycle index alternates between 1 and 2. In addition to determining which frequency and amplitude values are output, the cycle index also selects the loop timing, and in this way the software allows fully independent control of each trap's position, power, and relative duty cycle. For interlacing with a third signal such as fluorescence excitation, the cycle index runs through values of 1, 2, and 3, where the FPGA outputs 0 during cycle 3 for a period of time determined by the user.

In figure 2.4b we show the analog signal generated by our FPGA to control trap power, after is has passed through a voltage follower that was previously described in figure 2.2. The traps are modulated here at 50 kHz, with trap 1 set to 50 mW power, and trap 2 set to 0 mW power. The data was acquired with an oscilloscope (Tektronix TDS 220) sampling at 1 Gsamples/s.

Modulated Traps, Modified Stiffness

An untethered bead in the harmonic potential of an optical trap will undergo Brownian motion, subject to the viscous drag force which is proportional to the

particle's velocity, and the force exerted by the optical trap which is proportional to the bead's displacement from the trap center. Thus its equation of motion in one dimension is given by the Langevin equation

$$\beta\dot{x} + kx = F(t)$$

where $\beta = 6\pi\eta r$ is the viscous drag coefficient, η is the dynamic viscosity of water, r is the bead radius, and k is the trap stiffness. The inertial term $m\ddot{x}$ is dropped; its characteristic time, m/β, is on the order of nanoseconds. The stochastic driving force $F(t)$ is provided by the thermal (Brownian) force on the bead, has zero mean, and satisfies

$$\left|\tilde{F}(f)\right|^2 = 4\beta k_B T.$$

This lead to the familiar Lorentzian power spectrum (Figure 2.5a)

$$|\tilde{x}(f)|^2 = \frac{k_B T}{\pi^2 \beta\left({f_c}^2 + f^2\right)}$$

where the corner frequency f_c is related to the optical trap stiffness k:

$$f_c = \frac{k}{2\pi\beta}$$

For a 500-nm bead and typical experimental trap stiffness of 0.1 pN/nm, this yields a corner frequency of 3.7 kHz. Fluctuations faster than the corner frequency are suppressed by the surrounding fluid.

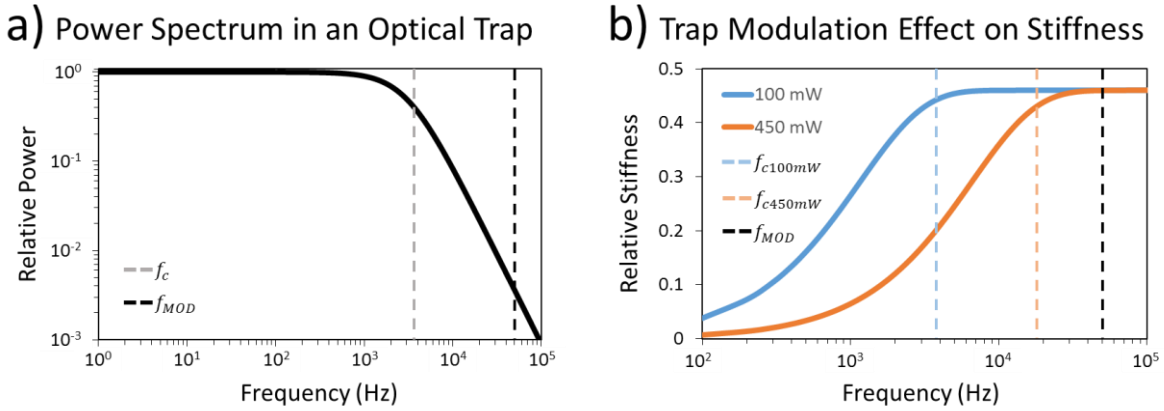

Figure 2.5 – Effects of Trap Modulation on a Free Bead
a) A model Lorentzian power spectrum is shown with a typical corner frequency for our experimental conditions of 3.7 kHz (grey dash), and our trap modulation frequency of 50 kHz (black dash) indicated. The amplitude of fluctuations occurring at frequencies faster than the corner frequency are heavily damped. **b)** Modulation decreases trapping stiffness below the time-averaged value at slow modulation rates. Here we show a prediction, based on an empirical model by Brau et al., of trap stiffness versus modulation frequency at a common trapping power (100 mW, blue), and our maximum trapping power (450 mW, orange). The corner frequencies for both trapping powers are indicated by dashed lines for reference. Trap stiffness in both cases increases with modulation frequency, rising to the maximum permitted by our duty cycle of 0.46 soon after surpassing the corner frequency. At our trap modulation rate of 50 kHz (black dash), our trap stiffness is not significantly affected by the modulation.

In a time-shared optical trap, if the time a particular trap is "off" while the laser is visiting another site is short enough such that $t_{off} \ll 1/f_c$, the bead response to the time-varying trap stiffness it experiences locally will be strongly damped. For the case of two traps, we require that the modulation frequency satisfies $f_{MOD} \gg f_c$, and in this case the effective trap stiffness is the time-averaged value for a trap of stiffness k when the laser is present, and 0 when the laser is away, or k times the modulation duty cycle. As modulation rates approach or drop below the corner frequency, the effective trap stiffness is reduced as the particle is permitted to diffuse through a larger volume of space during t_{off} [Brau et al. 2006]. Brau et al. measured trap

stiffness as a function of modulation frequency in a single trap at various laser powers. Because they used a second detection laser for their photodiode-based position measurement, they were able to monitor bead position continuously, even while the trapping laser was off. The resulting trap stiffness, as determined through the equipartition theorem, was found to vary relative to the maximum stiffness in a continuous trap of the same power according to an exponential function of the form $y = A\left(1 - e^{-f/f_m}\right)$, where A is the modulation duty cycle, f is the modulation frequency, and f_m is a characteristic frequency of the curve that scales linearly with trap stiffness. This relationship is shown in figure 2.5b for a trap power of 100 mW, a common experimental condition, and 450 mW, our maximum trapping power. Our modulation at 50 kHz is fast enough to avoid adversely affecting trap stiffness for all possible laser powers on our instrument.

Dumbbell Oscillations in a Modulated Dual Trap

So far we have examined the effects of trap modulation on the dynamics of an untethered bead in an optical trap. However, in general we are interested in applying forces to and measuring forces from a biological system, and this additional force will affect bead motion in the trap. The most common dual trapping configuration uses a dumbbell tether, in which a bead held in each trap suspends a DNA template between them. A CW dual trap requires that, at equilibrium, the force of the traps on the beads

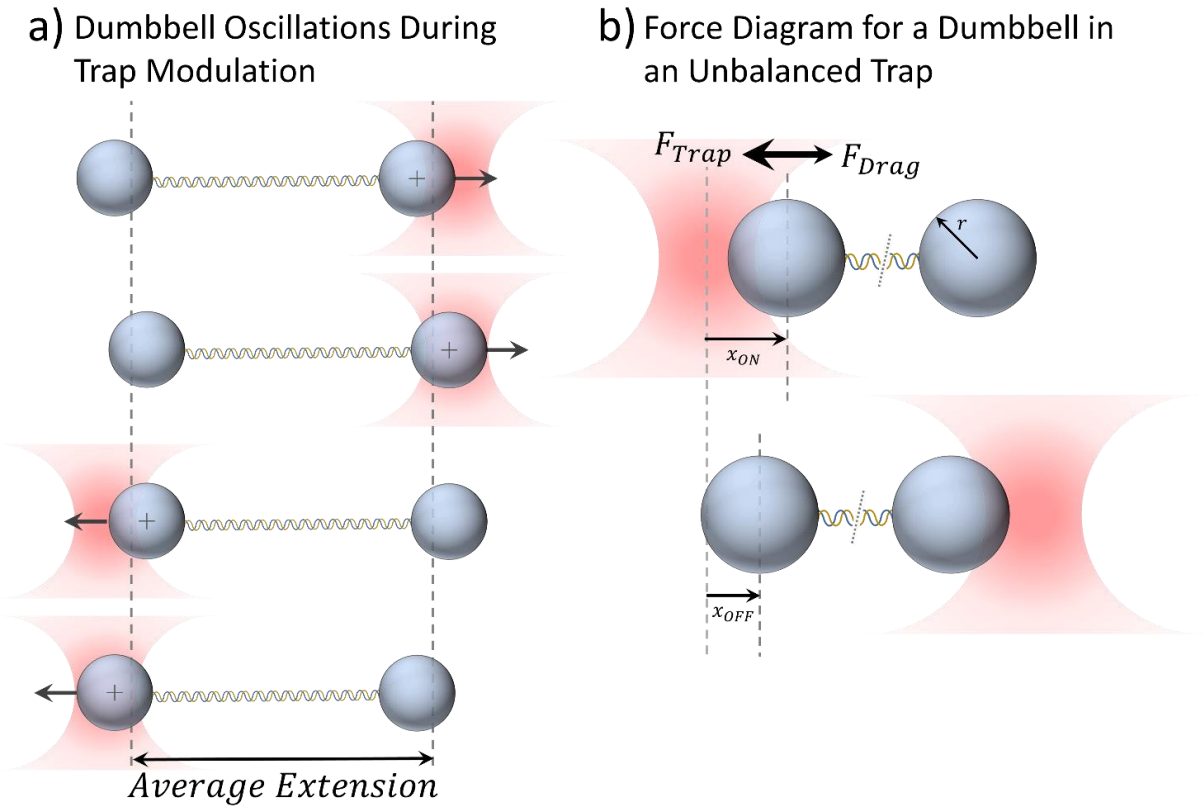

Figure 2.6 – A Dumbbell Tether Oscillates in a Modulated Trap
a) Because only one trap is on in the sample plane at any given time, the force on a dumbbell tether is always imbalanced, leading to oscillation of the dumbbell position along the axis of force at the modulation frequency. Each bead will oscillate about an average position in the trap that is symmetric when trap stiffness is symmetric. **b)** During a trap's on period, the dumbbell will experience a trapping force and a viscous drag force. We denote the position of one of the beads in the trap when the trap is first turned on, and when it is turned off a time Δ later, as x_{ON} and x_{OFF}, respectively. A symmetric but inverted picture exists for the bead in the other trap.

is balanced by the force of the DNA on the beads. In a modulated trap, in contrast, the force exerted on a bead at any given time is unbalanced, and will lead to an oscillation of the dumbbell system at the modulation frequency (figure 2.6a).

The flexibility and extensibility of the DNA linkage plays a significant role in the resulting bead dynamics. The fluctuations of a dumbbell system held in a CW dual trap have been thoroughly treated by Moffitt et al [Moffitt et al. 2006]. They derive

the thermally-limited signal-to-noise ratio (SNR) floor for a tethered bead as the ratio of the average bead displacement caused by a change in tether length ΔL, to the root mean square thermal fluctuations of the system. For one of the beads in a dual trap dumbbell configuration, assuming symmetric traps of stiffness k and identical beads of radius r, the SNR varies with trap stiffness and DNA stiffness, approaching an asymptotic maximum independent of DNA stiffness when $k_{DNA} \gg k$:

$$SNR_1 = \frac{k\Delta L}{\sqrt{2\beta}\sqrt{4k_B TB}}\sqrt{\frac{1-(\beta/\Gamma)^2}{1-\beta/\Gamma}}$$

Here, $B = f_{ave}/2$ is the measurement bandwidth of high-frequency data averaged to a frequency f_{ave}, $k_B T$ is the thermal energy, and Γ describes the hydrodynamic coupling between the two beads. Γ is constant when the separation between the two beads, R, is large with respect to the size of the fluctuations, and when R is also large with respect to the bead radius r, it is given by $\Gamma = 4\pi\eta R$ [Meiners and Quake 1999]. This is the SNR expected for two beads connected by a thin, rigid rod, in which the total drag coefficient is given by $\beta_1 + \beta_2 = 2\beta$. It is larger than the corresponding single trap SNR, due to the Brownian noise in each trap adding in quadrature.

In general, k_{DNA} varies significantly with tether length L, however for small changes in extension we can approximate DNA as a linear spring and expand its force-extension behavior about the equilibrium extension ξ_{eq} such that $k_{DNA} \approx$

$dF_{DNA}/d\xi|_{\xi_{eq}}$. Once DNA has been extended past its so-called entropic region [Wang et al. 1997], DNA stiffness rises rapidly as a tether is extended to and beyond its contour length, and is in general around an order of magnitude larger than the trap stiffness for forces of a few pN and higher.

As DNA stiffness rises as a tether is extended, so does the coupling between the two beads in a dumbbell tether. This results in an SNR increase when monitoring the differential signal in a dual trap, as compared to the SNR from just one of the two bead presented above. All noise that couples into symmetric bead motion is eliminated from the differential measurement, and only antisymmetric changes in bead position result in a signal. The maximum SNR in this case is given by

$$SNR_2 = \frac{k_{DNA}\Delta L}{\sqrt{\beta/2}\sqrt{4k_BTB}}\sqrt{1-\beta/\Gamma}$$

The ratio of SNR_2 to SNR_1 reflects to a certain extent the degree to which bead oscillations are coupled leading to a reduced noise floor in the differential signal:

$$\frac{SNR_2}{SNR_1} = \frac{2k_{DNA}}{k}\sqrt{\frac{1-\beta/\Gamma}{1+\beta/\Gamma}}$$

Since $R > r$, we will always have $\Gamma > \beta$, and so the radical expression will assume a value between 0 and 1.

If we model our dumbbell system as a pair of beads connected by a rigid rod (figure 2.6b), which we have shown is a reasonable approximation over the short timescales under consideration and at moderate to high DNA forces given the large ratio of k_{DNA} to k, the resulting oscillations of the dumbbell in a modulated dual trap are simple to derive [Capitanio et al. 2007]. Neglecting the thermal force since its time average is zero, the equation of motion is given, according to figure 2.6b, by

$$\beta' \dot{x} + kx = 0$$

where β' represents the effective drag of the dumbbell system. This is given by $6\pi\eta r'$ where $r' = r_1 + r_2 = 2r$. This equation accepts solutions of the form

$$x(t) = x_0 e^{-(k/\beta')t}$$

If we designate the position of a bead in one of the traps when it is first turned on as x_{ON}, then its position x_{OFF} a time Δ later when the trap is turned off will be

$$x_{OFF} = x_{ON} e^{-(k/\beta')\Delta}$$

A symmetric but inverted picture exists for the bead in the opposite trap. Additionally, we know that the average of x_{ON} and x_{OFF} is equal to the bead's average displacement in the trap x_{AVE}, therefore $x_{ON} + x_{OFF} = 2x_{AVE}$. Combining these relationships gives

$$x_{ON} = \frac{2x_{AVE}}{1 + e^{-(k/\beta')\Delta}}$$

$$x_{OFF} = \frac{2x_{AVE}}{1 + e^{(k/\beta')\Delta}}$$

and thus the amplitude of the oscillations will be given by

$$|x_{ON} - x_{OFF}| = (2x_{AVE})\frac{1 - e^{(-k/\beta')\Delta}}{1 + e^{(-k/\beta')\Delta}}$$

We can now examine how the amplitude of oscillation varies with experimental parameter. Figure 2.7a shows oscillation amplitude versus modulation frequency on a log-log scale for various trap stiffnesses, for oscillations about an average bead position fixed at 50 nm from the trap center. At slow modulation speeds, the bead relaxes fully to the center of its trap during the "on" period, giving an amplitude of twice the average bead displacement. The oscillation amplitude drops sharply after the trap's stiffness-dependent corner frequency is reached, but is still a bit over 10 nm at the highest possible power setting of 450 mW in our instrument. At a 50-nm average displacement with 50 kHz modulation, the trap stiffness values of 0.02, 0.05, 0.1, 0.2, 0.3, and 0.45 pN/nm, which correspond to forces of 1, 2.5, 5, 10, 15, and 22.5 pN, give oscillation amplitudes of 0.6, 1.4, 2.8, 5.5, 8.0, and 11.5 nm, respectively.

The oscillation amplitude is linear as a function of force (figure 2.7b), and the resulting dependence is relatively invariant with respect to trap power and bead displacement at 50 kHz modulation. At lower modulation rates, however, the oscillation as a function of force depends significantly on the trap stiffness. The slope

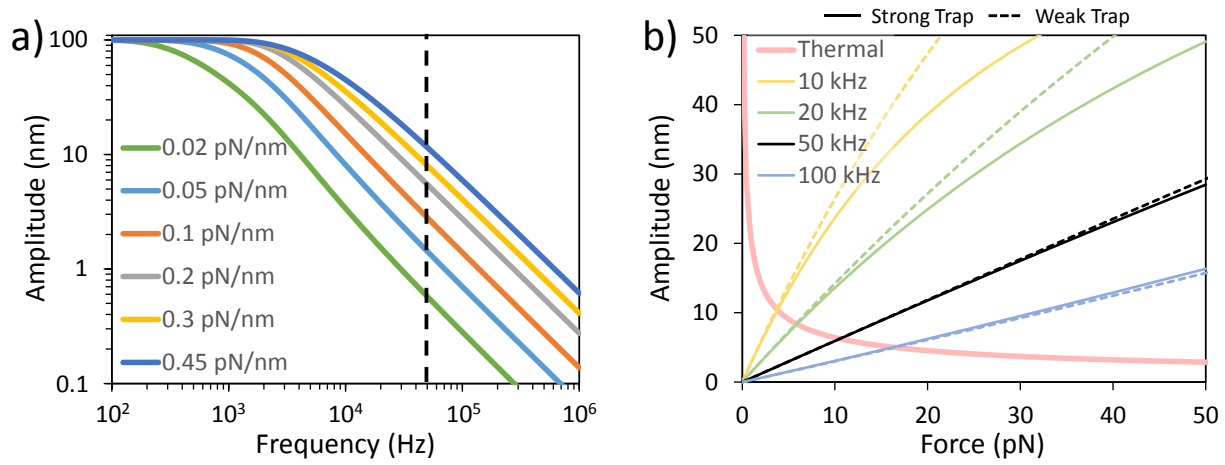

Figure 2.7 – Dumbbell Oscillation Amplitude in Time-shared Traps

a) For the dumbbell motion described by $x(t) = x_0 e^{-(k/\beta')t}$ where k is the trap stiffness and β' is the viscous drag coefficient of the dumbbell system, the amplitude of the oscillations induced by trap modulation is plotted on a log-log scale versus modulation frequency for various trapping stiffnesses, assuming the average position of the bead in each trap is 50 nm. Our trap modulation rate of 50 kHz is indicated by the dashed line. **b)** Dumbbell oscillation is plotted as a function of force applied to the DNA tether, for varying modulation rates for both a strong trap (solid line, 50 nm fixed average bead displacement) and weak trap (dashed line, 100 nm fixed average bead displacement). For high modulation rates, the relationship does not depend on trap stiffness. For high forces, dumbbell oscillation is significant at 50 kHz.

of the oscillation amplitude-force relationship for our trap at 50 kHz is 0.55 nanometers of oscillation per piconewton of applied force. It is informative to compare the scale of oscillations to the thermal fluctuations of a trapped free bead which are given by $\sqrt{k_B T/k}$. For a bead fixed at 100 nm displacement in a trap, we can vary trap stiffness to obtain an analogous amplitude-force curve. The crossover point at which the oscillations overtake the thermal noise is at 10 pN of force.

Although many time-shared instruments exist, the phenomenon of dumbbell oscillations has rarely been investigated experimentally. Molloy measured an oscillation amplitude of 2.5 nm for an actin filament suspended between two beads

for a dual trap modulation rate of 10 kHz and an application of 2 pN force. Our model predicts an oscillation amplitude of just over 5 nm at those conditions, however their experiment was performed near the fluid chamber surface in which fluid drag is significantly higher [Molloy 1998]. Although they did not mention values for the oscillation amplitude, Comstock et al. present measured, high bandwidth trap position data for their time-shared dual optical trap in the supplemental information of their 2011 publication in which the oscillations are visible and on the order of 10 nm [Comstock et al. 2011], however the force is not specified.

Sample oscillations induced by a time shared dual optical trap present a few potential complications. First, when measuring the positions of the optically-trapped beads with a high-bandwidth detector like a photodiode, the oscillations will add to the position uncertainty. However, if an FPGA is used, Comstock et al. showed that relative position can still be determined with sub-nanometer precision in their case, if the sampling of the high bandwidth photodetector is synchronized to the middle of the trap's on period [Comstock et al. 2011], essentially timing their measurement to sample bead position when the bead is at its average position. The contribution from sample oscillation to the error in bead position measurement is then determined by the sampling time resolution of the FPGA (200 kHz in their case) relative to the oscillation amplitude. Notably, for a low bandwidth detector which integrates over its sampling period, as in image-based detection, the bead oscillations will be pre-filtered

to their average values, with the oscillations only affecting the apparent bead size along the force axis. For this method of position detection, we only required that the camera exposure time is significantly larger than the modulation period. The oscillations will also affect the tracking of fluorescent labels which, like beads, will see their width distributions widen along the axis of force. Although this should not affect the accuracy of position tracking if again we integrate an exposure over many modulation cycles, in shot-noise-limited applications the increased fluorescent spread will reduce precision. Finally, the introduction of rapid sample motion of potentially several tens of nanometers over a period of 10 μs will introduce oscillating viscous drag forces to the specimen, however for proteins on the order of 5 nm in radius (an upper end estimate), these forces are much smaller than 1 pN.

From the relationship derived earlier for dumbbell position in a trap as a function of time, dumbbell velocity during a trap's "on" cycle will be given by

$$v(t) = -\frac{k}{\beta'} x_{ON}\, e^{-\frac{k}{\beta'}t}$$

We may then substitute in the expression derived earlier for x_{ON}, and use the relationship $F_{DNA} = kx_{ave}$ to write the velocity expression in terms of the force applied to a dumbbell tether:

$$v(t) = \frac{-2F}{\beta'} \frac{e^{-\frac{F_{DNA}}{\beta' x_{ave}} t}}{1 + e^{-\frac{F_{DNA}}{\beta' x_{ave}} \Delta}}$$

This relationship can be transformed to express the viscous drag force acting on a bound specimen protein moving at the dumbbell velocity by multiplying by the protein's drag coefficient $\beta_p = 6\pi\eta r_p$, which assumes a value of just under 10^{-7} pN·s/nm for a generous protein size estimate of 5 nm for r_p. Both the velocity and the proportional drag force versus time for such a protein is shown in figure 2.8a for various dumbbell tether forces (and thus varying oscillation amplitudes). Note that at 50 kHz modulation, the motion is cut short after 10 μs, when the current trap is turned off and the second trap is turned on. The inset in figure 2.8a shows the relevant 10 μs portion of the data with a linear scaling. Since the oscillation amplitude will be given by the area under the velocity-time curve, it is clear why, with 50 kHz modulation, the oscillation amplitude as a function of force does not depend on trap stiffness, whereas this is not the case for slow modulation rates. The maximum drag force experienced by a protein bound to an oscillating dumbbell occurs at $t = 0$, and this value is shown as a function of force applied to the DNA dumbbell tether for a strong and a weak trap in figure 2.8b. The dependence on trap strength is minimal, and the maximum drag force on even a very large protein at very high tether forces is a fraction of a piconewton.

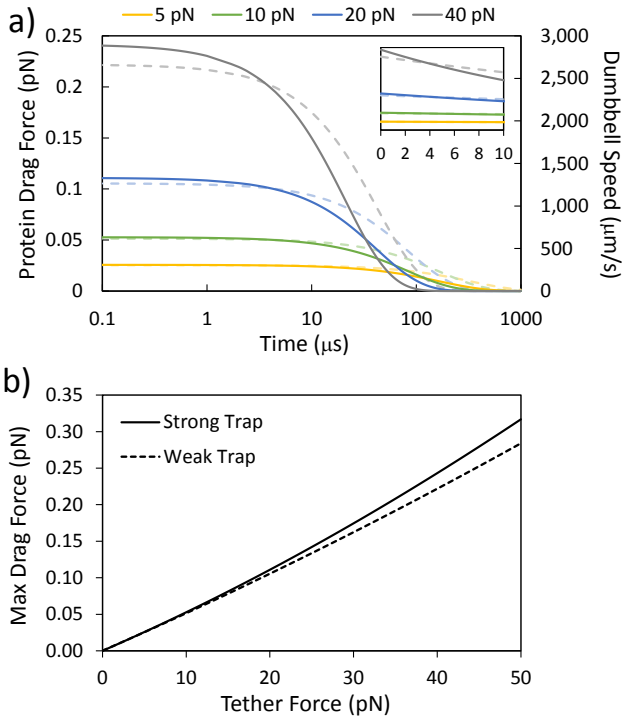

Figure 2.8 – Dumbbell Velocity and Viscous Drag on a Bound Protein
a) Dumbbell velocity as a function of time is plotted on the secondary y axis for various values of force applied to the dumbbell tether, for both a strong (average bead position fixed at 50 nm) and a weak (average bead position fixed at 100 nm) trap. The inset shows the first 10 μs of dumbbell motion on a linear scale, which is the "on" period for our traps modulated at 50 kHz. It is clear why, at these rates, the dumbbell oscillation amplitude as a function of force as shown in figure 2.7b does not depend on trap stiffness, which is represented here by the area under the velocity-time curve. The corresponding drag force values acting on a protein of radius 5 nm bound to the dumbbell tether is shown on the primary y axis. **b)** The maximum drag force on the aforementioned bound protein as a function of force applied to the dumbbell tether. The drag force remains well under 1 pN, even for a strong trap and large dumbbell oscillation amplitude.

2.4. Trap Power Measurement and Feedback Stabilization

While the AOD provides a fast method of modulating both the position and power of the trapping laser, the diffraction efficiency across an AOD's driving frequency range is not uniform, leading to an undesired variation in trap power as a

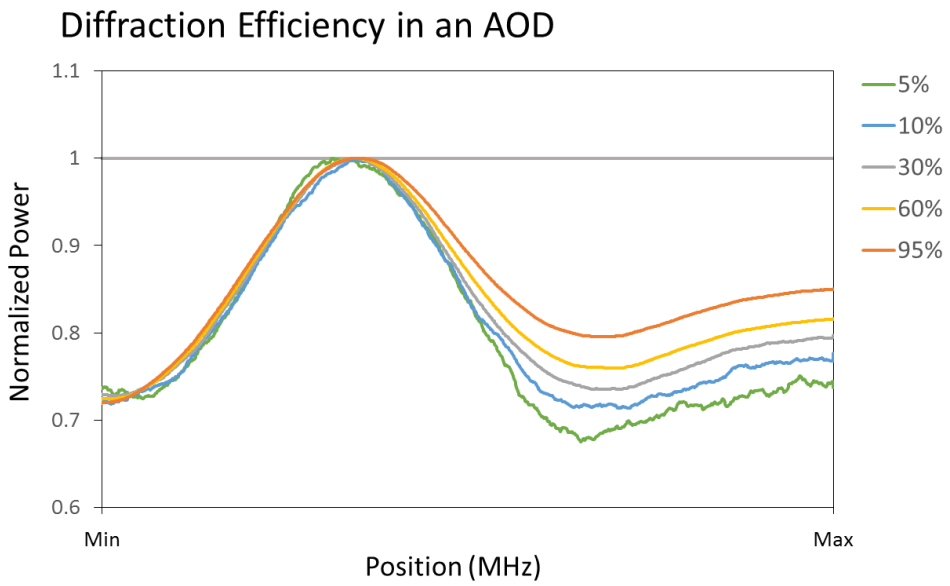

Figure 2.9 – AOD Diffraction Efficiency vs. Driving Frequency
The diffraction efficiency of an AOD is not constant as a function of driving frequency / deflection angle. The power in the first order deflected beam as a function of driving frequency was plotted at several different driving amplitudes and normalized to peak power output. The output power is found to vary within 20 – 30% of peak values, and to a variable degree with driving amplitude.

function of trap position. The power present in the first order diffracted beam as a function of driving frequency (and, correspondingly, trap position) for our AOD is shown in figure 2.9 for several different AOD driving amplitudes. Each curve is normalized to its peak power value. The diffracted power in the trapping beam exhibits a total variation between 20 to 30% of the peak power value, depending on the driving amplitude. Left uncorrected, this would result in an equivalent difference in trapping stiffness between two time-shared traps located at different positions in the sample plane.

For a diffraction efficiency curve that is constant with driving power when expressed as a percentage of the maximum efficiency (i.e., if each of the curves in

figure 2.9 were coincident), a simple look-up-table (LUT) could be used to modify the driving amplitude as a function of frequency in order to make the resulting power in the first order diffracted beam uniform. The observed variation, however, precludes the effective implementation of a single LUT and requires a two-dimensional LUT instead. Since any augmentation of trap power and position needs to be implemented at the FPGA-level, which has limited physical resources for storing large blocks of memory, we decided to forgo a 2D LUT in favor of implementing a measurement and feedback system for live power stabilization.

Measuring Trap Power

Measuring the power of each trap independently requires a specialized, high-bandwidth photodiode, as standard silicon photodetectors exhibit parasitic filtering at high speeds when measuring 1064-nm light [Berg-Sorensen et al. 2003; Berg-Sorensen et al. 2006]. Specialized Si photodiodes are made for this purpose, which are fully-depleted and can be operated with a reverse bias of up to 180V, however we chose to use an InGaAs detector (Thorlabs DET20C) for our setup since the material's responsivity curve is better-suited to measuring 1064-nm signals.

We used a pellicle beam splitter to sample a small fraction of the beam between the first expansion telescope, and used a 38.1 mm FL lens to map the AOD rotation plane onto the detector surface (2-mm in diameter) so that the beam hits the center of

the photodiode for all trap positions. We sample the photodiode current across a 517-Ω resistor, which results in a maximum voltage reading of 800 mV before saturation is observed. An appropriate combination of neutral density filters was used to attenuate the light incident on the detector surface so that the maximum trapping power (corresponding to 450 mW in the sample plane) results in a photodiode reading of 560 mV. The analog input channels on our FPGA possess a fixed range of -10 to 10 V and are digitized at 16 bits. Therefore, our detector signal will be measured across 10.8 bits of information, with each bit level corresponding to 0.3 mV on the detector, which translates to 0.24-mW resolution of our trapping power in the sample plane. Because the noise in our signal is significantly larger than one bit, much greater precision can be achieved by averaging over time.

A measurement of our 50-kHz-modulated traps made with the InGaAs photodiode is shown in figure 2.10 (lower trace), next to the driving signal output by our FPGA (upper trace). Both signals were acquired on an oscilloscope at 1 Gsamples/s. The power measurement displays a rise time of 2 μs, which is precisely the value predicted by the acoustic velocity and our beam width within the AOD, therefore we believe the response of the photodiode is fast enough to capture our trap modulation without filtering. A significant 8-μs phase delay between the driving signal and resulting traps is also present. This is due in part to the time required for the acoustic wave to travel from the transducer to the location of the beam within the

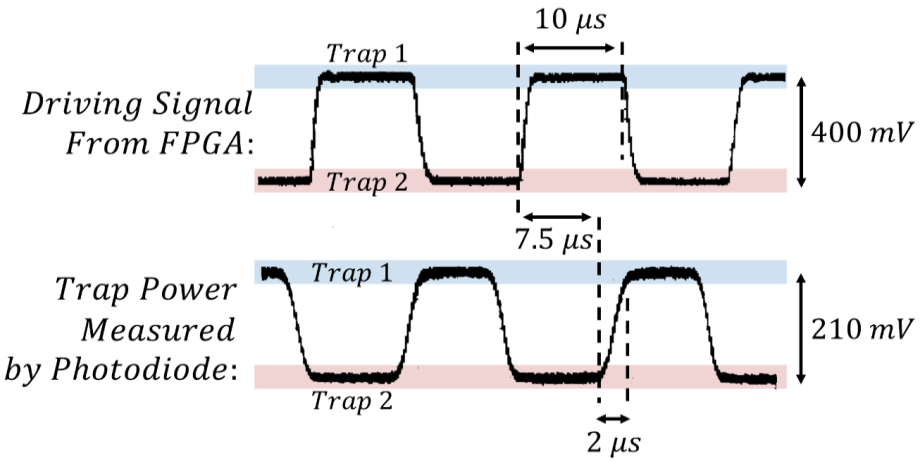

Figure 2.10 – Trap Power Modulation Measured by InGaAs Photodiode
The analog driving signal controlling trap power that is output by our FPGA was sampled on channel 1 (upper trace) of an oscilloscope, alongside the measured power of the resulting traps on channel 2 (lower trace). Trap 1 is set at 50 mW in the sample plane, and trap 2 is set at 0 mW. The rise time of 2 ms observed in the trap power is predicted by our beam width through the AOD and the AOD acoustic velocity. The phase delay is constant with respect to all modulation parameters, and is taken into account in synchronization software.

AOD crystal, and in part to the time required to write a new value to the RF synthesizer. While the latter can be fixed by using buffers or frequency switches, both of these effects are constant with respect to all modulation parameters, so we chose to simply account for this phase lag in the FPGA software when synchronizing tasks.

Power Feedback Stabilization

To perform feedback on the measured trap power, we obtain one sample for each trap per trapping cycle. Our FPGA samples its analog channels at 750 ksamples/s, or once every 1.3 μs, providing an ample window during the 8-μs trap period to take a measurement. To synchronize the analog sample acquisition with the

trap modulation without interfering with the modulation timing, the sampling is performed in two separate, independent loops whose timing is triggered by the main trap modulation loop. A schematic diagram is shown in figure 2.11a. The analog channel sampling loops wait in hibernation until they are signaled by the main modulation loop that a new trap value has been written. Each trap has a designated power sampling loop that is triggered independently according to which trap has just been written.

Once a trigger is received, the loop waits an amount of time equal to the constant phase lag plus one half the modulation time, and then a single measurement is taken in the middle of the trap's modulation period. Measurements are transferred via an internal FIFO bus to additional loops which perform feedback via PID loops. The PID loops update the new power set-point to the main loop once their calculations are completed. The raw measurements are additionally sent to a target-to-host DMA FIFO, where it is periodically read by the host application. Data points are both streamed to disk along with other acquired instrument data, and averaged and displayed for a live power reading of each trap. Figure 2.11b shows power in the sample plane as a function of AOD driving frequency / trap position for a feedback-stabilized trap. Although the measurement parameter (photodiode reading) and control parameter (AOD driving amplitude) are related non-linearly, a relatively small proportional term and longer integration period allows power stabilization within the

timescales of interest. Power maintains a standard deviation of 0.5% and peak-to-peak fluctuations within 3% of the set point across the frequency range of the AOD.

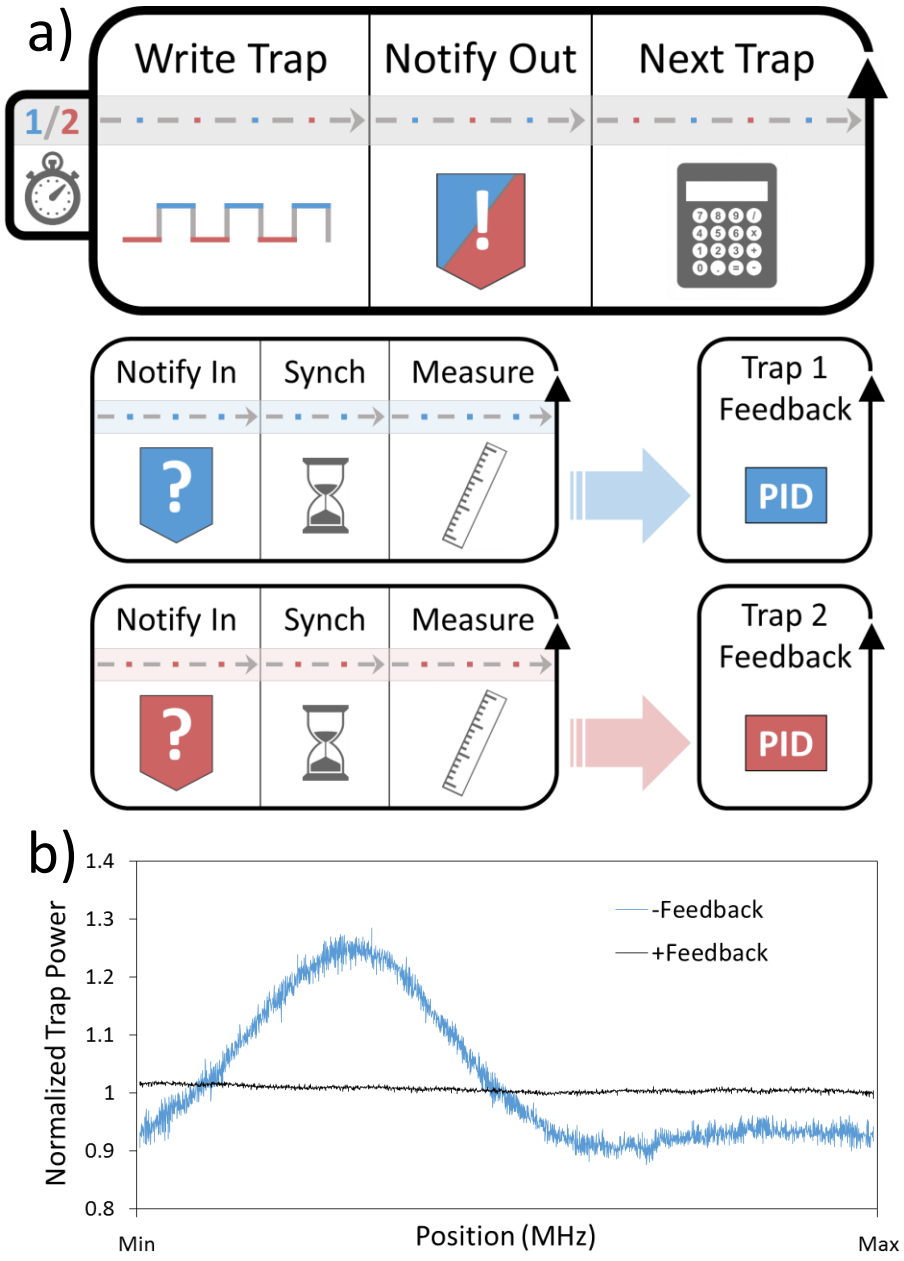

Figure 2.11 – Differential Trap Power Measurement and Feedback
a) Schematic of the power measurement and feedback in the FPGA software, enabling synchronization of the analog power measurements with the control of trap modulation at the hardware level. **b)** The results of feedback-stabilization on the measurement of power vs AOD driving frequency. Power is stabilized to a peak-to-peak range of 3% and a standard deviation of 0.5% of the target set-point.

2.5. Position Detection in Single-Objective Optical Tweezers

Overview

Traditional position detection is accomplished using back focal plane interferometry (BFPI) in a collecting objective opposite the trapping objective. The back focal plane of an objective represents a Fourier plane to the optical traps in the sample plane, in which angular displacements of the trapping beam affected by the trapped particle manifest as positional displacements. The interference pattern in the back focal plane of the collecting objective is created between the fraction of the trapping beam that is scattered by the trapped particle, and the remainder of the trapping beam which does not interact with the trapped particle. This pattern is mapped onto a position sensing device, usually a quadrant photodiode, to measure its center of mass position, and the resulting signal is calibrated to bead displacement in the trap by scanning a fixed bead with a piezo stage [Allersma et al. 1998]. BFPI has become ubiquitous in modern optical trapping instruments due to its ability to measure angstrom-level changes in bead position at tens of kHz, however because our instrument does not employ a second objective, we explored other alternatives for position detection.

Several labs have used the back-scattered light from an optical trapping setup to perform position detection in situations where the forward-scattered light was inaccessible. This eliminates the error introduced by focal drift between an objective

pair in the forward-scattering configuration, leading to improved low frequency stability [Huisstede et al. 2005]. However to ensure a stable trap in which the optical gradient forces overcome the optical scattering force, the standard trapped particle is mostly transparent and has an index just slightly above that of the surrounding medium, which minimizes back reflections from the bead. The amount of available light for making a measurement, therefore, is much smaller for the reflected-light case than the forward-scattered case, and backscatter detection becomes shot-noise-limited in particular at high frequencies [Huisstede et al. 2005]. Early implementations of back-scatter detection that used a standard beam splitter to extract the reflected light from the incoming trapping laser suffered in particular from this issue [Friese et al. 1996; Shivashankar et al. 1998].

One strategy to overcome these obstacles is to use a second detection laser of a shorter wavelength and larger reflection coefficient, which can then be isolated for measurement via dichroic filters. The alignment of the detection laser to the trapping laser is a delicate operation that is only suitable for single-trap instruments [Huisstede et al. 2005; Shivashankar et al. 1998; Soni et al. 2002]. Another solution employs a polarizing beam-splitting cube (PBSC) and quarter wave plate (QWP) to extract the reflected light from the main optical path [Carter et al. 2007; Sischka et al. 2008]. P-polarized light is transmitted by the PBSC and converted to circularly-polarized light by the QWP. The reflected light, now with the handedness of its polarization

reversed, is converted into the orthogonal linear polarization state by the QWP and is then directed at a right angle to the main beam path by the PBSC. Because this method dictates the polarization state of the optical traps, it is not compatible with polarization-based dual optical tweezers.

Regardless of the specifics of its implementation, backscatter detection is additionally susceptible to two other significant complications: first, the presence of even a weakly-reflective surface nearby to an experiment will adversely affect the measurements, and second, the complex reflections from a spherical surface display dramatically different properties as a function of bead size, detection wavelength, and objective numerical aperture. Though the first point can be mitigated (and the axial resolution potentially improved [Keyser et al. 2006; Sischka et al. 2008]) by spatial filtering through a pinhole in the case of a single trap and a slit in the case of a dual trap [van Loenhout et al. 2013], this method fails in the presence of a more strongly reflective surface.

The second point was beautifully demonstrated by Volpe et al. [Volpe et al. 2007] in a series of simulations predicting the response of a position-sensing photodiode (PSD) to bead displacement in an optical trap configured in back-scatter mode. To facilitate measurement, we require the PSD response to be linear within a certain range of bead displacements, and indeed we find a linear PSD response in the forward-scattering case with relatively minor changes in the slope and linear range as

the size of the trapped bead is varied. The back-scattering case presents dramatically different results, owing to the complex superposition of spherical harmonics in the reflected signal. As the bead size is varied, the PSD response to bead displacement exhibits several distinctive and troubling features: the magnitude of the signal is around two orders of magnitude smaller due to the weak reflections generated by polystyrene microspheres, the linear range is around one order of magnitude smaller, and the slope of the PSD response not only varies substantially, but changes sign periodically. Certain bead sizes, therefore, result in no detectable signal change as a function of bead displacement. This means that on top of all other experimental considerations, one must carefully take into account their choice of objective and bead size when constructing a back-scatter detection instrument, and the size heterogeneities within a population of microspheres could result in significant measurement errors. Due to these substantial challenges, the ability to measure one-nanometer bead displacements has yet to be demonstrated in any backscatter detection configuration.

Another more flexible option for position detection is image-based particle tracking (IBPT). This technique readily lends itself to the tracking of a large number of trapped particles, requires relatively little instrumentation to implement, benefits from the ability to share processing code between multiple instruments and developers, and is compatible with a large variety of instrument configurations and

imaging conditions. The drawbacks to IBPT have historically been in resolution and bandwidth, as the conventional CCD cameras used in the past were only able to track particles at several tens of Hz and a resolution up to 10 nm [Keen et al. 2007]. Due to these limitations, IBPT is most commonly used in magnetic tweezer setups where laser-based methods are excluded, and has historically found little use in optical tweezers instruments where BFPI presented a more attractive solution.

By the mid-2000s, however, the maturation of CMOS camera technology brought kHz framerate cameras to an affordable price point for research laboratories [Biancaniello and Crocker 2006], garnering an increased interest in their use in optical tweezers and other instruments. Keen et al. directly compared the performance of a high speed image tracking system to BFPI via a quadrant photodiode and found similar performance at 2 kHz, however their accuracy was limited to 10 nm by image noise [Keen et al. 2007]. Indeed, as camera speeds have increased and costs decreased, camera framerate is no longer a limiting factor; cameras capable of capturing a kilo-pixel ROI at tens of kHz are now available for under $10,000. These fast speeds, however, exacerbate the remaining bottlenecks: the signal-to-noise ratio of images acquired with ultra-short exposures, and the large amounts of image data which ideally need to be transferred and processed in real time.

Biancaniello et al. implemented high brightness Kohler laser illumination capable of saturating a camera sensor in 2 μs. This allowed framerates in excess of 10 kHz

with a tracking error down to 2 nm, however they were unable to perform real-time analysis due to slow data transfer rates [Biancaniello and Crocker 2006]. Other groups have implemented high intensity fiber illumination [Otto et al. 2010], superluminescent diodes (SLDs) [Lansdorp et al. 2013], and high-power collimated LEDs [van Loenhout et al. 2012] to achieve high SNR images at short exposure times with similar accuracies.

Parallel data streaming protocols such as Camera Link and CoaXPress are capable of transferring small regions of interest at tens of kilohertz, and real-time particle tracking at high speeds has emerged over the last 5 years as a result. Otto et al. achieved real-time tracking of optically trapped colloids at 6 kHz in 2011 [Otto et al. 2011], and higher speeds have been achieved by implementing onboard FPGA image processing [Towrie et al. 2009], or highly-parallelized processing via GPUs and/or multiple CPUs. These advances culminated recently in the first demonstration of sub-nanometer precision in a video-based tracking system at kHz speeds [Huhle et al. 2015]. Using an increased image magnification and a high-intensity fiber-coupled mercury lamp to maximize the information in each image, and an efficient and accurate tracking algorithm executed in parallel between their processing computer's CPU and GPU, Huhle et al. were able to resolve 0.3 nm steps of a piezo-driven fixed bead and a magnetically trapped bead, demonstrating a speed and resolution comparable to BFPI for the first time.

Drift-Resistant Image Tracking

Due to the host of challenges and limitations involved in performing position detection using back focal plane interferometry with back-reflected light, and our desire to construct a versatile and integration-ready instrument compatible with a variety of reflective surfaces, we chose to pursue image-based particle tracking for our instrument's position detection. Our initial implementation, as a proof of concept demonstration, has been performed without the use of specialized equipment. A schematic of the imaging configuration is shown in figure 2.12. We use a high-end EMCCD camera (Andor iXon Ultra 897) intended for low-light fluorescence applications and connected through a USB 3.0 interface, illumination with either a standard 20W halogen lamp (Nikon C-DSLS, transmission mode) or LED (Luxeon MR-B0040-20S, 70 lumens 470 nm, reflection mode), and process images offline using custom-written LabVIEW software (see section 4.3). We anticipate the implementation of a high-speed CMOS camera with embedded, real-time image processing via FPGA in the near future.

In order to use image tracking to measure forces on optically-trapped particles, we must measure their displacements relative to their trapping centers. Thus, while simply tracking a trapped microsphere with nanometer precision is a challenge, this is not enough. We must be able to track a trapped microsphere with both precision *and* accuracy, and we must also know the positions of our traps with similarly-high

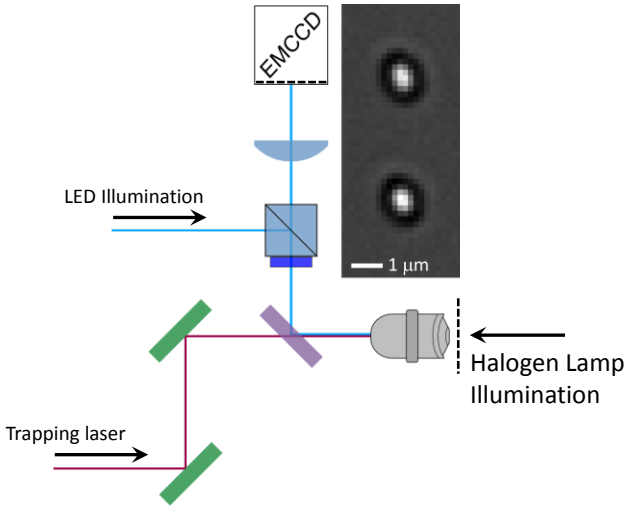

Figure 2.12 – Image Tracking Configuration
Images are acquired on an Andor iXon Ultra 897 EMCCD camera connected through a USB 3.0 interface. The camera is mapped to the objective sample plane via a 300 mm focal length lens, giving a total of 90x magnification when combined with the 60x water immersion objective. The result is a scaling of 177.1 nm per pixel in the y direction, along the axis of motion and force in our dual trap. Imaging may be performed in reflection mode with an LED emitting at 470 nm, or with a 20 W halogen lamp located above the objective for transparent samples.

degrees of precision and accuracy, in order to make a relative measurement of bead displacement within a trap. For a typical configuration, this requires knowing both bead and trap position to within 0.01 pixels[1]. In fact, this feat of image tracking has never been demonstrated at nanometer resolution in an optical trap. Most of the successes with IBPT have been in magnetic trapping instruments, which do not have a defined trapping center (force measurements are made by measuring the variance of the magnetically-trapped bead motion over time). Additionally, most claims of nanometer resolution indicate the variance in the position measurement of a *fixed*

[1] For a magnification of 100x and a pixel size of 10 μm (scientific cameras typically have pixels between 5 and 15 μm in size), one nanometer corresponds to 0.01 pixels.

bead, which does not reflect the effects of systematic errors in tracking algorithms, nor how accurately a particle can be tracked while moving, which is also effected by instrument stability relative to measurement bandwidth.

We can directly determine the location of an optically trapped bead in any given frame, but we have no direct measurement of trap location during an experiment – this must be pre-calibrated. This can be done by holding an untethered bead in the optical trap and sweeping the trap across the AOD range while tracking bead position (figure 2.13a). The trap is moved slowly to eliminate offset due to viscous drag, and to average multiple frames together for increased precision. The resulting data (figure 2.13b) can be used either as the source of a linear fit, or as a LUT to determine trap pixel position as a function of AOD frequency. We can subtract the best linear fit from the tracking results to view the deviations from the baseline. How good is a linear fit as a representation of trap position as a function of AOD frequency? Figure 2.13c shows: not very! A linear fit in this case will result in tracking errors of plus or minus 10 nm. However, if these deviations are systematic, i.e. if they are persistent between multiple scans, then we can instead use this data as a LUT table to determine trap position. Figure 2.13d shows the results of subtracting a different calibration sweep from the data in figure 2.13b, after both datasets had been averaged to remove high frequency noise. It is evident that the deviations are predominately random, and a LUT will be subject to the same inaccuracies in position determination as a linear fit.

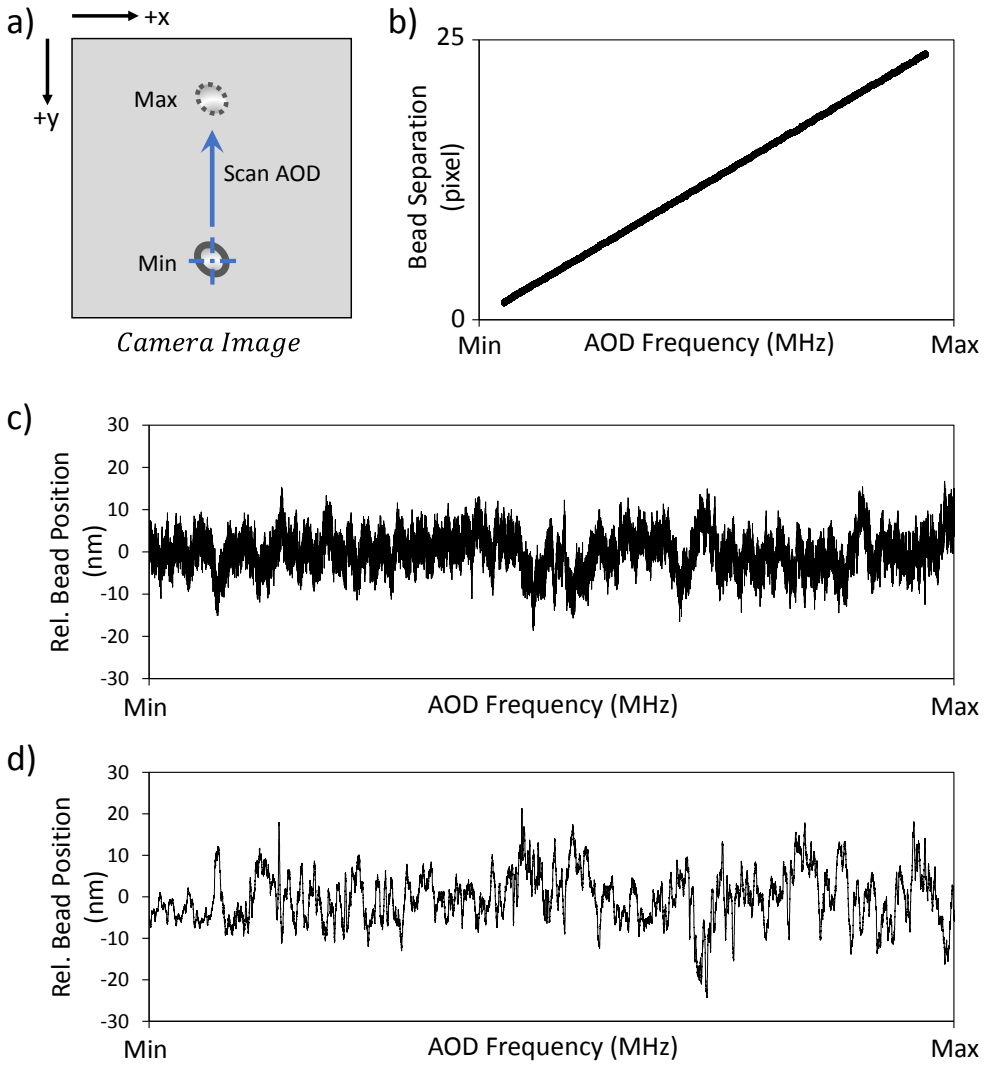

Figure 2.13 – Calibration of Trap Position via Single-Bead Scan
a) A free bead is held in an optical trap as the trap is scanned across the AOD frequency range, moving the trap across the sample plane and the camera sensor. **b)** The tracked position of the bead can be plotted versus the corresponding AOD frequency for each image frame, thus calibrating the location of the traps on the image sensor as a function of AOD frequency. **c)** Subtracting off the linear fit of the data in (b) gives the deviation from the linear model, which when converted into nanometers, is as large as 10 nm in either direction. **d)** Data from a second linear sweep was subtracted from (c) after averaging to remove high frequency noise, showing that the fluctuations are predominately random.

We have previously discussed the manner in which a differential measurement between a pair of optical traps can mitigate the effects of instrument instability and dramatically increase measurement resolution. We have developed a detection

technique which, unlike traditional dual trapping measurements, foregoes the measurement of each bead's individual displacement entirely and instead uses the tracked distance between two trapped particles as the only figure of relevance.

We first perform a calibration, analogous to figure 2.13a, to measure bead separation (rather than absolute position) as a function of AOD frequency. With an untethered bead in each trap, we hold one trap stationary at a fixed location, and scan the second trap through the remaining AOD range (figure 2.14a). We track the

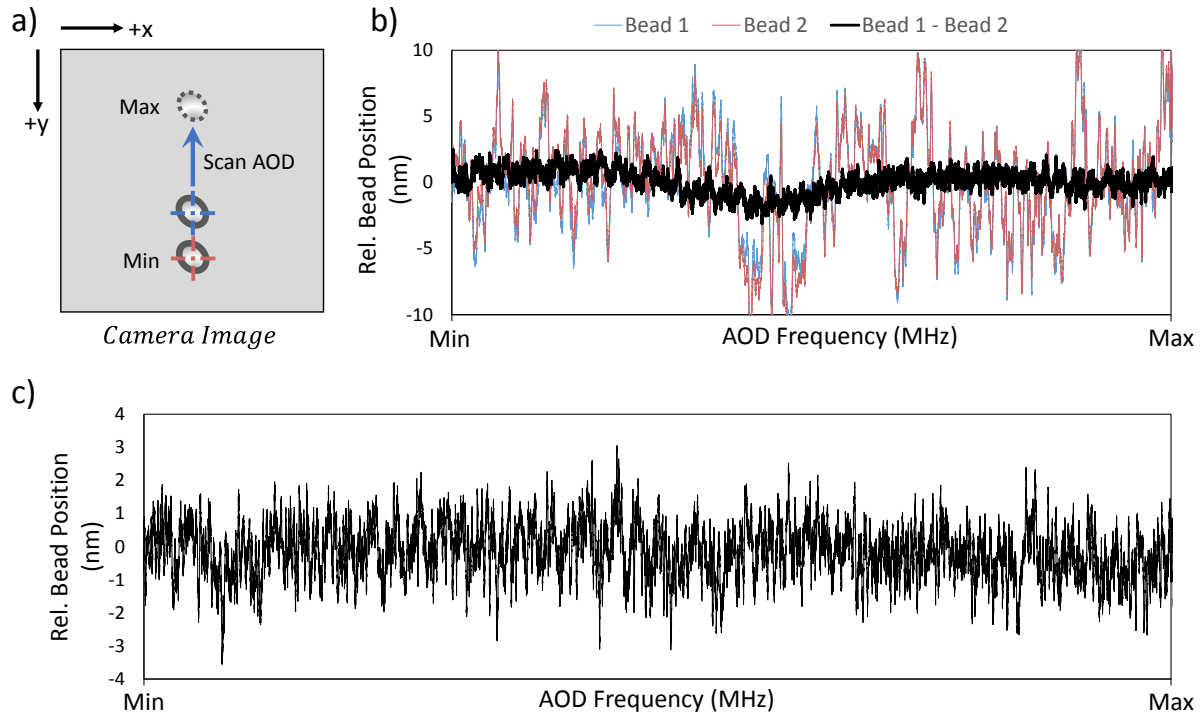

Figure 2.14 - Calibration of Trap Position via Dual-Bead Scan
a) A free bead is held in each trap. One trap is fixed at one end of the AOD range, and the other trap is scanned through the remaining AOD range. **b)** Plotting the baseline-subtracted tracked position of each bead individually (blue and red traces) highlights the large degree of correlation between the fluctuations in each signal. The black trace shows the baseline-subtracted differential signal between trap 1 and trap 2. **c)** The low-frequency variation of the dual bead signal about zero is systematic. Subtracting a second calibration scan from the first yields the residual noise, which has a standard deviation of 0.8 nm.

positions of both trapped beads to determine the distance between them as a function of the AOD frequency of the scanned trap. We can again subtract the best linear fit from the acquired data of bead separation versus trap position. In figure 2.14b we show the baseline-subtracted positions of each bead individually, and of the differential signal obtained by subtracting one bead's position from the other, highlighting the large amount of coupled noise that the technique eliminates. Additionally, the low-frequency drift about zero is, this time, systematic. In figure 2.14c, we've subtracted a separate dual-bead calibration sweep from the data in figure 2.14b. The resulting signal exhibits exceptional stability with a standard deviation of 0.8 nm. We discuss the noise and stability of our position measurements further in section 4.4. Future modifications such as shielding the laser from air currents, locking down unneeded mechanical positioning stages, and reducing noise in our RF signal generation may yield further improvements to our resolution limit.

When experiments with a biological substrate are performed, we again fix one of the two traps at the same position as in the calibration, then manipulate the sample via movement of the second trap. We use the AOD frequency of the moving trap during the experiment as the index for a LUT provided from a free bead calibration sweep. The calibration trace tells the separation we would expect from two beads without any applied force. Half of the difference between this distance, and the one we measure between two beads during an experiment, represents the average displacement of the

beads in their respective traps for that frame. Because this detection technique never relies on an absolute measurement of position and only measures the relative displacement between two beads, it drastically reduces the extreme sensitivity to mechanical drift and laser pointing instability from which standard image-based tracking methods so badly suffer. The resulting measurement stability is on par with back-focal-plane interferometry for a single bead (figure 2.15).

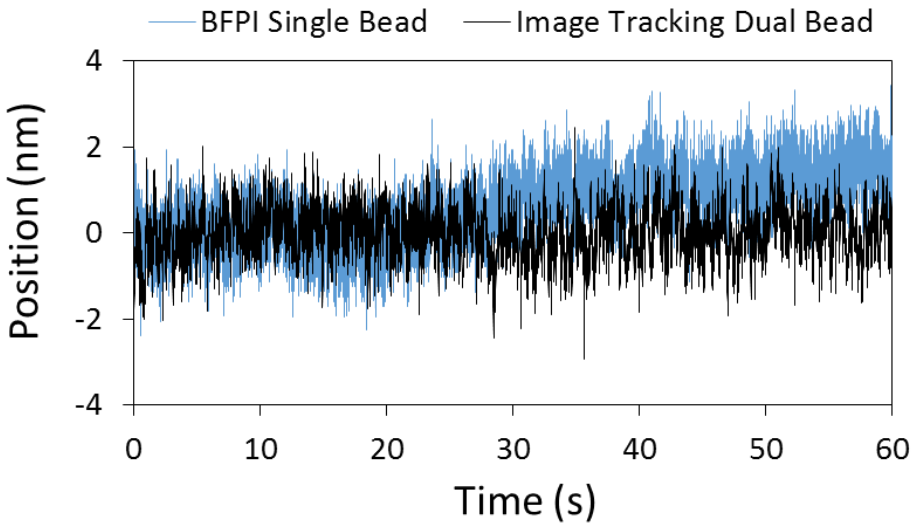

Figure 2.15 – Stability of Dual-Bead Image Tracking vs Single Bead BFPI
A differential measurement to determine relative bead position in the trap using image-based tracking shows an accuracy and drift resistance on par with the technique of BFPI for a single bead.

2.6. Software

The instrument control software was written in LabVIEW 2015. Like all languages, LabVIEW (LV) has its strengths and weaknesses. It is relatively easy to learn, and individuals without prior programming experience can quickly interface

with almost any hardware component. As a visual language, LabVIEW code depicts the flow of data through the functions that operate on it, which is a natural design for data-driven instruments. In contrast to this data-flow-driven model, most other traditional line-written languages are control-flow-driven, in that the execution order of functions acting on data is explicitly written. LabVIEW's data-flow design allows it to be inherently parallel in that sections of code without data dependency will execute in parallel without any direction by the developer. Finally, memory allocation is by default handled by the LabVIEW compiler, saving valuable development and debugging time.

On the other hand, a traditional language like C lends itself to more precise low-level control and offers performance advantages for many computationally-intensive tasks, but with a steep learning curve that can make certain applications out of reach for developers without the appropriate background and experience. Whether this is a pro or a con is up to debate – while LabVIEW may be ideal for quickly designing measurement and control applications by inexperienced users, this very advantage can become a disadvantage with larger, more complex programs. Without proper care and good design practices, the non-serial nature of LabVIEW code can result in a mess of tangled wires so difficult to discern that it is often easier to rewrite an entire application from scratch than to debug someone else's existing work (Figure 2.16). This problem is so common that it is often cited as a disadvantage to the LabVIEW

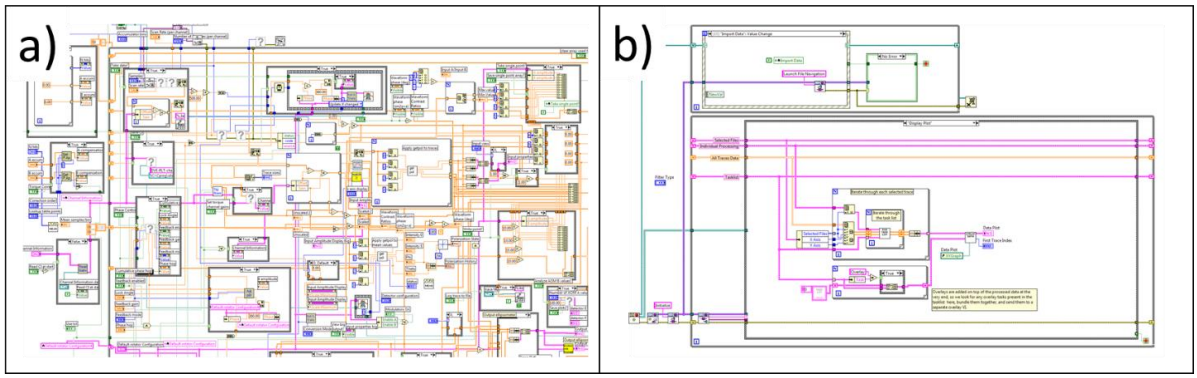

Figure 2.16 - Spaghetti Code vs Clean Code
Two LabVIEW programs of similar complexity but different levels of organization, demonstrating the effects of a careful consideration to design patterns and application architecture **(b)**, or a lack thereof **(a)**.

language itself, but this is simply not true. "Best practice" coding conventions for LabVIEW exist, and with proper design, care, and forethought, large-scale applications can be developed that are modular, well-documented, easy to debug, and easy to scale.

Application Framework

To run an optical trapping instrument, the LabVIEW software must provide a user interface (UI) through which researchers can manipulate biological samples and design experiments, execute those experiments through the control of diverse instrument hardware, acquire data from various sensors, process the collected data in real time when necessary to accommodate feedback tasks, and rapidly save data to disk for post-analysis. These complex demands require careful consideration be given to the top-level software architecture. The added computational burden of large image

data, which must be acquired from the camera, processed to extract bead positions, and saved rapidly to disk, provides unconventional demands that traditional optical tweezers software frameworks are not equipped to handle. A queued message handler (QMH) architecture was developed for this project to enable parallel and independent, yet synchronized acquisition, control, and logging tasks.

As an application grows, it makes sense to take advantage of LabVIEW's inherently parallel execution and divide tasks up into independent loops. For example, if we have a data acquisition task and a data analysis task, a naive implementation might place the analysis in sequence with the acquisition in the same while loop. This determines our loop execution rate as the inverse sum of the time it takes each of these two tasks to execute in sequence. As analysis tasks become more complex and take longer to execute, this implementation bottlenecks both our data acquisition rate and our data analysis rate. By dividing these tasks into two independent while loops, the rate of each is improved and made independent of one another. However in this example, we still need a way to pass data from the acquisition loop to the analysis loop without wiring an explicit data dependency which would cause the loops to execute in series.

The QMH is a framework for allowing communication between otherwise independent sections of code running in parallel without data dependency. It relies on two, complementary LabVIEW synchronization constructs; the Queue (LVQ) and the

Notifier (LVN). Once created, both Queues and Notifiers hold data that is written to them, and this data can then be read in other parts of the software. The LVQ holds an arbitrary number of data elements of a designated type in a "first in, first out" (FIFO) manner. When a data point is written by a producer, it is added to the end of the queue, increasing the number of elements currently in the queue by one. When a data point is read by a consumer, it is removed from the front of the queue, decreasing the number of elements currently in the queue by one. The LVN, in contrast, stores just one element, and neither reading nor writing data changes the number of data points in the notifier. When a new data element is written to a LVN, it overwrites the previous data element. Thus, the LVQ is a "many to one" structure that transfers data losslessly between any number of producers and a single consumer, which receives every element placed into the queue, and the LVN is a "one to many" structure that transfers data with potential loss to any number of consumers. Because LVQs and LVNs are not connected with wires, consumers can monitor them for new data without introducing a data dependency.

Implementation

The instrument software is divided into a number of independent and parallel loops, the primary of which are for registering UI events, handling UI events, image acquisition, image processing, image saving, data acquisition, data processing, and data

saving. Each of these loops acts as the sole consumer of a unique LVQ which is used to communicate between loops and synchronize the application. The data type of these special communication queues is defined as a cluster containing a message (string type) and any associated data (variant type). The structure of each loop is to monitor their communication queue for new items, and when a new item arrives, conditional code is executed conditionally based on the instructional content of the message item, using the value parameters contained in the data item.

In addition to the communication LVQs, a LVQ for image data and an LVQ for instrument data pass these items from their respective acquisition loops to their respective saving loops when a record is in progress, ensuring that data is saved without loss and in a manner that does not slow down acquisition or processing rates. For live instrument analysis updates, we do not require that every raw data point is processed and displayed, so LVNs are used to transfer acquired data to their processing and analysis loops, and then transmit processed data back to the main UI loop for display or further action. This allows data to be processed and shared between all loops running data-dependent tasks, without affecting acquisition or logging speeds. Additionally, the update rates of all data processing and data display tasks can be independently limited, saving valuable CPU cycles for more time critical tasks.

FPGA

An FPGA (National Instruments PCIe-7852R), also programmed with LV 2015, controls the AOD to determine the positions and powers of the optical traps in the sample plane. We describe the software for trap modulation in detail in section 2.3. We also use the FPGA to coordinate other high speed control and acquisition tasks, including differential trap power measurement and feedback stabilization (described in section 2.4), the modulation of AOMs and LED drivers for interlacing fluorescence excitation and 2-channel imaging respectively (described in section 2.2), and the precise synchronization of image data with trap position and power. We discuss the synchronization between image data and trap data here.

During an experiment, we may wish to read out both a trapped particle's position and the trap frequency location in order to calculate a force, however simply grabbing the most recently acquired data point for each item provides a sufficient time resolution on par with the camera exposure time of ~2 ms for low resolution feedback tasks and data display.

For post processing, however, we would like to know precisely the AOD driving frequencies and amplitudes that occurred over the course of each exposure. We accomplish this by monitoring a TTL output sourced from our camera, sent as a digital input to our FPGA, which allows us to count camera exposures. The TTL

output, called "Fire Out" by Andor, is high while an exposure in in progress, and low while image data is being transferred to the storage register for amplification and readout. Monitoring the status of this lines allows the FPGA to maintain a frame count, and to know precisely when each exposure begins and ends. Thus the data output by the FPGA and saved to disk contains, for each time point, the powers (AOD amplitudes) and positions (AOD frequencies) of both traps at that time, as well as a number which represents either the frame number of an exposure that is currently in progress, or is zero if the camera is between exposures or not currently acquiring. When a recording is finished, the software automatically parses the master data file containing the raw, unfiltered signals and generates a second "frame data" file, containing the average of each measured data column across each exposure and discarding data points between exposures. We have tested and verified that this synchronization is accurate to within the speeds detectable by our imaging rates. Thus our instrument generates a pair of data files for each recording session: one at an unfiltered maximum acquisition frequency, and a second that accurately filters all instrument data to the camera framerate, synchronizing each filtered data point to its appropriate camera exposure.

3. Constructing and Labeling Fluorescent DNA Dumbbell Templates

DNA is manipulated in our optical trapping instruments via polystyrene beads to which the DNA is attached. In a single trap configuration, one end of a target DNA template is attached to a microscope coverslip, and the other end is attached to a bead which can then be trapped and manipulated. These attachments are typically realized by labeling complementary surfaces with complementary molecular agents that bind each other with (ideally) high strength and high specificity. The streptavidin/biotin [Weber et al. 1989] and digoxigenin(dig)/anti-digoxigenin(anti-dig) [Kessler 1991] combinations are fairly ubiquitous for this purpose.

In a dual optical trap, each end of a DNA template is attached to a different bead using a unique label pair, one bead is held in each trap, and the DNA strand is suspended between the two. This configuration is referred to as a dumbbell. For our experiments, we purchase carboxylated beads 500-nm in diameter, and from these we synthesize both streptavidin-coated beads and anti-dig coated beads. We synthesize DNA templates of various lengths and sequences with one or multiple biotin tags at one of the DNA ends, and one or more dig tags at the other. This is usually done by performing a PCR reaction with dig- and biotin-labeled primers, or by sequentially cutting each end of the DNA template with a restriction endonuclease that leaves an

overhang, followed by a klenow fill-in reaction using a dig- or biotin-labeled dNTPs [Roche 2006].

When constructing a DNA template with fluorescent labels, the wide variety and availability of streptavidin-linked reagents is noteworthy. Because of this reagent availability, it may in some cases be desirable to use the biotin/streptavidin pair to bind a streptavidin-labeled fluorophore to a biotinylated DNA template, in which case an alternate molecule pairing needs to be used to attach DNA to bead. The fluorescein (fluor)/anti-fluorescein (anti-fluor) combination [Bird et al. 1988] was utilized in this work.

There are numerous options for synthesizing a DNA template with fluorescent labels for manipulation in an optical trapping instrument, the choice of which depends on factors such as template length, number of desired labels, and whether label placement should be random or precise. The long lengths of DNA templates in single-molecule assays (typically several to tens of kilobase pairs (kbp)) limit the options for template purification, typically to spin columns, precipitation, or gel purification, which makes synthesizing a labeled template more challenging [Linpinsel and Conn 2012]. If the labels may be randomly located along the DNA template, nick-translation [Rigby et al. 1977] and PCR with fluorescent dNTPs [Tasara et al. 2003] are potential options which we will discuss. One may also use intercalating nucleic acid stains such as the TOTO, SYBR, and STYOX families of dyes, however

these are often incompatible with single-molecule studies on DNA and DNA-based proteins as they alter the mechanical properties of the DNA [Biebricher et al. 2015].

Many choices exist as well for site-specific template labeling, with a common theme being the formation of a hybrid structure between the DNA and a tertiary agent with sequence specificity. This category includes triplex forming oligonucleotides (TFOs) [Knauert and Glazer 2001], peptide nucleic acids (PNAs) [Wang et al. 1996], and the sequence-targeted binding of labeled proteins [Dylla-Spears et al. 2009]. Nick translation can also direct sequence-specific labeling following digestion with nicking endonucleases. Short digestion times or dideoxynucleotides can be used to limit the reaction to locations vicinal to the nicks. Nick translation has also been used in this manner to form single-stranded gap sequences for subsequent annealing with a labeled oligo [Zohar and Muller 2011].

In this chapter, we describe the construction of several new DNA templates for single-molecule optical trapping studies, with both site-specific and random labeling. We conclude by discussing various techniques for labeling DNA templates with quantum dots, including a novel flow-cell design that allows us to label a template with multiple binding sites while the template is under force.

3.1. Constructing a Singly-Labeled Template

We designed and constructed an 8-kpb DNA template with dig- and fluor-labeled ends and a single, biotin-labeled nucleobase in the center of the template for attaching a streptavidin-coated quantum dot (figure 3.1). Labeled primers purchased from IDT were used to PCR two, ~4-kbp segments which we refer to as "arms" from the M13mp18 plasmid [Yanisch-Perron et al. 1985]. The forward primers for both arms contain a regular annealing sequence that is 20-bp long for the template plasmid, and additionally contain a non-complementary, 27-bp tail on the 5' end. The tail contains the recognition sequence for the BstXI restriction endonuclease (RE), and in

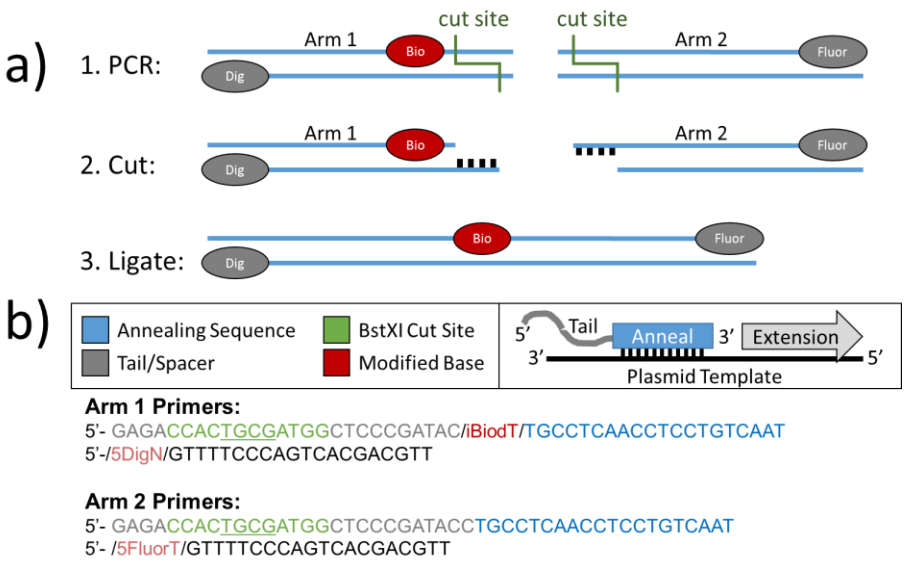

Figure 3.1 – An 8-kbp DNA Template with Central Biotin Tag
a) We first PCR two 4-kbp "arms" which each contain a cut site leaving a complementary overhang. Following restriction enzyme digestion, we ligate and then gel purify the template. The template may then be labeled by incubating with streptavidin-coated quantum dots (QD). **b)** We introduce the complementary but non-palindromic cute sites via the PCR primers, which are designed with a 20-bp annealing sequence that recognizes the plasmid template, and an added tail which is not complementary to the plasmid. The tail contains the engineered cut site, the end and central labels for attaching the DNA to beads, and a QD, respectively. We also inserted a spacer sequence between the biotin label and the cut site to ensure robust cutting and ligation.

the case of one of the arms, contains a nucleobase modified with a biotin tag. The reverse primers for the two arms contain a dig end label and a fluor end label, respectively.

After we PCR the two arms, we column purify the PCR product and then digest each arm with the BstXI RE, followed by another column purification to remove the RE. The digestion leaves a four-bp overhang on each arm that is complementary to the other arm, but non-palindromic to prevent self-ligation within each arm. The two arms are combined and ligated together, and then a gel purification is performed in the final step to separate the 8-kbp template from the 4-kbp arms that remain un-ligated. The template may be labeled with streptavidin-coated quantum dots (Life Technologies Q22063), as described in more detail in section 3.3, either before or after formation of the tethered construct. Figures 3.2a and 3.2b show gel electrophoresis results for the template fabrication process. The ligation proceeds with good yield when the PCRs of the two arms are of high quality. The final product after gel purification is just over 8 kbp in length. We refer to this template as "8kbQD". In figure 3.2c, we have incubated the template with streptavidin-coated quantum dots to attach a QD to the central biotin tag, and then formed a dumbbell tether in a dual optical trap. The figure was obtained using the 2-channel imaging technique described in section 2.2, and is the sum of a brightfield (cyan) image of the trapped beads, and a

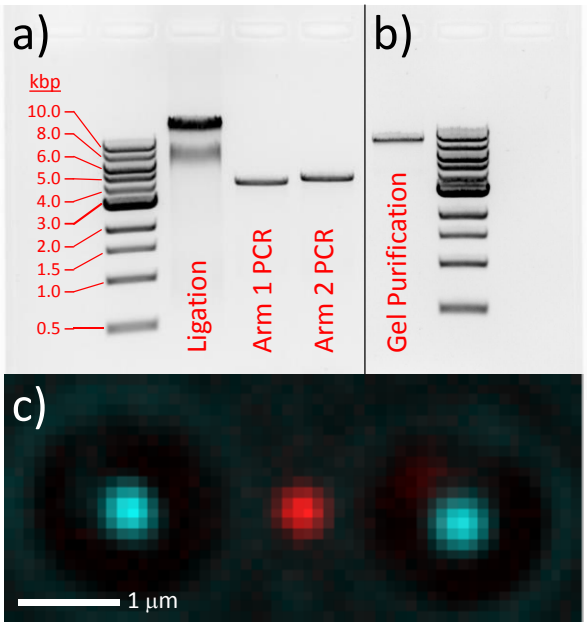

Figure 3.2 – The 8kbQD Template Fabrication and Results
a) Arms 1 and 2, just over 4kbp in length, are PCRed with primers that introduce an engineered cut site for the non-palindromic BstxI restriction enzyme, as well as a dig and biotin tag on either end of arm 1, and a fluor tag on the end of arm 2. The arms are cut and then ligated. The ligation proceeds with good efficiency as shown here when the arm PCRs are of high quality. **b)** The finished template, which we call "8kbQD," after gel purification of the ligation product. **c)** A combined brightfield (cyan) and fluorescence (red) image shows the successful formation of a dumbbell tether using the 8kbQD template after the central biotin tag has been labeled with a streptavidin-coated quantum dot. The trapped beads are visible in cyan in the brightfield image, and the emitting quantum dot is visible in red at the center of the DNA tether that bridges the two beads.

fluorescence (red) image of the emitting quantum dot located in the center of the DNA template which spans the two trapped beads.

To generate a long DNA template with a well-defined, central fluorescent label, this technique has some strengths, and some weaknesses. Both the end and central tags on the template are incorporate through PCR primers which are HPLC-purified by the manufacturer, leading to a very high label incorporation efficiency. The exact location of the central biotin label is known to the base-pair. Thus, the labeling of this

template is both precise and robust. Although it would stand to reason that this technique could also be used with a primer containing an embedded dye rather than a biotin tag, we attempted this process with a primer containing an internal Cy5 label but could not obtain a suitable ligation yield, despite the large spacer between the dye location and ligation site. It is worth noting then that some dye modifications may inhibit enzyme activity. The PCRs for this template may additionally present a challenge due to the long, non-complementary sequence in the forward primers, and the overall length of the total primer. The primers required careful design to mitigate mis-priming and secondary structures exacerbated by their high melting temperatures and non-sequence-specific tails, and the PCR protocol required extensive optimization.

3.2. Constructing a Multiply-Labeled Template

Label Incorporation by Nick Translation

It can be useful to generate a DNA template with multiple labels along the sequence, as single dyes are challenging to work with due to their low brightness and limited lifetime. Nick translation (figure 3.3) is one technique capable of introducing multiple modified nucleobases randomly along double-stranded DNA (dsDNA). Nick translation takes advantage of the 5' to 3' exonuclease activity of the DNA

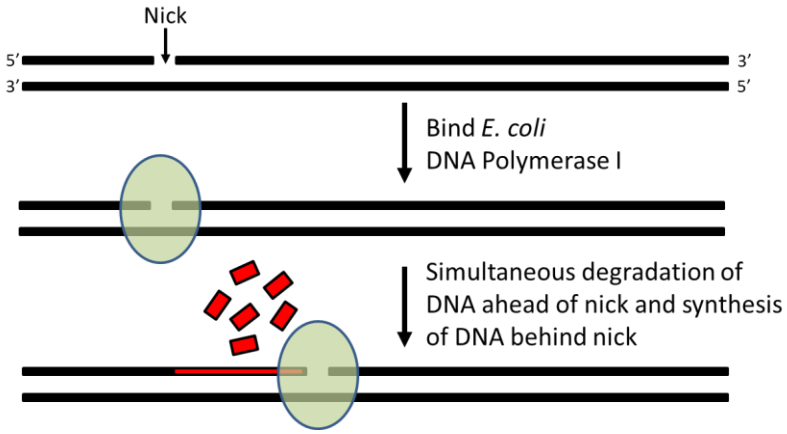

Figure 3.3 – Nick Translation
DNA Polymerase I (Pol I) binds to nicks in double-stranded DNA. Pol I has a 5' to 3' exonuclease activity that allows the enzyme to excise bases ahead of the nick, and incorporate new bases via polymerization behind the nick. The nick is thus translated in the 5' to 3' direction, incorporating deoxynucleotides (dNTPs) from the surroundings. If modified dNTPs are included in the reaction, they will be incorporated at random locations downstream of nicking sites.

Polymerase I enzyme, allowing it to excise bases in front of a nick while incorporating deoxynucletodies (dNTPs) from its surroundings to the 3' side of the nick behind it. If modified dNTPs are included in the reaction, they will be incorporated into the template. Nick translation is commonly used after DNA digestion with the general DNA degradation enzyme DNase I to generate short, randomly-sized fluorescence hybridization probes [Kato et al. 2006], however it has not been adapted for use in generating long, multi-labeled single-molecule templates. We investigated whether this technique was compatible with the requirements of single-molecule templates for introducing multiple modified dNTPs into a long dsDNA sequence.

For single-molecule assays, a targeted nicking enzyme which preserves template length needs to be employed. In general, restriction endonucleases bind as a dimer to

a specific DNA sequence, and act in cooperation to hydrolyze both strands of the DNA duplex at the same time. Nicking enzymes are synthesized from regular restriction endonucleases by incapacitating one of the two enzyme units so that only one side of the DNA strand is cut, creating a nick at a precise location relative to the enzyme's recognition sequence. Unfortunately, we found that nicking enzymes may still cut both sides of a DNA template to a significant extent when digestions are performed at the recommended reaction conditions. In order to examine the extent to which full cutting occurs under various reaction conditions, we performed a series of gel nicking assays with the nicking enzyme Nb.BbvCI (NEB R0631S).

A supercoiled plasmid migrates faster through an agarose gel when an electric field is applied than a linear DNA strand of the same length, due to the condensed size of the supercoiled structure. Nicking a circular plasmid, however, allows the plasmid to fully uncoil into a ring, and in this state it runs slower on a gel than its linearized counterpart. If a nicking enzyme cuts through the dsDNA strand entirely rather than just nicking one side, the plasmid will be linearized, which is activity we want to avoid. A regular gel can thus be used to assay the extent to which an enzyme nicks and linearizes plasmid DNA under various conditions. We examined Nb.BbvCI nicking on a 10 kbp template with three engineered Nb.BbvCI nicking sites within a 60-bp span, using varying amounts of nicking enzyme and varying digestion times. It is recommended by the manufacturer to run a digestion using an amount of enzyme

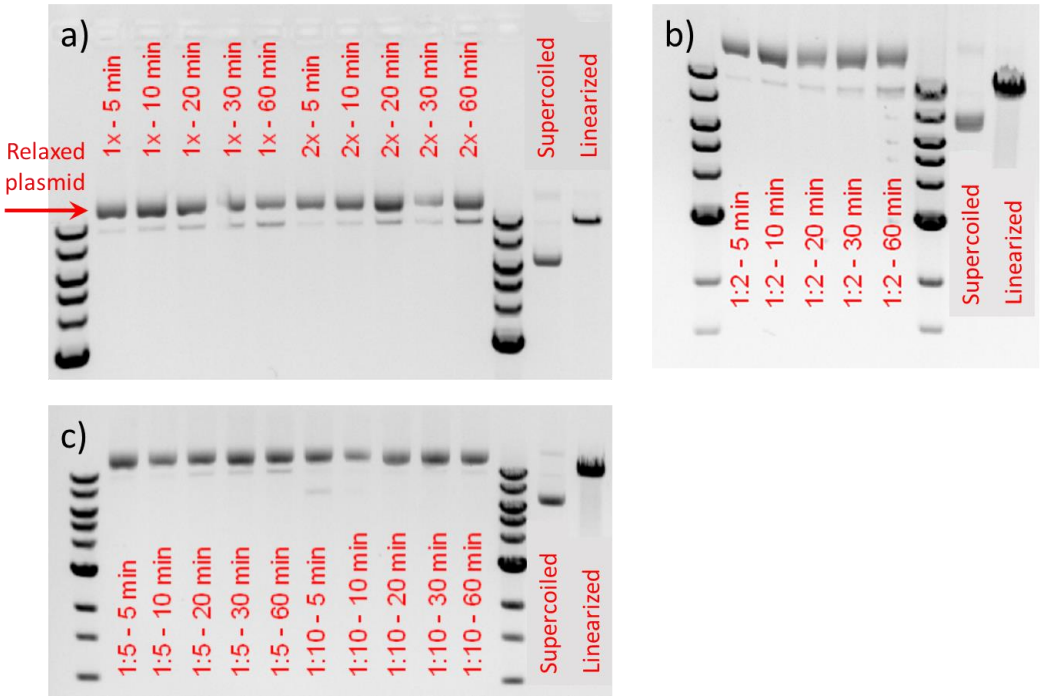

Figure 3.4 – Time-Series Gels to Assay Nicking Endonuclease Activity
A supercoiled plasmid, nicked (relaxed) plasmid, and a linearized plasmid all run at different rates through an agarose gel. We assayed the activity of the nicking enzyme Nb.BbvCI on a 10 kbp DNA template in which three nicking sites are located in a 60-bp stretch, at varying digestion times and concentrations. The concentrations are relative to the manufacturer-recommended amount ("1x"), and all digestions were carried out at 37 °C. **a)** Digestions at the recommended concentration, and a 2x over-digestion which is commonly done to ensure complete cutting, show that the template is 100% digested and partially linearized after just 5 minutes of a reaction. The standard reaction conditions (1x for 60 minutes), results in around 50% linearization of the template. **b)** The plasmid is also fully digested after 5 minutes when the enzyme is diluted by a factor of 2. **c)** Partial digestion of the supercoiled plasmid was finally achieved after a five-minute digestion with the nicking enzyme diluted by a factor of 10. At this concentration, we were able to digest for the recommended 60 minutes without inducing significant linearization.

which we refer to as 1x, and incubate the enzyme at this concentration with DNA for one hour at 37 °C. We ran digestions at the 1x and 2x concentrations, as well as dilutions by factors of 2, 5, and 10. We removed aliquots of the digestion reactions after digestion times of 5, 10, 20, 30, and 60 minutes, and heated the samples to deactivate the enzyme. The results of these samples run on an agarose gel are shown in figure 3.4.

After only 5 minutes of incubation at the recommended concentration ("1x", figure 3.4a), the supercoiled plasmid was completely digested into nicked and linearized components. At the recommended reaction conditions (1x enzyme and a reaction time of 60 minutes), the supercoiled plasmid was almost 50% linearized. Dilution of the enzyme by a factor of 2 (figure 3.4b) reduced linearization slightly, but significant linearization still occurs. Using a ten-fold enzyme dilution (figure 3.4c), we were finally able to achieve conditions of partial plasmid digestion with an incubation time of five minutes. After 20 minutes at these conditions, the plasmid was fully nicked. A ten-fold dilution allows the plasmid to be digested for 60 minutes without significant linearization. From this assay, we determined that a digestion time of 30 minutes with a ten-fold reduction in enzyme concentration achieves complete template nicking while minimizing linearization.

Using the optimized conditions determined by the nicking gel assay, we digested a ligated (circular) lambda DNA template with Nb.BbvCI and subsequently performed nick translation in the presence of Alexa Fluor® 647-aha-dUTP (Life Technologies A32763). Although this was successful in labeling the DNA, we also observed that the nick-translation caused smearing of the DNA template on agarose gel, indicating DNA length reduction through degradation (figure 3.5a). Although not

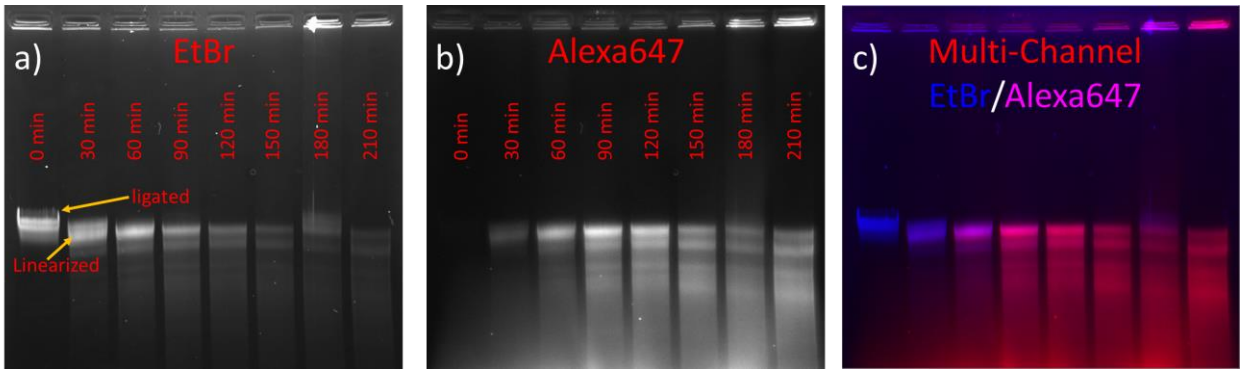

Figure 3.5 – Nick Translation Degrades DNA
Lambda DNA was first circularized through ligation, then nicked with the Nb.BbvCI nickase. The nicking enzyme was deactivated by heat, and then nick translation of the template was performed in the presence of Alexa-647-dUTP. Aliquots were removed from the reaction every 30 minutes and the reaction was stopped by heat inactivation before running on an agarose gel. **a)** The ethidium bromide (EtBr) channel shows significant DNA degradation after 60 minutes. Additionally, the initially circular template is entirely linearized after 30 minutes, indicating the presence of random nicks on the template strand. **b)** The Alexa-647 channel shows the incorporation of fluorescence labels into the template DNA by Pol I. Significant incorporation is visible after 90 minutes. **c)** The EtBr (a) and Alexa-647 (b) channels combined.

typically mentioned in nick translation protocols, the DNA Pol I enzyme has a 3' to 5' exonuclease activity [Beese and Steitz 1991], in addition to the 5' to 3' exonuclease activity that propagates a nick during nick translation. Consequently, the combined exonuclease activities of Pol I degrade the ends of linear DNA [Cooper 2014]. This reaction is slow relative to the polymerization activity that translate a nick during strand synthesis, and the enzyme can be biased towards nick-translation using a high concentration of dNTPs and short reaction times.

To investigate these activities of Pol I, we performed a time series gel assay of a nick translation reaction run on lambda DNA. We first ligated the lambda DNA to form a circular plasmid, then nicked the DNA with Nb.BbvCI, then deactivated the nicking enzyme with heat. We then performed nick translation in the presence of

Alexa-647-dUTP and examined the reaction progress by agarose gel. The results are shown in figure 3.5. Figure 3.5a visualizes the presence of DNA through an ethidium bromide (EtBr) stain, while figure 3.5b visualizes the incorporation of fluorescent Alexa-647-dUTP, and figure 3.5c combines these channels to illustrate the competing rates of these two enzyme activities.

After 30 minutes of nick translation, our circular plasmid became completely linearize (figure 3.5a). It is therefore likely that random nicks were introduced into the dsDNA template during the nicking reaction and subsequent heat inactivation of the nicking enzyme. As DNA Pol I translates a nick through the extension strand, if it encounters a nick on its template strand, the DNA in front of and behind the enzyme will be disassociated at this point, introducing a double-stranded break (figure 3.6). Additionally after 30 minutes, significant smearing below the main template band is evident, showing template degradation which increases in severity with time. The Alexa-647 channel of the gel (figure 3.5b) shows the degree to which fluorescent labels are incorporated into the template DNA by Pol I. Extensive labeling occurs by 90 minutes of reaction time, at which point the DNA is already significantly degraded.

Two points are made quite clear by this experiment in regards to the use of nick translation as a technique for generating single-molecule DNA templates for optical trap tethering. First, the reaction must precede the addition of the end labels used for attaching DNA to beads, because the nick translation reaction will strip any tags in

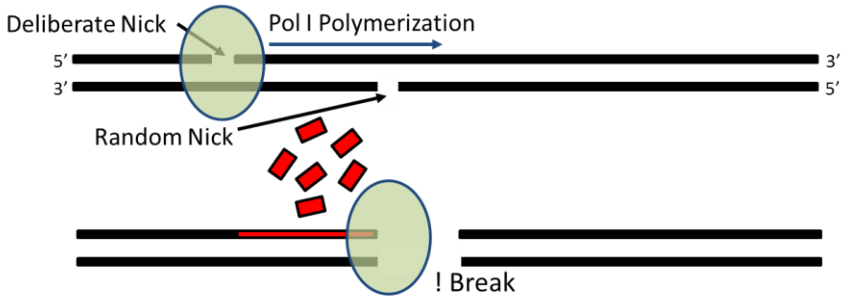

Figure 3.6 – Nick Translation can Cause dsDNA Breaks
The mechanism by which the nick translation reaction induces dsDNA breaks. A nick in the polymerization strand enables nick translation, however if Pol I encounters an unintended nick in the template strand, separation occurs.

place from the DNA ends through end degradation. Second, extended nick translation reactions are not compatible with single-molecule template generation unless one can robustly generate nicks on only one strand of a circularized DNA template, which may prove to be a prohibitive challenge. We thus deem nick translation unsuitable for the generation of single-molecule templates in which fluorescent labels are randomly incorporated along the full length of the template.

Label Incorporation by PCR

Polymerase Chain Reaction (PCR) can alternatively be used to incorporate fluorescent labels into a dsDNA template. PCR is a technique for amplifying regions of DNA. A DNA template is first denatured into two strands through heat, and then cooled in the presence of excess ~20-bp "primer" sequences which flank the region of interest on the template DNA to be amplified (the amplicon). A thermophile DNA

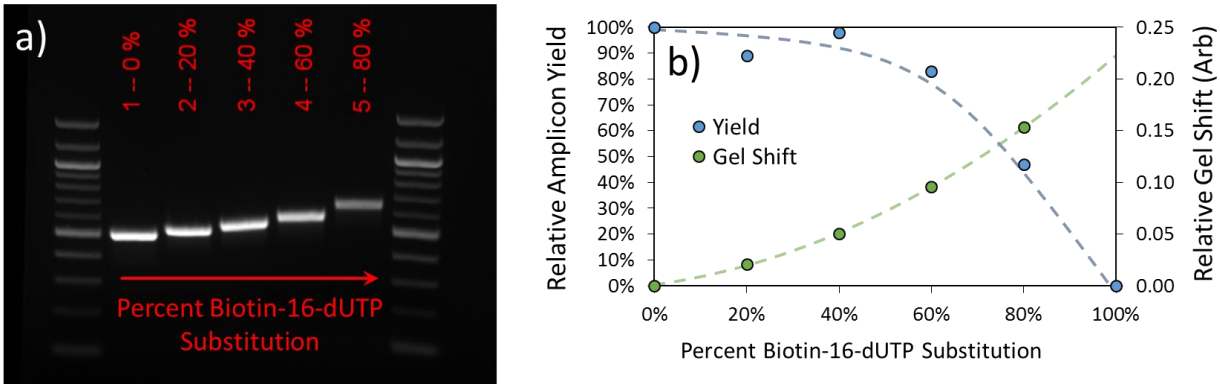

Figure 3.7 – Biotin-16-dUTP Incorporation by Long-Amp® PCR
a) Biotin-16-dUTP was substituted for dTTP in a PCR reaction at varying relative amounts. The incorporation of the modified nucleotide shifts the resulting gel band of the PCR product. Additionally, amplicon yield drops as substitution rates approach 100%. 100% substitution of a modified nucleobase is known to cause PCR failure. **b)** Band intensity, corresponding to PCR amplicon yield, and gel shift, corresponding to modified nucleobase incorporation, are plotted relative to the unsubstituted PCR band in lane 1, as a function of modified base incorporation ratio. Note that the relative gel shift cannot be used to quantitate incorporation efficiency without additional information, such as the gel shift of a 100% incorporated PCR.

polymerase enzyme which can survive the heat denaturation of the template then extends the primer sequence in the 5' to 3' direction, incorporating dNTPs from its surroundings complementary to its template strand. The reaction beginning from heat denaturation is repeated for around 30 cycles, doubling the moles of target DNA in each reaction cycle.

Modified dNTPs included in the reaction will be incorporated by polymerase into the DNA product, however it is known that if 100% of any given base is substituted with a modified version, the PCR reaction will fail. This can be seen on a gel of the purified PCR product under varying substitution ratios, which we show in figure 3.7 for a 496-bp template PCRed with Biotin-16-dUTP (Sigma-Aldrich 11093070910) replacing a varying percentage of the dTTP in the reaction. The gel

illustrates successful incorporation of the modified nucleobase by gel shift, caused by the additional bulk of the biotin molecule attached to the base by a long linker arm. Yield remains robust for substitution ratios up to around 60%, at which point yield begins to quickly drop with higher substitution ratios. It should be noted that the substitution ratio does not necessarily dictate the incorporation ratio, since the polymerase may have a preference for incorporating unmodified dNTPs, and this preference is, furthermore, likely to vary substantially for different nucleotide modifications and polymerases. The gel migration can quantitate relative changes in PCR incorporation (i.e., a lane that shifts twice as far on the gel as another probably has twice as many modified nucleotides incorporated), however without knowing an absolute calibration marker such as the gel shift caused by a single modified nucleotide, or the gel shift of the 100%-incorporated product, the shift cannot quantitate the absolute amount of modified dNTPs incorporated.

Why does yield decrease at high substitution ratios? One could hypothesize that a modified nucleotide, not being an enzyme's preferred substrate, might slow down the incorporation reaction, causing yield to drop as full extension is not achieved within the allotted thermal cycling time. Were this the case, lengthening polymerase extension times in the PCR protocol could potentially recover a portion of the lost yield, however increasing extension times is not found to improve yield [Zhu et al. 1994]. Zhu and Waggoner used a linear amplification assay to differentiate the effects

of dye-modified nucleotides in the extending strand, the template strand, and in the primer-binding region on polymerization yield [Zhu and Waggoner 1997]. They found that primer extension proceeds to completion when modified nucleotides are present on the template strand, but that the incorporation of dyes into the extending strand had a chance to cause early termination of strand extension. The likelihood of early strand termination increases in adjacently-labeled sites, and extension could not be recovered after early termination given a longer wait time. They additionally found that modifications of the DNA strand at the primer binding site affects primer binding and lowers yield.

With a mechanism of strand termination implicating the interactions of the modified base with the enzyme's catalytic activity, it is not surprising then that the results of an incorporation PCR are highly variable; they depend on the polymerase used in the PCR reaction, and on the specifics of the modification, including the modification molecule (smaller molecules tend to be better-tolerated than larger molecules), the length of the linker arm used to attach the modification (longer linker arms are better-tolerated), the site of attachment of the linker arm (major groove modifications are better-tolerated than minor-groove modifications), and the particular nucleobase (A, T (or U), G, or C) used [Tasara et al. 2003]. The Deep Vent™ strain of DNA polymerase was found to incorporate modified bases with

greater efficiency than the standard Taq DNA polymerase for all modifications examined by Tasara et al..

To generate a long DNA tethering template with multiple fluorescent labels, we first designed a PCR construct from lambda DNA. Primers[2] were selected for an amplicon 13,702 base pairs in length, which we refer to as the λ13.7 template. Taq DNA is generally not well-suited to amplicons longer than 3 to 4 kbp in length, and so we used LongAmp® Taq Polymerase (NEB M0323S) for this work. LongAmp® contains a mix of standard Taq and the Deep Vent™ polymerases that have been shown to better-tolerate the inclusion of modified bases in the PCR reaction. We optimized our PCR protocol for specificity and yield (figure 3.8), and the resulting protocol is given in table 1. We found that increasing cycle number beyond 27 made the PCR more prone to failure, and chose the conditions of 27 cycles and 5 ng of DNA template for high yield and high specificity. For four 50-uL PCR reaction tubes, our yield is consistently excellent (at least 25 μg), and when the PCR is performed with end-labeled primers for attaching the template to beads or a coverslip, we find this template gives an exceptionally-high tethering efficiency relative to other templates in our experience.

[2] Forward Primer: GCT GAT GCT TGA ACC CGC CTA TGC
Reverse Primer: CTC AGT TTG CCT TCC TCC GTG TCC TC

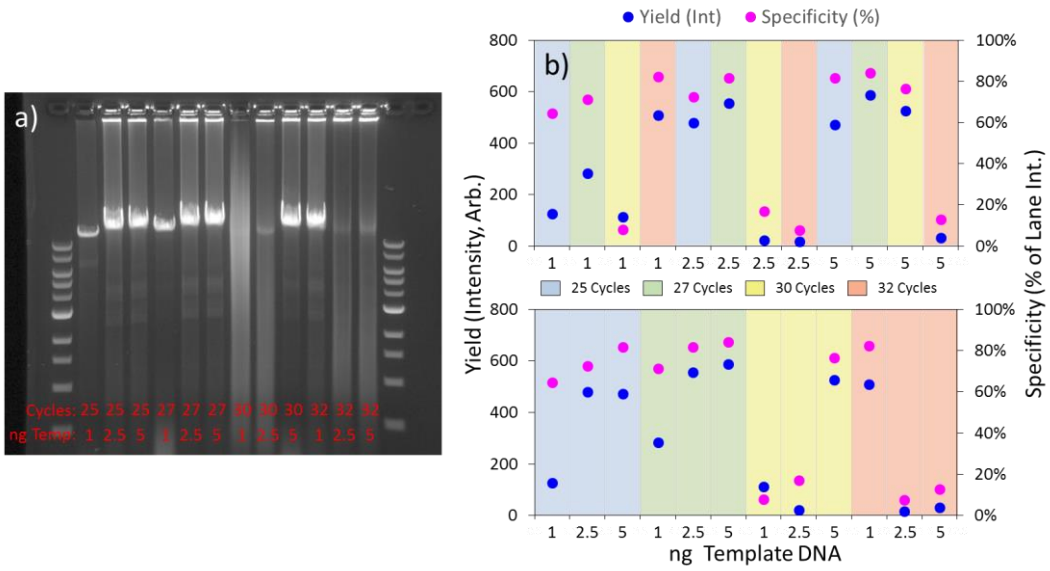

Figure 3.8 – PCR Optimization for 13.7 kbp Template

a) We ran a sequence of PCRs for the λ13.7 template in which we varied cycle number and nanograms of the lambda DNA template ("ng Temp"). The scaling of the gel has been adjusted to highlight the presence of nonspecific bands below the target amplicon at 13.7 kbp. b) From the gel data in (a), yield (integrated band intensity in arbitrary units), and specificity (band intensity as a fraction of total lane intensity) of the amplicon band are plotted for each reaction condition. The same data is shown sorted by increasing template DNA (top) and increasing cycle number (bottom).

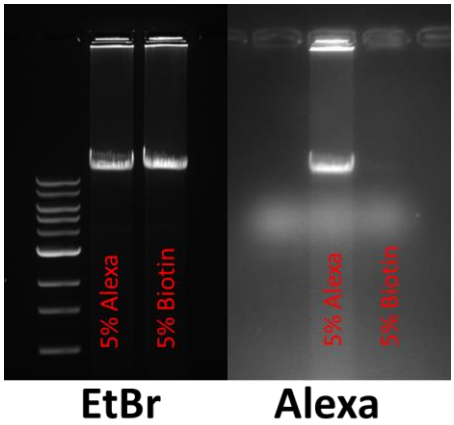

Figure 3.9 – 13.7 kbp Template PCRs with Biotin and Alexa-647

The PCRs of our final, end-labeled template for single-molecule tethering experiments. We made templates with PCR incorporation of Biotin-16-dUTP and Alexa-647-dUTP, both at a substitution ratio of 10%. The left shows the ethidium bromide (EtBr) stain of the DNA, and the right shows successful incorporation of Alexa dyes with a fluorescence gel image.

Table 1: PCR Protocol for Labeled 13.7-kbp Tether Template from Lambda DNA

PCR Preparation:

Reagent:	Amount	Stock Concentration	Final Concentration
D.I. Water:	153.10 µL		
LongAmp® Taq Buffer:	44.00 µL	5 X	1 X
dNTPs (see below):	14.52 µL	N/A	See Below
Lambda DNA Template:	2.20 µL	10.0 ng/ µL	5.00 ng/vol.
Forward Primer:	0.90 µL	100 µM	0.41 µM
Reverse Primer:	0.90 µL	100 µM	0.41 µM
LongAmp® Taq Polymerase:	4.40 µL	2.5 units/ µL	2.5 units/vol
Total Volume:	220 µL	(Makes 4x50-µL PCR tubes)	
Labeled and Unlabeled dNTPs:			
Labeled dNTP:	6.60 µL	1.0 mM	0.03 mM
Unlabeled dNTP:	5.94 µL	10.0 mM	0.27 mM
Other 3 dNTPs:	1.98 µL	33.3 mM	0.30 mM
Total dNTP Volume:	14.52 µL		

Combine reagents on ice, in the order listed, and pause just before adding the polymerase to hot-start the thermocycler. Mix by pipetting up and down several times *very* gently just before adding polymerase, and just after, until mixture is uniform by eye. Aliquot into 50-µL PCR tubes and commence the hot-start thermocycler protocol.

Thermocycler Protocol:

	Step	Temperature	Time
1.	Initial Denature:	94 ºC	3:00
2.	Denature:	94 ºC	0:15
3.	Anneal:	64 ºC	0:15
4.	Extend:	65 ºC	13:00
	GOTO Step 2 x 27 cycles		
5.	Final Extension:	65 ºC	10:00
6.	End:	4 ºC	Forever

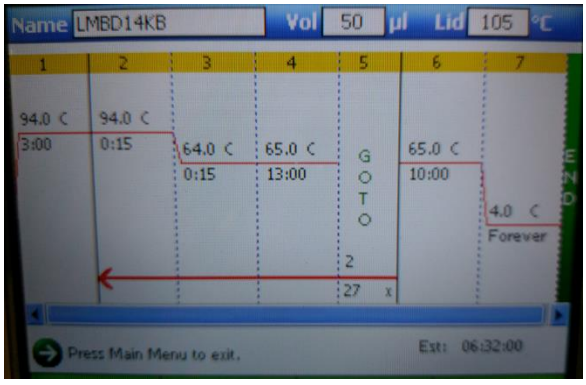

PCR products of our λ13.7 template for use in single-molecule assays were generated for a 10% substitution ratio for both biotin-16-dUTP and Alexa Fluor® 647-aha-dUTP (Life Technologies A32763). While biotin -16-dUTP showed robust PCR yield at up to 60% substitution in our preliminary assay (figure 3.7), Alexa-647-

dUTP caused PCR failure at as low as 20-30% (template-dependent, data not shown) substitution. We were able to obtain good yield for this reaction, however, when we dropped the substitution of Alexa-647-dUTP to 10% or lower. Our 10%-substituted products for our λ13.7 template are shown in figure 3.9. We will discuss the labeling of the biotinylated template with streptavidin quantum dots in section 3.3.

3.3. Flow Cells and Template Labeling

Flow Cell Construction

Dumbbell tethers for dual optical trapping experiments are constructed within a flow cell made from a glass microscope slide, coverslip, and parafilm. Our standard flow cell configuration is shown in figure 3.10. We begin by drilling the inlet and outlet holes in the glass slides using a diamond grinding bit (McMaster-CarR 4376A11) and a precision drill press (MSC M-7000). We wash then plasma clean the microscope coverslip and slide. We cut out a parafilm template defining the flow channels with a razor blade and then press it into place onto the drilled slide. Thin polyimide capillaries with an inner diameter of 50 microns (Amazon B0013HOZY6) are cut with a razor blade and positioned across the channel boundaries. Finally, the plasma-cleaned coverslip is placed over the parafilm, and the entire assembly is heated briefly under gentle manual compression on a hot plate, and then let to cool. The inlet

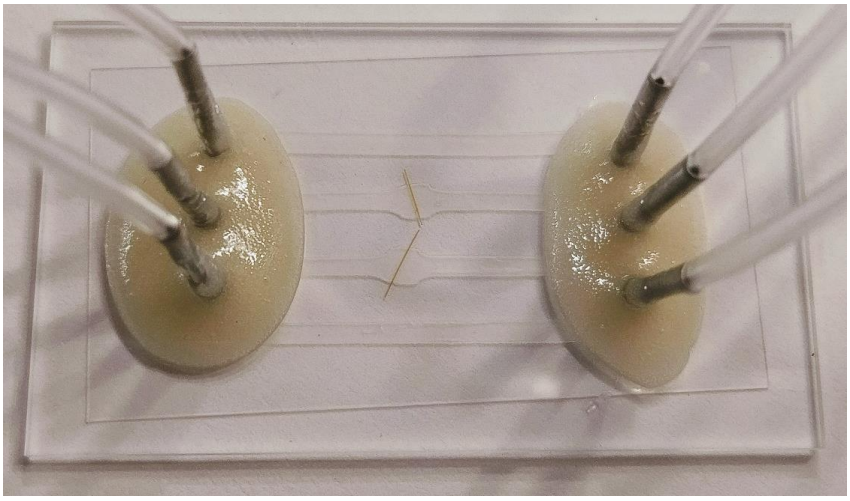

Figure 3.10 – Basic Flow Cell for Forming Dumbbell Tethers
A parafilm pattern defining the flow cell lanes is sandwiched between a glass slide, into which holes have been drilled, and a microscope coverslip. The assembly is heated to melt the parafilm, and then tubing is joined to the inlet and outlet holes via metal tubing and glued into place. Small capillaries allow tether-forming reagents to flow from the outer lanes to the central channel.

and outlet holes in the microscope slide are coupled to Tygon tubing (S-54-HL) via short segments of metal tubing (Amazon B004WPQT2C) which we cut to size, insert into the holes drilled in the microscope slide, and then fix with epoxy (The Epoxy Source 4023). We let the flow cell dry for 24 hours before use.

The flow cell is first filled with vacuum-de-gassed water, then the interior surfaces is pacified by flowing 10 mg/mL casein through each channel, before flushing each channel with the experiment buffer. De-gassing reagents, and letting all reagents come to room temperature before introducing them to the flow cell helps prevent the formation of bubbles. Reagents are pulled into a channel through the inlet tubing using a syringe drawing from the end of the outlet-side tubing. This reduces the likelihood of leaks caused by the positive pressure of injecting fluids into the flow cell. For storage, we flush each channel with half a milliliter of water, and then fill the

flow cell with a dilute sodium azide solution. The outlet are plugged and the inlets are left in a bath of this solution to prevent the flow cell from drying.

Making Dumbbell Tethers

Reagents must first be prepared for a flow cell experiment. We mix a suspension of streptavidin-coated beads, and pre-incubate a mixture of anti-dig-coated beads and template DNA (and quantum dots if applicable). In the case that a template contains one or more internal biotin tags for the purpose of binding streptavidin-coated quantum dots, we replace the biotin tag normally at the DNA end of bead attachment with a fluor tag, and we synthesized anti-fluorescein-coated beads in house to use in place of streptavidin beads for those assays. The optimal DNA:Bead pre-incubation ratio to achieve good tethering efficiency while minimizing dual tethers [Fuller et al. 2006] varies depending on the freshness and quality of the DNA template and beads, as well as the incubation time and absolute concentrations, but is generally between 1:1 and 10:1. Our incubation protocol for a standard template is given in table 2.

Tethers are made within the central flow cell channel, using reagents that flow into the central channel from the side capillaries, as shown in figure 3.11a. We have found that a simple gravity feed system works better than a syringe pump for establishing and modifying the flow rates between the channels. Flow is controlled by changing the relative heights of inlet and outlet tubing fluid reservoirs, as shown in

Table 2: Incubation Protocol for Dumbbell Tethers

Amount	Stock Concentration	Reagent	Directions
0.2 μL	1 nm	Template DNA	Combine at room temperature, flick tube to mix
9.8 μL	1x	PBS buffer	
1.0 μL	200 pM	Anti-dig beads	Combine at room temperature, vortex then sonicate 10-60s to disperse
2.0 μL	10 mg/mL	Casein	
7.0 μL	1x	PBS buffer	
Add beads to DNA, flick tube several times gently to mix. Incubate on benchtop ~20-60 minutes.			
1.0 μL	200 pM	Strep beads	Combine at room temperature, vortex then sonicate 10-60s to disperse
2.0 μL	10 mg/mL	Casein	
17.0 μL	1x	PBS buffer	

figure 3.11b. We attach the fluid reservoirs to vertical microstages to facilitate height adjustments. The low outlet in the central channel establishes the main flow direction in the system. By elevating the side channels' inlet reservoir relative to the central channel's inlet reservoir, positive pressure is maintained in the outer channels relative to the central channel, so that reagents move from the side channels, through the capillaries, and into the central channel.

We fill the left channel with the streptavidin-coated bead mixture from table 2, and the right channel with the bead-DNA pre-incubation, then plug the outlet tubing of the side channels. The downward flow of the central channel directs the reagents exiting the capillaries into well-ordered laminar flows with distinct boundaries near the capillary exits, as visible in 3.11a, where we have filled the side channels with Rhodamine dye to visualize the flows.

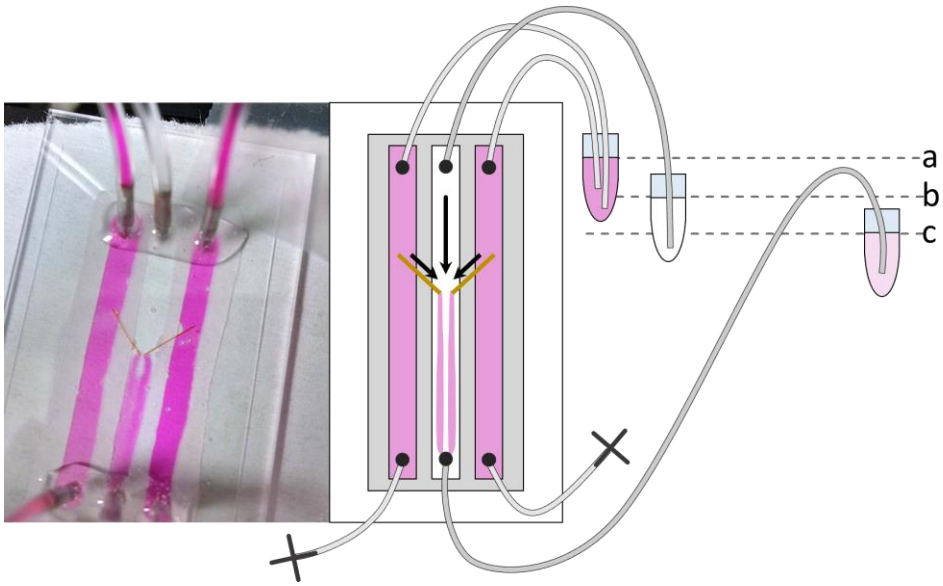

Figure 3.11 – Gravity-Controlled Flow Cell Operation
The side channels of a flow cell (left) were filled with Rhodamine dye to visualize the flow of reagent through the channel capillaries. The region near the capillary exits displays clear boundaries between the flows with no mixing. To the right is a diagram illustrating gravity-feed flow cell control. The height differential between the central channel inlet reservoir (b) and outlet reservoir (c) controls the flow rate in the main channel. The reservoir level for the side channel inlets (a) should be slightly higher than (b) to direct flow into the central channel at a moderate rate.

Once the flows are properly established a dumbbell tether can be formed. With the traps at maximum separation in the sample plane, an anti-dig bead pre-incubated with DNA is first caught in the upper trap, and then a streptavidin bead is caught in t he lower trap (figure 3.12). This configuration ensures that the DNA on the anti-dig bead is flow-extended towards the second bead. The traps are then moved close together to bring the free DNA end containing a biotin label near the streptavidin bead, and then drawn slowly apart. This process may be repeated several times until a signature force rise is observed, indicating the formation of a tether.

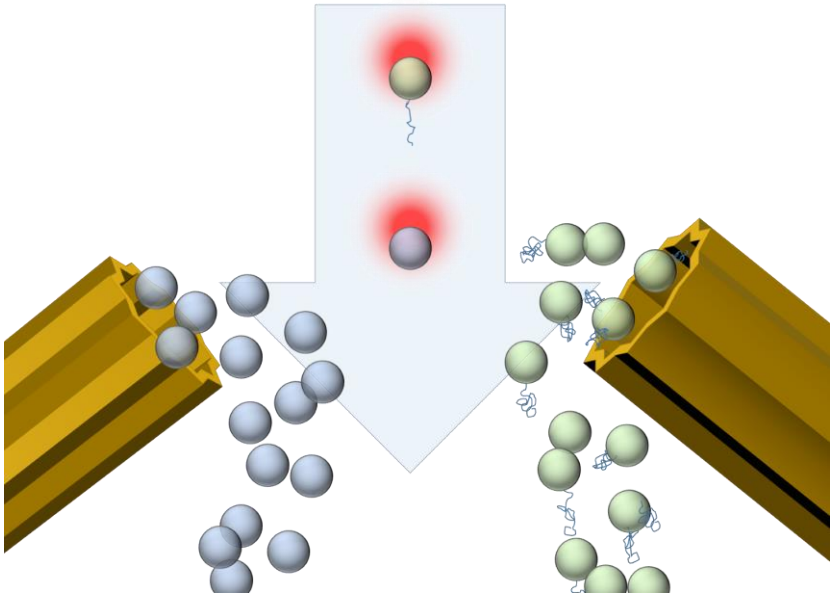

Figure 3.12 – Dumbbell Tether Formation
An anti-dig bead with attached DNA (green) in first caught in the upper trap, then a streptavidin bead (blue) is caught in the lower trap. This configuration ensures that the DNA is flow-extended downwards towards the streptavidin bead. The traps are then moved close together, then slowly apart. If a tether has formed, the detected force in the traps will rise as the tether is extended.

Labeling Dumbbell Tethers with Quantum Dots

For a template with a single quantum dot (QD) binding site, e.g. a single biotin label for a streptavidin-coated QD, the template DNA can be pre-incubated with a large excess of quantum dots before combining with beads as in the protocol in Table 2. The remaining process for flow cell operation and tether formation is unchanged. A large excess of quantum dots is necessary to prevent cross-linking between DNA strands, since the QD coating process attaches multiple streptavidin molecules to each QD, and each streptavidin additionally has multiple binding sites for biotin molecules.

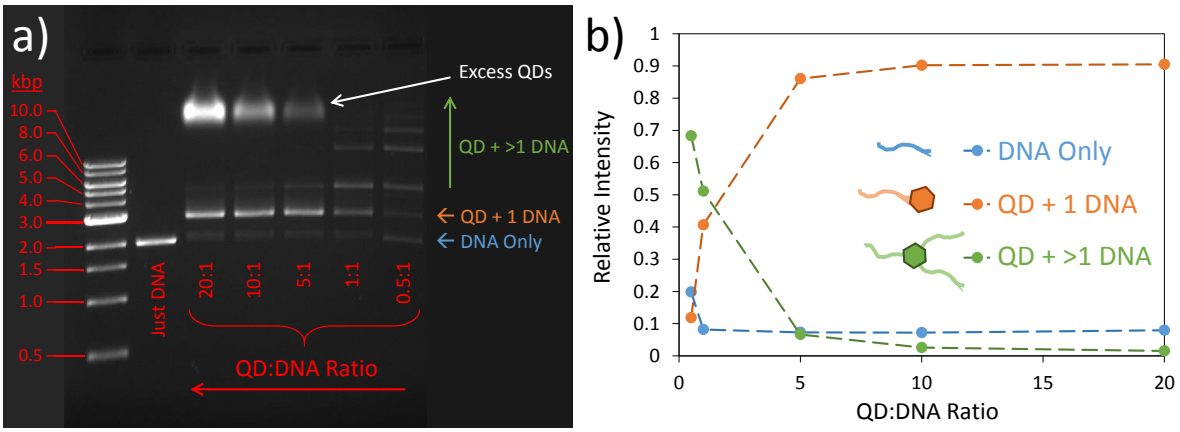

Figure 3.13 – Quantum Dot Binding Gel Assays Labeling Stoichiometry
a) A 2 kbp DNA template with one biotin label (blue) was incubated with several molar ratios of quantum dots (QDs). When a DNA binds a QD its gel mobility is reduced due to the QDs low intrinsic charge, shifting the band upwards (orange). Additional DNAs bound to the QD further reduce gel mobility (green). **b)** The intensities of the gel bands relative to their lane's total intensity are plotted as a function of QD:DNA ratio. The intensity in all DNA bands higher than the QD + 1 DNA band were summed. QD titration shows the expected behavior, reducing the population of multi-DNA-QD complexes, and increasing the relative proportion of the singly-bound species.

The appropriate incubation ratio to prevent crosslinking without wasting reagents can be assayed by gel electrophoresis (figure 3.13a). Though very small, quantum dots have poor electrophoretic mobility due to their low intrinsic charge [Zhang et al. 2012], thus their binding to DNA can introduce a significant gel shift. In figure 3.13, we incubated a 2 kbp DNA template containing one biotin label with varying ratios of streptavidin-coated quantum dots, from a 0.5:1 QD:DNA molar ratio, to a 20:1 excess of QDs. Multiple bands above the 2 kbp DNA-only lane (blue) result when one (orange) or more (green) DNAs are bound by each quantum dot.

The gel shift of the resulting QD-DNA complex is dependent on the DNA template length. For small DNA fragments, each additional DNA bound to a QD shifts the corresponding band lower on the gel. The mobility increase of the complex

due to the DNA's charged backbone outweighs the mobility decrease due to the DNA's size. For longer templates, the size of the DNA dominates the gel behavior of the QD-DNA complex, and each additional bound DNA slows the migration of the complex through the gel. This latter situation represents the behavior seen in figure 3.6, as can be deduced from the effects of QD titration shown in figure 3.13b. As the molar ratio of quantum dots to DNA is increased, so should the population of singly-bound DNAs (orange), along with a corresponding decrease in the bands representing multi-DNA-QD complexes (green). This allows us to assign the orange band to the singly-bound complex[3], and also to determine a good QD:DNA incubation ratio to minimize crosslinking. In this case, this can be achieved with a quantum dot excess of 10:1. The optimum incubation ratio is template dependent, however. Long templates favor singly-bound DNA:QD complexes due to charge screening of the entropically-coiled DNA molecule, which shields the quantum dot from binding additional DNAs and allows for optimum binding conditions at lower QD:DNA ratios (data not shown).

For templates containing multiple biotin tags, the situation becomes more complex. Rather than crosslinking between multiple DNA molecules, the quantum dots in this case will rapidly crosslink a single DNA to itself due to the proximity of

[3] Though we did not attempt it, a gel purification may also allow for a clean sample of singly-labeled DNAs and remove excess QDs from the solution. It needs to be verified that the presence of the QD does not affect the gel purification process, however.

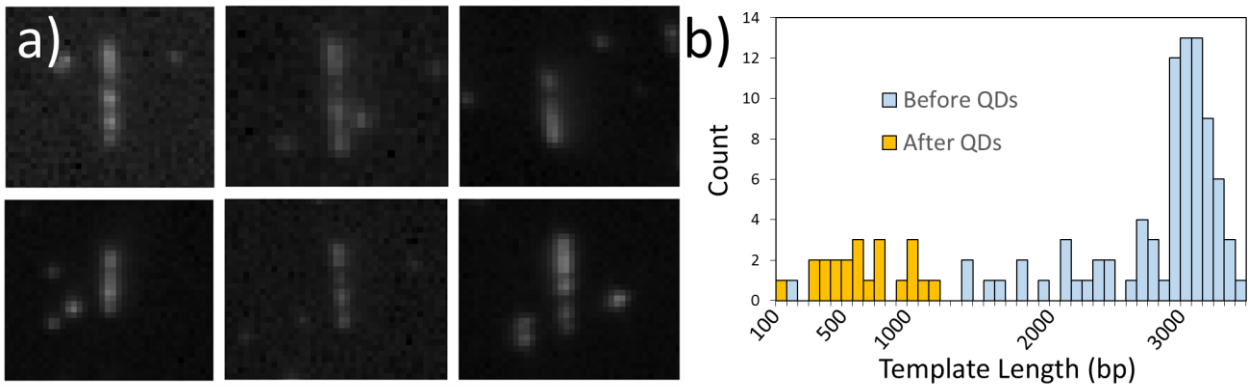

Figure 3.14 – Quantum Dot Labeling in Multiply-Labeled Templates
a) Our biotinylated 13.7 kbp DNA was flow-extended and fixed to a microscope cover slide and then incubated with streptavidin quantum dots, illustrating successful incorporation and labeling of multiple biotin binding sites. **b)** In a surface-tethered chamber using a biotinylated 3.2 kp DNA template, tether length was assayed via tethered particle motion (TPM) before (blue) and after (yellow) flowing in streptavidin quantum dots, and the results are shown by histogram. Initially at the expected length, the histogram distribution of tether lengths is dramatically shortened after flowing in quantum dots, illustrating crosslinking within each DNA strand due to multiple biotin binding sites on each quantum dot.

multiple biotin labels along the DNA template (figure 3.14b). Although this could hypothetically be remedied with a large enough excess of quantum dots, in practice this becomes difficult and expensive. Alternatively, the templates can be labeled while under force to prevent crosslinking, as shown in figure 3.14a in which tethers were first flow-extended and then fixed to a coverslip surface before introducing quantum dots.

When working with dumbbell tethers, labeling under force can be accomplished by introducing a fourth flow cell channel for the quantum dots, connected to the central channel by a third capillary. However, with unidirectional flow in the central channel and three reagent streams that need to be accessed sequentially, there is

topologically no capillary configuration that enables one to reach the third reagent stream without crossing through the second reagent stream. The quantum dot stream must be accessed after the tether is formed, which dictates we visit this stream last, however crossing through a bead stream destroys the tether.

Our solution to this problem was to remove the topological constraint imposed in the central channel by a unidirectional flow. Our design for a bi-directional flow cell for dumbbell labeling is shown in figure 3.15a. A central inlet and a pair of outlets on either end of the channel changes the flow symmetry and allows unencumbered access to each reagent stream. By offsetting the central inlet and connecting it with a lane at 90º to the main channel, we may also afforded the option to perform experiments under different flow conditions, either parallel or perpendicular to the tether axis. In a standard flow cell, a flow perpendicular to the tether is not possible because the flow must point along the tether axis to flow-extend the DNA for tether formation. Figures 3.15b and 3.15c show two different implementations of the concept, both with and without an extended side channel. The flow cell in 3.1c uses a nanofabricated silicon sample in place of a glass slide, demonstrating that flow cell construction is fully compatible with such substrates. With these bi-directional flow cells, a tether can be formed as usual, and then brought into a stream of quantum dots while the tether is extended under force in order to generate a dumbbell tether with multiple, direct quantum dot labels. Successful labeling with multiple quantum dots is

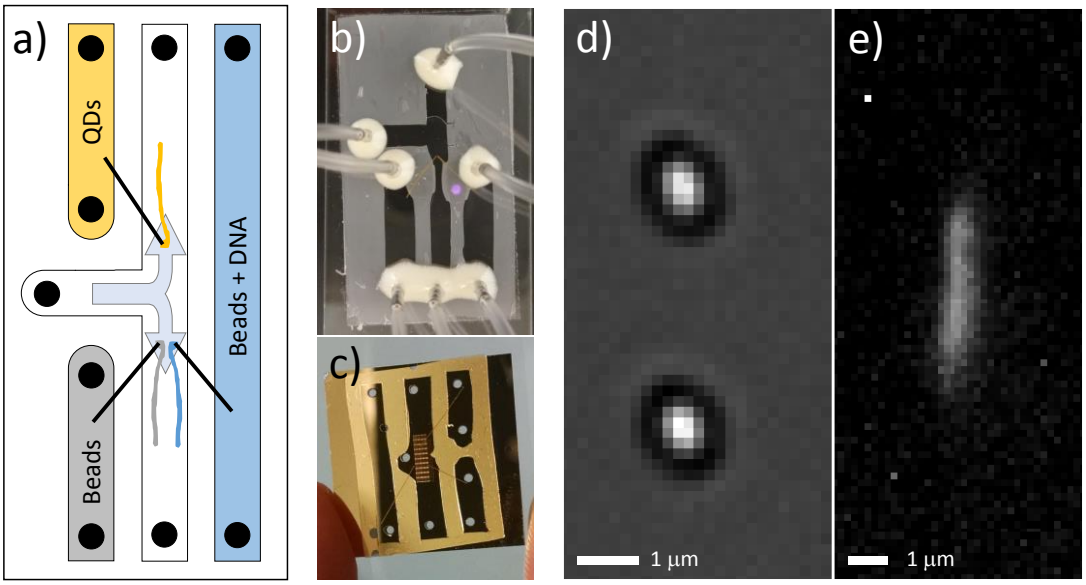

Figure 3.15 – Bi-Directional Flow Cell for Multiply-Labeled Dumbbells
a) The bi-directional flow cell pairs a central inlet with two outlets on either end of the central channel, enabling unencumbered access to three reagents streams for labeling tethers under force. **b)**, **c)** Two implementations of the concept, on glass (b), and on a nanofabricated silicon wafer (c). **d)** A brightfield image of a dumbbell tether after labeling with quantum dots. **e)** A fluorescence image of (d) showing multiple quantum dot labels along the template.

shown in figures 3.15d (a brightfield image of the trapped beads on either end of a 13.7 kbp DNA tether) and 3.15e (a fluorescence image showing QD emission along the DNA tether).

4. Instrument Implementation

This chapter describes aspects of realizing data from our optical trapping instrument. We begin by detailing the necessary calibrations for trap power and trap stiffness, which allow us to translate raw measurement signals into physical parameters. We then present a method for image-based particle tracking that is free of bias, enabling us to resolve sub-nanometer displacements of an optically-trapped bead. We characterize noise and drift in our detection system via power spectral analysis and Allan variance. We include the first temperature measurements in an optical trap near a gold surface, then conclude by showing DNA stretching and unzipping traces obtained by our instrument, with excellent agreement to theory.

4.1. Trap Power Calibrations

The goal of our power calibration is to determine the relationship between the amplitude of the AOD RF driving signal, which controls the fraction of our laser's output power that is sent to the objective, and the resulting trapping power acting in the microscope sample plane. The most accurate way to measure optical power in the sample plane is with a pair of identical objectives set up in a trapping configuration, allowing the empirical determination of scattering and reflection losses through the

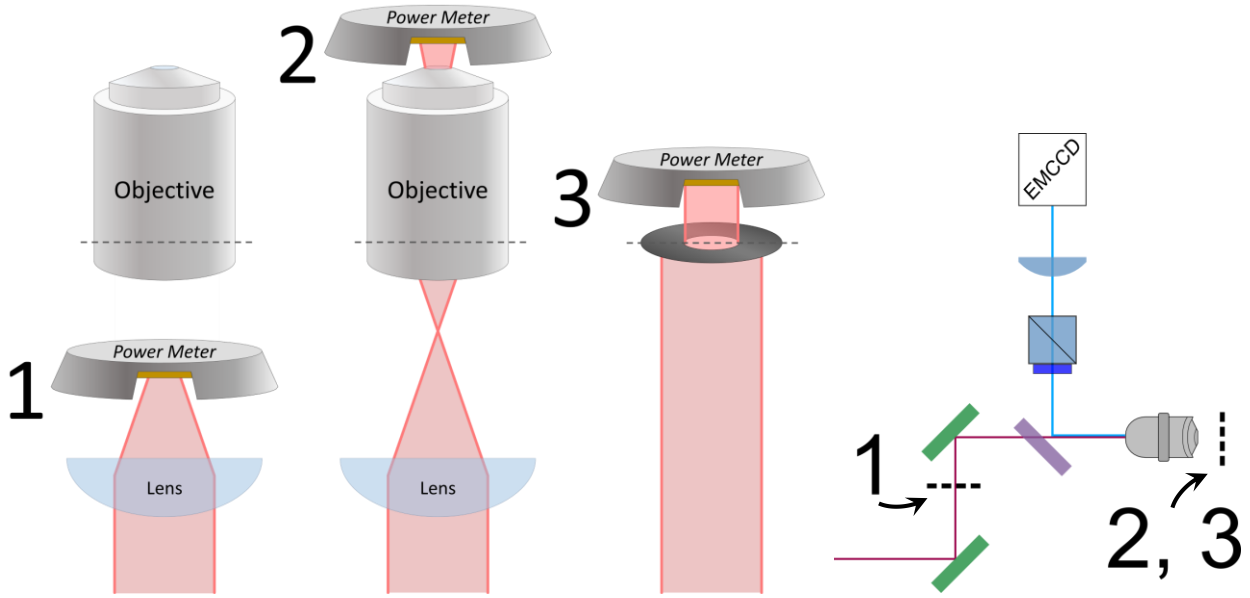

Figure 4.1 – Estimating Power Loss through the Objective: Configuration
Laser power is measured by a power meter as a function of AOD driving amplitude at three different locations. Position 1 gives the power incident at the objective back aperture. Position 2 relative to position 1 gives the power loss due to objective attenuation not factoring in clipping at the objective back aperture. In position 3, the objective is replaced with an iris diaphragm set to the back aperture diameter. The measurement at position 3 relative to position 1 gives the power loss due to clipping at the objective back focal plane. Combining the effects of objective loss and clipping gives the total attenuation of the trapping power incident at the objective back focal plane. The inset on the right shows the locations of the measurement positions with respect to the instrument layout in figure 2.1.

objective system by comparing the power sent into the trapping objective to the power exiting the collecting objective. We did not have access to a matched objective, however, and neither could we directly measure the trapping laser power at the objective focus, as the beam is too divergent through the objective focus for the aperture of our power meter. We thus implemented a sequence of measurements that can accurately estimate the amount of trapping power in the sample plane[4].

[4] Note that all measurements in this chapter were obtained with the AOD operating at its central frequency, and feedback stabilizations turned off.

Figure 4.1 shows the measurement sequence and configurations. A power meter (Newport 818T-10) was placed between the two periscope mirrors, which was the closest we could position the meter to the back of the objective (position 1), and a temporary focusing lens was inserted between the final PBSC and the periscope in order to shrink the trapping laser profile so that it would fit on the power meter's sensor. The relationship between AOD driving amplitude and input power to the back of the objective was then measured. In position 2, the power meter was placed immediately after the objective such that the trapping laser, focused near but not at the objective back focal plane by the temporary lens, was fully contained on the power meter sensor surface. Without the temporary focusing lens, the beam would be too divergent to fit fully on the power meter's sensor, because the power meter's aperture is too small to permit the nose of the objective to get close to the sensor surface. The power measurements as a function of AOD driving amplitude were repeated at position 2, and from this, the transmission ratio of the objective was determined to be about 69%.

In addition to transmission losses caused by the objective's lenses, attenuation of the input beam will also occur due to the objective's back aperture, which the laser slightly overfills. In position 3, we replaced the objective lens with an iris diaphragm that was carefully measured and set to the diameter of the objective back aperture. We again measured the power as a function of AOD amplitude, and determined the back-

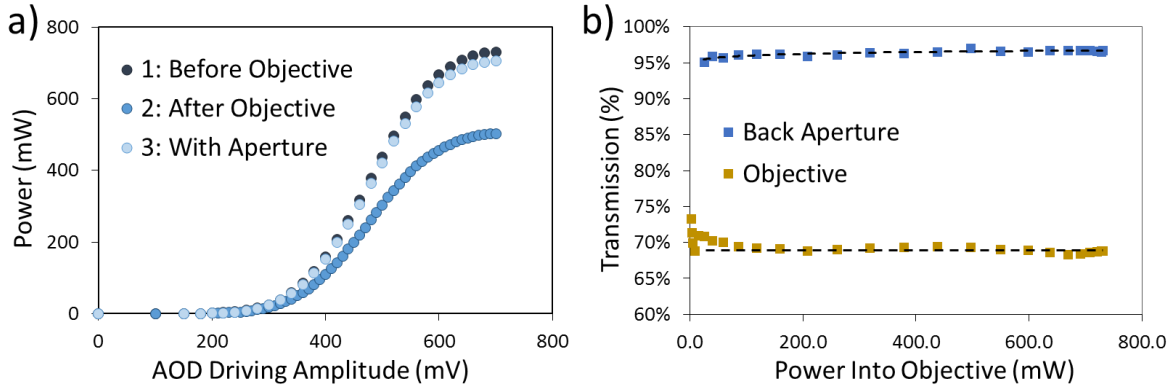

Figure 4.2 – Estimating Power Loss through the Objective: Measurement
a) Measured power versus AOD driving amplitude (as mV into the RF synthesizer) is plotted for the three detector positions shown in figure 4.1. **b)** The ratio of curve 2 to 1 gives the objective lens attenuation, and the ratio of curve 3 to 1 gives the back aperture attenuation. These ratios are plotted as a function of power into the objective. Objective loss is estimated at 69% across all input powers, and aperture loss was fit with the function $y = 3.74x10^{-3}ln(x) + 9.42x10^{-1}$. The product of these two losses gives the total attenuation of trapping laser power by the objective.

aperture transmission as a function of input power from its ratio to measurement 1. This relationship was well-fit by the expression $y = 3.74x10^{-3}ln(x) + 9.42x10^{-1}$. Figure 4.2a shows the power relationships obtained at all three positions, and figure 4.2b shows the relevant ratios between measurements. Multiplying the attenuation due to the objective's transmission properties and the objective's back aperture size gives the overall attenuation between the sample plane power and the objective input power as measured between the periscope mirrors:

$$P_{Sample\ Plane} = 2.58x10^{-3}\ln\left(P_{Obj.Input}\right) + 9.42x10^{-1}$$

The objective losses thus characterized for a given input beam size, future calibrations of trapping power can be acquired by performing a single measurement series of laser

power versus AOD driving amplitude with the Newport detector at position 1, and applying the above attenuation function for the objective.

Our next task was to calibrate the high-speed InGaAs photodiode (HSPD) in order to enable live, in-setup measurements of the trapping power in the sample plane. We use a pellicle beam splitter as described in section 2.1 to direct a small fraction of the trapping laser onto the HSPD surface, which is synchronized to the trap modulation in order to make differential power measurements on each trap, as described in section 2.4. In figure 4.3 we show a diagram of the measurement configuration and predicted photodiode (HSPD) and power meter (Newport) responses for both CW and modulated traps. We expect the HSPD power reading of a given trap to be identical for a CW trap and a modulated trap of the same AOD driving amplitude. The Newport power meter, however, has a bandwidth of less than 1 Hz, and so a power measurement in the case of a modulated trap will yield the time-averaged power of both traps. In order to measure the average power of one modulated trap in the sample plane, we set trap 2 to 0 mW and varied the AOD driving amplitude for trap 1. The Newport meter then gives the time-averaged power of trap 1 in the sample plane after applying the attenuation function described earlier, thus allowing us to determine HSPD voltage as a function of power in the sample plane for a modulated trap.

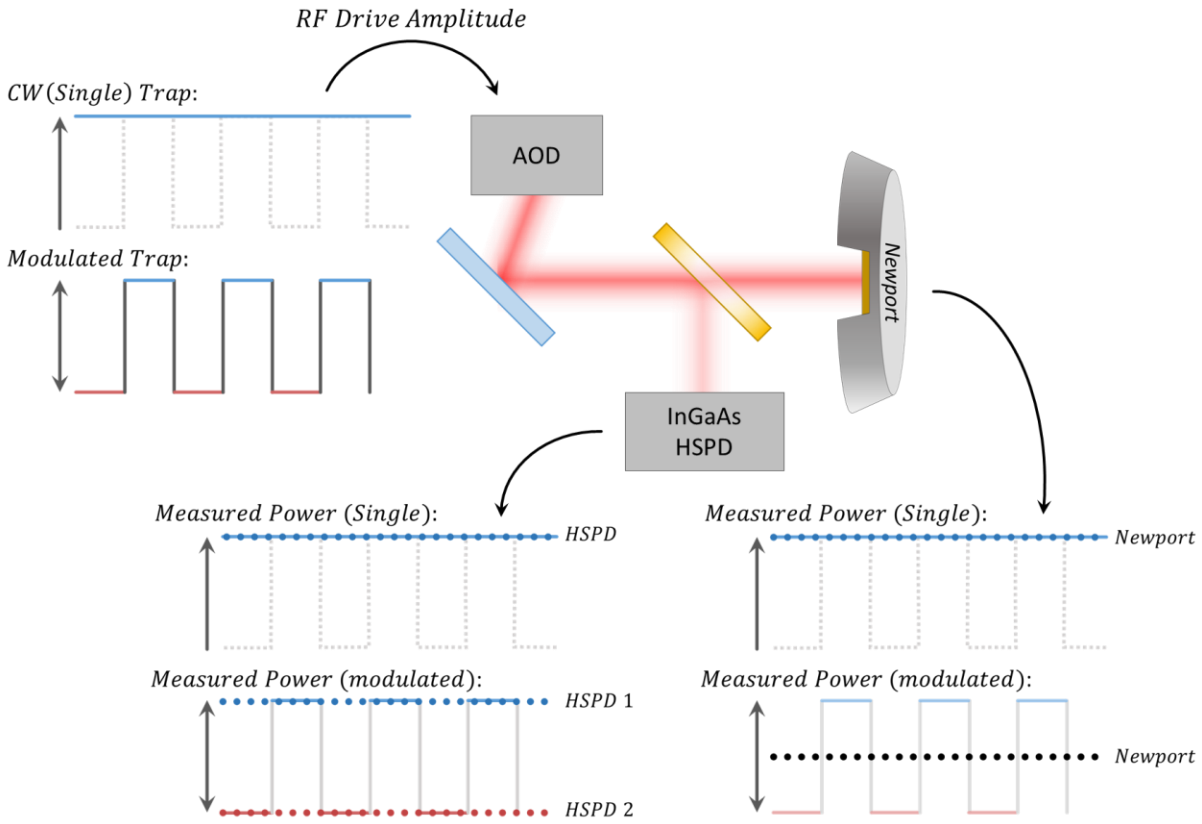

Figure 4.3 – Measuring Power in a Modulated Trap
To calibrate our InGaAs high speed photodiode (HSPD) to measure trapping power in the sample plane, we use a pellicle beam splitter (gold) to sample a fraction of the beam. The remaining power is incident on the Newport power meter location between the periscope mirrors (position 1, figure 4.1). We can then calibrate AOD driving amplitude to an InGaAs voltage reading, and to a power in the sample plane as measured by the Newport meter with the attenuation function described earlier. To measure power in a modulated trap, we set trap 2 to 0 mW and varied the power in trap 1, in which case the Newport meter gives the time-averaged trap power of trap 1 in the sample plane.

The HSPD voltage as a function of trap power in the sample plane for a CW single trap, and for a modulated trap is shown in figure 4.4a. Surprisingly, the measurements were not identical. As laser power is increased, the HSPD measures a higher voltage for a modulated trap than for a CW trap of the same power, resulting in a nonzero slope for the ratio of the modulated trap power to the CW trap power

One potential explanation is the temperature-dependent responsivity inherent to photodiodes, as we expect that laser power incident on the sensor surface will increase its temperature. Modulating the traps from zero to a target value reduces the time-averaged incident power on the photodiode, and so the modulated trap reading will occur at a lower temperature than for a CW trap at the same maximum power. For a lower temperature to produce a higher photodiode current for an equivalent amount of incident optical power, the temperature coefficient modulating the responsivity curve would need to be negative. Indeed, for InGaAs photodiodes at 1064 nm, the temperature coefficient is around -0.1% [Stock and Heine 2000].

The Newport power meter, on the other hand, is a thermopile-type detector, and so the temperature-dependence of its electrical response is precisely what yields an accurate power reading. The trap power in the sample plane measured by the Newport power meter as a function of AOD driving amplitude, again for a CW trap and for a modulated trap, is shown in figure 4.4b[5]. If the effects we measured in figure 4.4a were solely due to the thermal coefficient of the HSPD, we would expect the ratio between the CW and modulated trap as measured by the Newport meter to be constant with trap power (and equal to the duty cycle). As seen in figure 4.4b, this is not the case.

[5] Note that between the measurements in figures 4.2a and 4.3a, we increased the power from our fiber laser from 35% to 50.6%

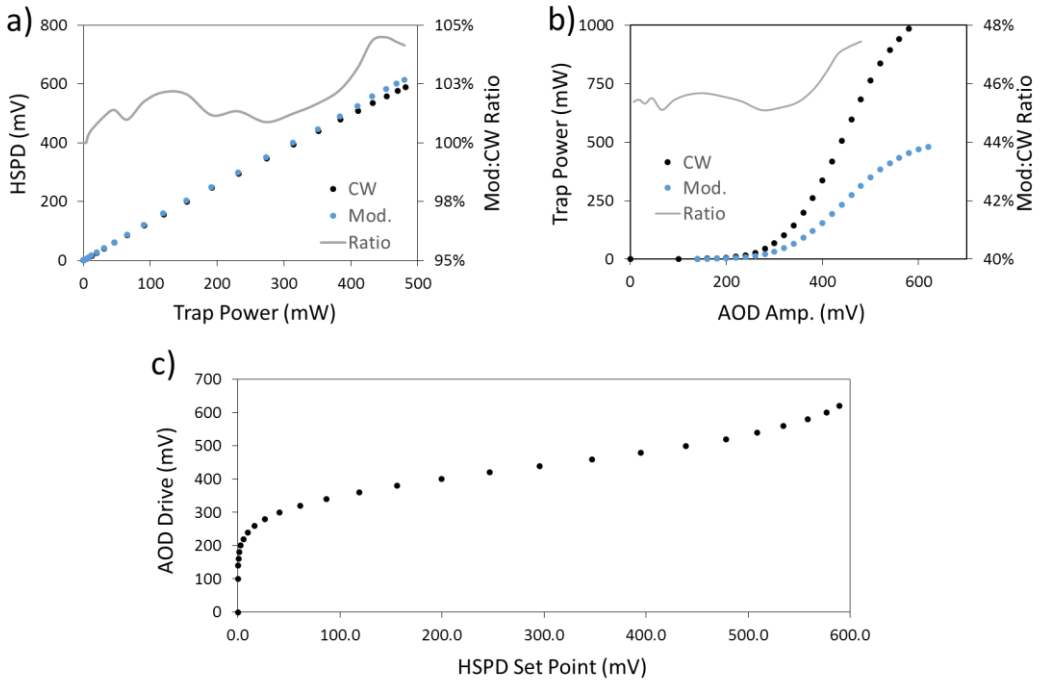

Figure 4.4 – High Speed Photodiode Calibration
a) HSPD reading as a function of sampled plane trapping power for a single (CW) and modulated (mod.) trap. The sample plane power was calculated for the Newport power measurement (b) at the same AOD driving power (figure 4.3). Though we expect identical readings for the CW and modulated traps, we find that the modulated traps give a higher reading at high modulation depths. **b)** Trapping power in the sample plane versus AOD driving amplitude (as mV into the RF synthesizer) for a CW and modulated trap. The ratio of the two gives the duty cycle as 45%, but reflects a similar rise with trap power as in (a). **c)** For PID control of trap power, a HSPD set point is first calculated from a target trapping power from (a), and then the PD set point is converted to an AOD driving power set point from (b).

The fact that two power meters using very different physical mechanisms show the same effect is strong evidence that the results are indeed reflective of the physical trap power during modulation, and not a measurement artifact. Regardless, the effect appears only when modulation depth is very large (reminiscent of an overdrive, perhaps), and our modulation depth during experiments, with approximately equal powers in both traps, is always very shallow. Therefore, we assume the true duty cycle during trap modulation is always fixed at 45% (the value measured for small

modulation depths), and use only the CW HSPD calibrations for our power set points, since our actual power modulation approaches CW conditions for equal trapping powers.

From these measurements we can determine the power present in the sample plane at any given time from the measured HSPD voltage, and also determine the appropriate AOD driving amplitude to achieve a target power in the sample plane. All of these calculations are performed on the FPGA. We use the measured HSPD voltage as the process variable for PID control of the AOD driving amplitude, stabilizing trap power in the sample plane to a user-determined set point (see section 2.4). The photodiode set point for a requested trapping power is determined from the linear fit of the data in figure 4.4a, and then this is converted into an AOD driving amplitude with the data in figure 4.4c as a LUT.

4.2. Trap Stiffness Calibrations

We have previously introduced common methods for quantifying the trap stiffness k of an optical trap, which is prerequisite to obtaining a force value F_{Trap} from a displacement measurement x via the harmonic relationship

$$F_{Trap} = -kx.$$

Although the equipartition theorem and power spectral density (PSD) methods are fast and accurate, they require a large measurement bandwidth to capture the full spectrum of trapped bead motion. A slow acquisition rate acts as a low-pass filter, and the loss of high-frequency information on the trapped particle's position results in an underestimation of trap stiffness in the case of the equipartition method, and can either underestimate or overestimate the Lorentzian in the case of the PSD method, depending on the relationship between the sampling frequency and the corner frequency [van der Horst and Forde 2010].

Van der Horst and Forde accounted for the blur and aliasing that occurs in image acquisition when the Nyquist frequency f_{Nyq} is below the power spectrum corner frequency, in order to obtain a corrected Lorentzian from the measured spectrum. They validated this method against measurements taken from a quadrant photodiode and showed accurate results for f_c up to 3 times f_{Nyq}, however as acquisition rates fall to the sub-kHz range, the viability of spectral stiffness measurements diminishes rapidly. When image acquisition rates are well-below the 1 kHz threshold, the drag force method is the preferred option. A trap stiffness measurement made via drag force analysis is, relative to other methods, more time consuming and labor-intensive, but produces accurate results.

The drag force method makes use of the known frictional force imparted to a low Reynold's number, spherical object by a laminar flow, which is given by Stokes' law as

$$F_d = 6\pi\eta r v$$

where η is the viscosity of the surrounding medium, r is the radius of the particle, and v is the relative velocity of the particle to the medium. Accordingly, if we measure the displacements bestowed to a bead by the drag force at a series of velocities, the slope of the linear relationship between the known forces versus the measured displacements yields the trap stiffness [Malagnino et al. 2002].

Though theoretically simple, the implementation of this technique presents some challenges. If we consider our typical bead size of 500 nm, generating a 1-pN force[6] requires a velocity of almost 250 μm/s. A piezo stage is the standard choice for moving the sample relative to the trap to produce this velocity, and the precision stages found on an optical trapping instrument have ranges on the order of 100 μm. Given that we are already under the constraint of low image sampling rate, it can be difficult to acquire enough data points to make a given measurement before the stage exhausts its linear range. Additionally, because image acquisition rates and image noise are inversely coupled, increasing framerates will not necessarily improve performance,

[6] Using the dynamic viscosity of water $\eta = 8.9\text{x}10^{-4}$ Pa·s, and $r = 2.5\text{x}10^{-7}$ m.

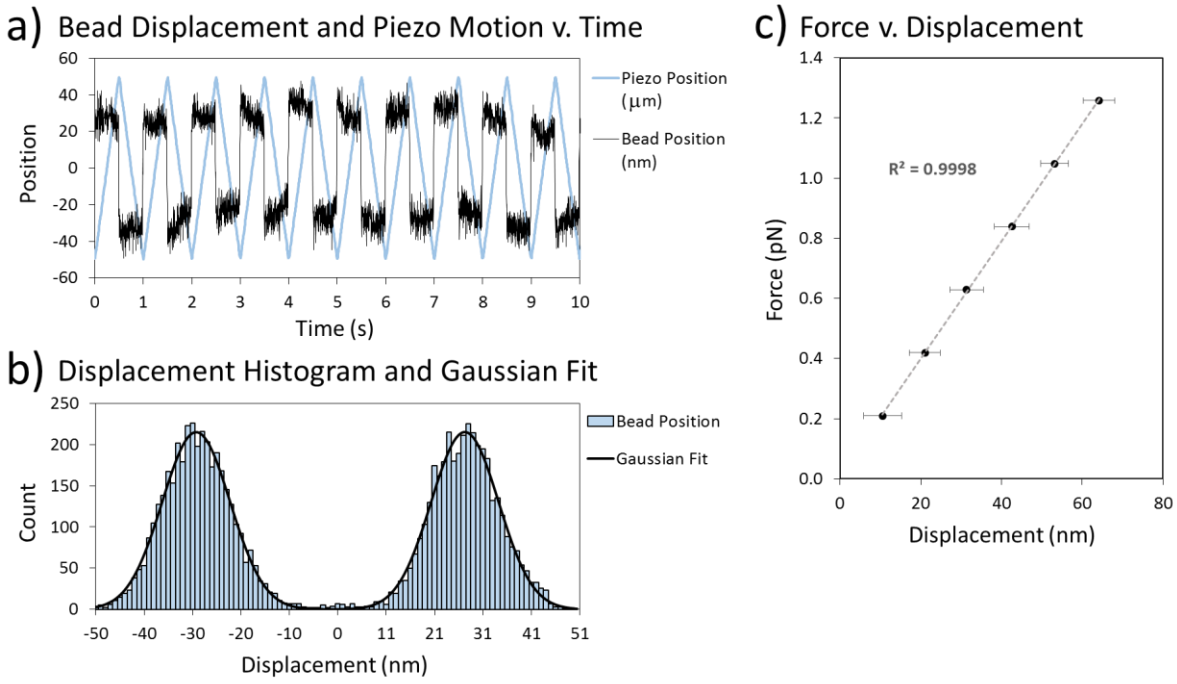

Figure 4.5 – Drag Force Stiffness Calibrations Part I: Method
a) Bead displacement (black) and piezo position (blue) versus time from a representative measurement. **b)** The bead displacement data from (a) plotted as a histogram and fit with two Gaussian curves. **c)** Calculated forces are plotted versus the displacements obtained from the Gaussian fits for several different velocities. The data shows an excellent degree of linearity (R = 0.9998). The error bars represent the standard error of the fit.

as a concurrent increase in noise would require we average over a greater number of samples to yield the same level of precision.

We overcame these limitations by modulating piezo position as a triangle wave and analyzing the data by histogram. The bead in this configuration oscillates as a square wave between a positive and negative displacement value about the trap center as the stage is moved in either direction (figure 4.5a). The histogram data (figure 4.5b) is fit with a pair of Gaussians whose peaks represent the average displacement positions over many piezo cycles, allowing a robust and drift-resistant data set to be

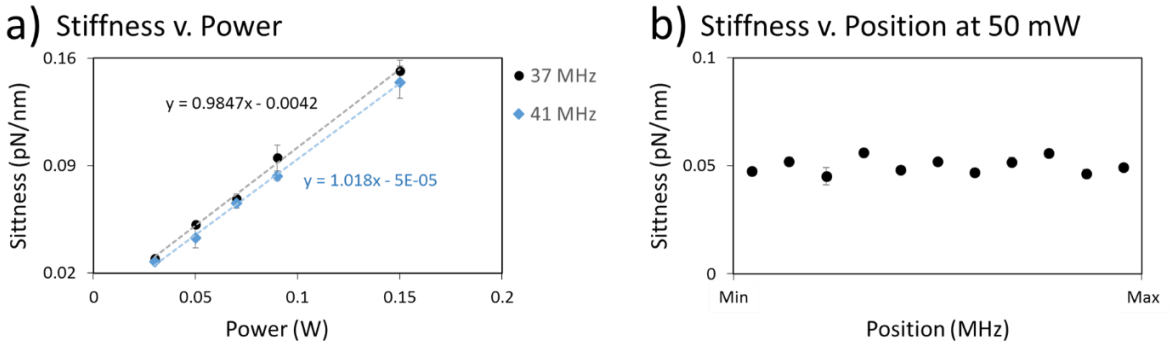

Figure 4.6 - Drag Force Stiffness Calibrations Part II: Results
a) Stiffness as a function of power is shown at two different AOD frequencies, and averages to 1.0 ± 0.07 pN/nm·W over all trap positions. **b)** Trap stiffness at 50 mW trapping power is shown as a function of trap position. The trap position ranges from 25 to 45 MHz, corresponding to 18.2 μm of travel in the sample plane.

collected over time even when the piezo can only be moved in one direction for a fraction of a second. In addition to obtaining the bead displacement for a given piezo velocity, an examination of the widths and symmetry of the two peaks provides insight into the symmetry of the traps along the movement axis. Indeed, the presence of axial asymmetry in our initial stiffness measurements alerted us to a problem with our laser alignment. Once rectified, our stiffness measurements yielded the excellent degree of symmetry presented in figure 4.5b.

In figure 4.5c we show an example of the linear relationship between force and measured displacement, which yields one stiffness data point from the slope. The accuracy of this technique is evidenced by the quality of the linear relationship as measured by R^2. The error bars here represent the standard error of the fit. We repeated this process at a variety of different trapping laser powers and trap positions as modulated by the AOD, and the results are shown in figures 4.6a and 4.6b,

respectively. Our traps have a stiffness of 1.00 ± 0.07 pN/nm·W, where Watts here indicates the time-averaged power per modulated or CW trap in the sample plane. The flat profile of our trapping stiffness across the AOD's driving range indicates that the AOD is well-mapped to the objective. Note that power feedback stabilization was turned on for this set of data to ensure the traps received constant power across the AOD's driving range. Our measured trap stiffness is well in line with other optical tweezers in our lab, which have stiffnesses ranging from 0.97 pN/nm·W to 1.29 pN/nm·W. Elsewhere, optical tweezers may range in stiffness from around 0.5 pN/nm·W [Svoboda et al. 1993] to upwards of 4 pN/nm·W using reporter particles custom fabricated from more exotic materials [Jannasch et al. 2012].

The validity of the stiffness parameters we obtained may be assumed indirectly by the accuracy of the force measurements they yield against a known theoretical force, and this is examined in section 4.5. Though the results of these calibrations were quite accurate, the method lacks the ability for facile on-the-fly stiffness measurements, which can (quickly) yield valuable information such as bead heterogeneity and instrument changes over time. We anticipate the implementation of a high-speed camera system on this instrument for power spectral density stiffness measurements in the near future.

4.3. Measuring Displacement: A Bias-Free Particle Tracking Method

An optical trapping instrument enables the measurement of forces and displacements on the piconewton and nanometer scales by measuring the spatial displacement in the sample plane of an optically-trapped particle relative to the trap's center. Thus the precision, accuracy, and speed with which a trapped particle's position can be determined are defining characteristics of an optical trap. An instrument that is capable of measuring nanometer displacements can potentially resolve events on a DNA template to within a few base pairs. This instrument employs image-based particle tracking to determine the displacements of trapped objects relative to their respective trap centers.

Image-based particle tracking (IBPT) is widely employed across diverse applications including machine vision and industrial inspection, particle image velocimetry for investigating flow fields, and in biological fields for tracking cells, fluorescent dyes attached to an object of interest, and optically or magnetically trapped particles attached to an object of interest. Commonly implemented tracking algorithms for micron-sized or smaller particles include centroid estimation, image cross-correlation analysis, and for sub-diffraction-limit particles, a direct fit to a 2D Gaussian model. Though common in magnetic tweezer instruments where the implementation of back focal plane interferometry is excluded, it is rarely seen in

optical trapping instruments due to a host of limitations that make BFPI a superior detection technique.

Image-based force detection for optical trapping presents several significant challenges compared to back focal plane interferometry. The most obvious concern is speed. The photodiodes used to measure the laser signal which informs on the position of the trapped bead in a BFPI setup can be operated at tens of kHz – much faster than the corner frequency of a trapped particle. A typical camera, meanwhile, might acquire frames at speeds around 50 to 100 Hz. A second concern is precision, which is limited by the combined sources of noise in an instrument. Though both BFPI and IBPT rely at their core on photodiode technology, there is a large discrepancy in the signal to noise ratio of their respective measurements. BFPI uses the majority of the trapping beam, ranging from tens to hundreds of mW, to illuminate what are essentially 4 large "pixels" of a quadrant photodiode. That signal produces a continuous photodiode current which may be sampled at very fast rates. Amplification circuitry is relatively simple, and there is no need to make an analog to digital conversion. In contrast, the light intensity illuminating a microscope sample is often much less than in a focused laser trap, and only the fraction of the light that interacts with the trapped particle is used for detection. Shot noise can be significant in many imaging applications, and noise is added by the pixel amplification, readout, and digitization processes. Unlike in BFPI, speed and noise are inversely coupled in

IBPT; as the exposure time is shortened to acquire frames at a higher rate, signal to noise ratio decreases proportionally.

Not only is the noise floor higher and the light being used to make a measurement dimmer in the case of a camera detection scheme versus a BFPI configuration, the absolute magnitude of the signal that must be measured is much smaller in the case of IBPT as well. As an interferometric technique, small displacements of the bead in the sample plane are amplified in the interference pattern at the back focal plane of the objective, and these small displacements are measured as a differential signal at the quadrant photodiode. Furthermore, the choice of the back focal plane as the measurement plane greatly reduces the effects of instrument drift, since only relative changes between the bead and trapping laser appear as a signal. Angstrom-level displacements are well-within the capabilities of most BFPI systems if other sources of environmental noise can be suppressed. Meanwhile, for IBPT, measuring a displacement of one nanometer requires measuring a change in position of an image to within around $1/100^{th}$ of a pixel[7]. This technique is highly susceptible to drift, both of the trapping optics and of the imaging optics, and limited fundamentally by signal to noise ratio and the speed of image acquisition relative to the drift over the time-scales of interest. However, although IBPT in optical trapping

[7] For a magnification of 100x and a pixel size of 10 μm (pixel sizes in scientific cameras typically range from 5 to 15 μm), a 1 nm displacement corresponds to 0.01 pixels.

presents a substantial SNR challenge, noise that is randomly distributed can be mitigated by a high acquisition rate and frame averaging. Systematic error may present a more serious problem.

In order to make an image-based determination of position to within less than $1/100^{th}$ of a pixel, another important (and often overlooked) limiting factor is pixel bias. Pixel bias is a type of systematic error that arises due to the discrete sampling of a continuous signal. When tracking a particle, this discretization acts to bias the resulting fit of the particle's position towards integer pixel values, a phenomenon known as "peak-locking."

We can see how pixel bias arises by examining the position tracking error that occurs when fitting a continuous function on a discretized sampling grid. A 1-D generalization of the problem is sufficient to display biasing behavior. Consider a single dimension, $I(x)$, of a two-dimensional continuous image $I(x, y)$ falling on a camera sensor. The effect of the camera sensor can be modeled by a transfer operator $\mathcal{H}$ which maps the continuous function $I(x)$ onto a discrete data vector $\bar{g}$:

$$\bar{g} = \mathcal{H}I(x)$$

When a curve is fit to a discrete array of points, it makes an implicit assumption of the transfer operator, namely that the value g_j of the data vector at pixel index j is

obtained by evaluating the continuous function at the point in the center of the pixel (Figure 4.7a):

$$g_j = \int_{-\infty}^{\infty} I(x)\,\delta(x - x_j)dx = I(x_j)$$

where δ is the Dirac δ-function. If the pixels on a camera which discretize the continuous image $I(x)$ worked according to such a transfer operator, a direct fit of $I(x)$ to the data vector $\bar{g}$ would result in zero bias error.

In fact, the pixels on a camera act to integrate the image function across the width of the pixel w using a rectangular transfer operator (Figure 4.7b):

$$g_j = \int_{x_j - w/2}^{x_j + w/2} I(x)\,dx$$

The difference between the rectangular transfer operation imparted by the camera sensor, and the delta function transfer operation assumed by a curve fit to an array of points, results in a systematic error in the fit (Figure 4.7c) that is periodic on the pixel grid. Note that in the case where the image function is linear across the pixel width, the delta function transfer operator and the rectangular transfer operator return the same value and the bias error imparted by the transfer operator is zero. Thus the faster an image function varies nonlinearly across the pixel width, the larger the

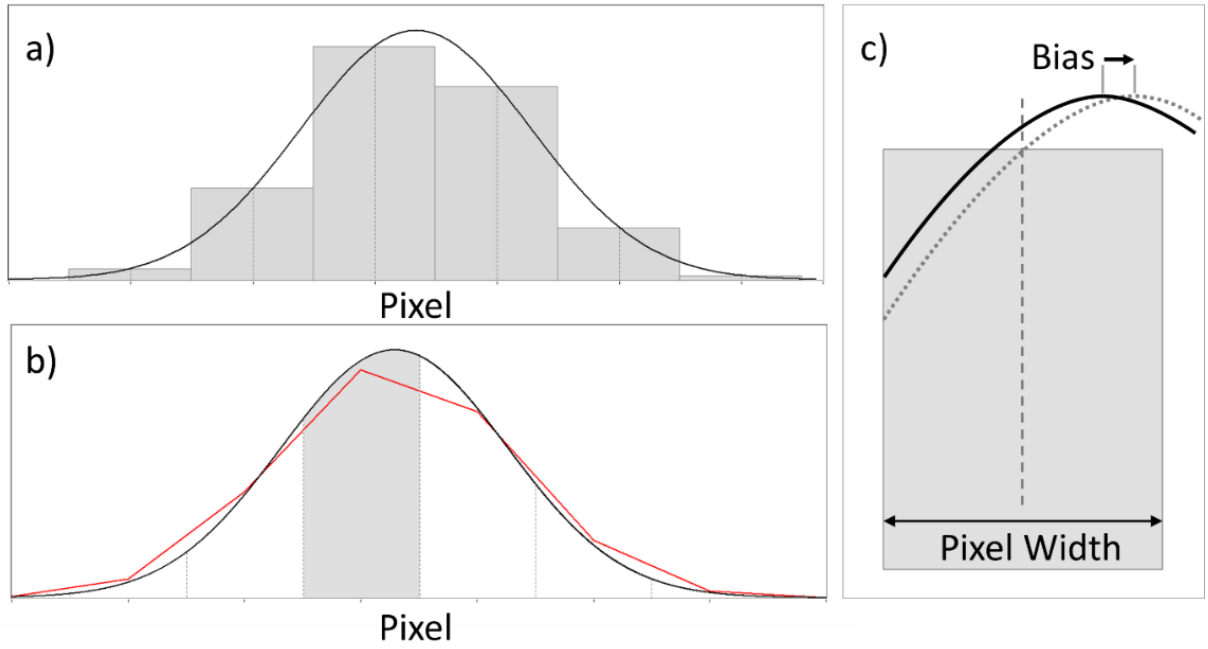

Figure 4.7 – Pixel Bias from Sampling a Continuous Function on a Discrete Grid
a) A continuous Gaussian image function in one dimension (black line) is discretized on a pixel grid. If the value each pixel assumes (grey bars) is equal to the value of the image function at the pixel's center, then a Gaussian fit to the discrete array recovers the original image function. **b)** If instead we integrate the continuous function across each pixel, as more closely represents the behavior of a camera, the resulting discretization (red line) will impart error based on the degree of nonlinearity of the image function across the pixel. **c)** A Gaussian fit performed through the discretization obtained via integration no longer recovers the initial image function. The error, known as pixel bias, is periodic on the pixel grid.

resulting bias error. This can be viewed as a restatement of the Nyquist Theorem, in that the higher the frequency components present in an image function, the higher the sampling rate must be in order for information to not be lost.

Although we have considered here the case for a direct fit of an image function, cross-correlation methods suffer as well when the discrete cross-correlation matrix is used to determine sub-pixel displacement. Most commonly, the adjacent points to either side of the cross-correlation matrix peak in x and in y are fit to a Gaussian

curve or a parabola, and this process is subject to the same discretization bias. Moreover, additional bias is introduced when discrepancies exist between the fit function and the actual image function.

We illustrate these effects through a series of simulations. We first examined only the effect of the image transfer operator error discussed above. We began with a continuous Gaussian in one dimension as our image model, and integrated this function across a pixel grid to simulate an image formed via a rectangular transfer operation. We then fit this simulated image with a Gaussian function identical to the one used to generate the discretized image, and examined the bias given by the difference in the peak location of the generated image function and the peak location of the best fit to the discretized image. The results are shown in figure 4.8a. In the case where a true Gaussian image is fit with a Gaussian model, the bias is only significant when the width of the Gaussian (defined here as the FWHM) drops below about 1.5 pixels. The bead images in our instrument, however, are not Gaussian, and are in fact well-described by a cardinal sine (sinc) function with an exponential decay. If we take this more realistic function as our 1D image model, the bias is impacted by the mismatch between the fit and image functions. For a FWHM of 2 pixels, the bias is an order of magnitude larger when fitting the more realistic image model with a Gaussian (figure 4.8b).

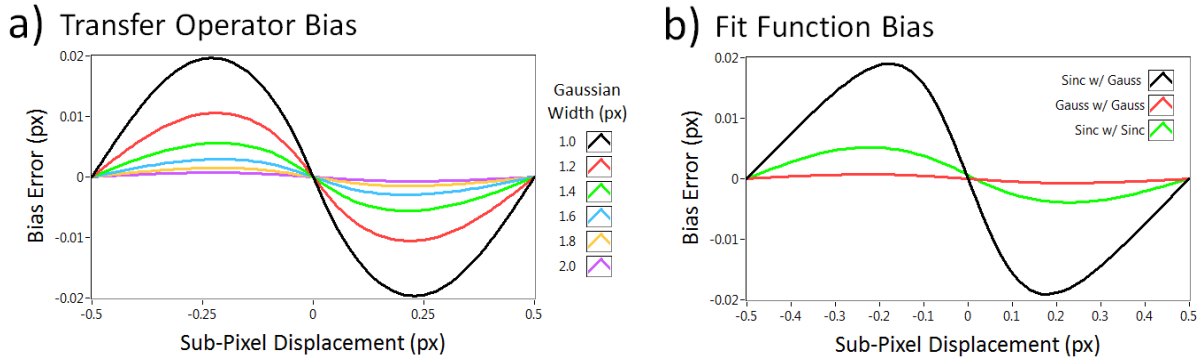

Figure 4.8 – Simulated Pixel Bias with a Rectangular Transfer Function
a) A continuous, 1D Gaussian image function was discretized on a pixel grid according to a rectangular transfer function that integrates the image intensity across the width of each pixel. When the discretized image is fit with the same Gaussian model used to generate the pixel array, bias results. Bias for various Gaussian FWHMs are shown. **b)** Bias error increases when the fit function does not match the image model function. Using a FWHM of 2 pixels, a Gaussian fit to a Gaussian image has negligible bias, but a Gaussian fit to a more realistic sinc function with decay has significant bias. Fitting the sinc image model with a sinc fit function improves performance.

We have seen that when the fitting model is an approximation of the true image function (rather than the identical function), bias is increased. This comes into play with real-world images, where an initial image function is convolved with the point-spread function of the optics in use, and initially symmetric objects may be distorted elliptically. Indeed, bias is strongly influenced by elliptical objects, particularly when their elliptical axis is not aligned with the axis of movement. We performed simulations to investigate the bias produced by various fit models when tracking a realistic, two-dimensional model image.

Our model image was generated by a 2D, asymmetric sinc function with rotation and exponential decay, where pixel values on a grid were assigned according to

$$P(x,y) = A\frac{sin(\mathcal{R})}{\mathcal{R}}e^{-\left(\frac{\mathcal{R}}{d}\right)^2} + B$$

where A is the peak amplitude, B is the background offset, d is a parameter that modulates the bounding decay rate, and $\mathcal{R}$ is the rotated radial distance from the center given by

$$\mathcal{R} = \sqrt{\left[\frac{(x-x_c)'}{w_x}\right]^2 + \left[\frac{(y-y_c)'}{w_y}\right]^2}$$

Here, x_c and y_c are the x and y (subpixel) positions of the function peak, w_x and w_y are parameters that modulate the x and y widths and the prime ($'$) on the center-shifted x and y coordinates indicates each has been acted on by a rotation matrix:

$$\begin{bmatrix}(x-x_c)'\\(y-y_c)'\end{bmatrix} = \begin{bmatrix}cos\theta & -sin\theta\\ sin\theta & cos\theta\end{bmatrix}\begin{bmatrix}(x-x_c)\\(y-y_c)\end{bmatrix}$$

Note that assigning pixel values this way assumes a delta-function transfer operator. The following simulations therefor neglect the contribution of bias from the integration action of a camera array, however we have shown that this source of bias is indeed negligible for objects sized ~2 pixels and larger, which are the exclusive subjects of our interest for the remainder of this section.

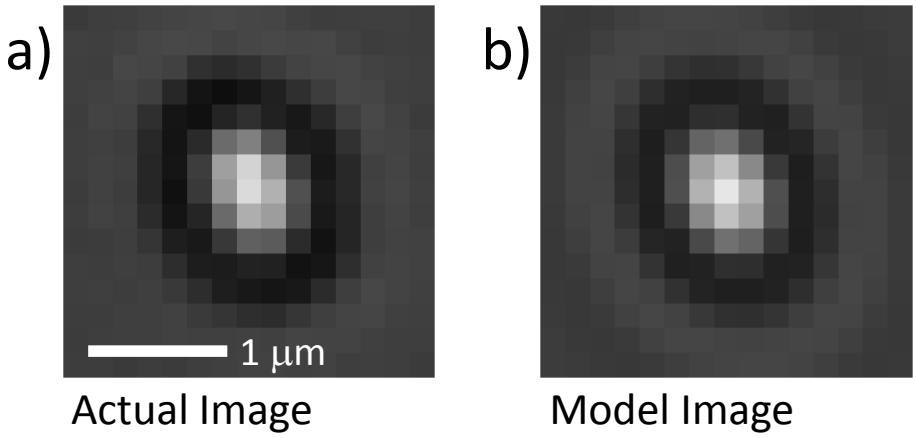

Figure 4.9 – Image Model for Simulating Polystyrene Beads
a) A real image of an optically-trapped, 500-nm polystyrene bead taken from our instrument. **b)** A simulated image using parameters obtained from fitting our real image data with our sinc function bead model.

Our image model was constructed to represent the bead images we obtain from our instrument. Figure 4.9 compares an actual image (a) of a trapped 500-nm polystyrene bead taken with our instrument, to a simulated image (b) generated by our model using the fit parameters described above. Thus generated, we used our image model to compare the accuracy of various tracking methods, including cross-correlation, direct fitting to a Gaussian model, and direct fitting to our sinc function model. Since each additional model parameter adds to the processing time and has implications for performing real-time force measurements, we also investigated the accuracy of the direct fit models with and without parameters for asymmetry and rotation.

The results are shown in figure 4.10a. Cross-correlation exhibited a strong pixel bias regardless of the image model used (e.g. even with a symmetric Gaussian image

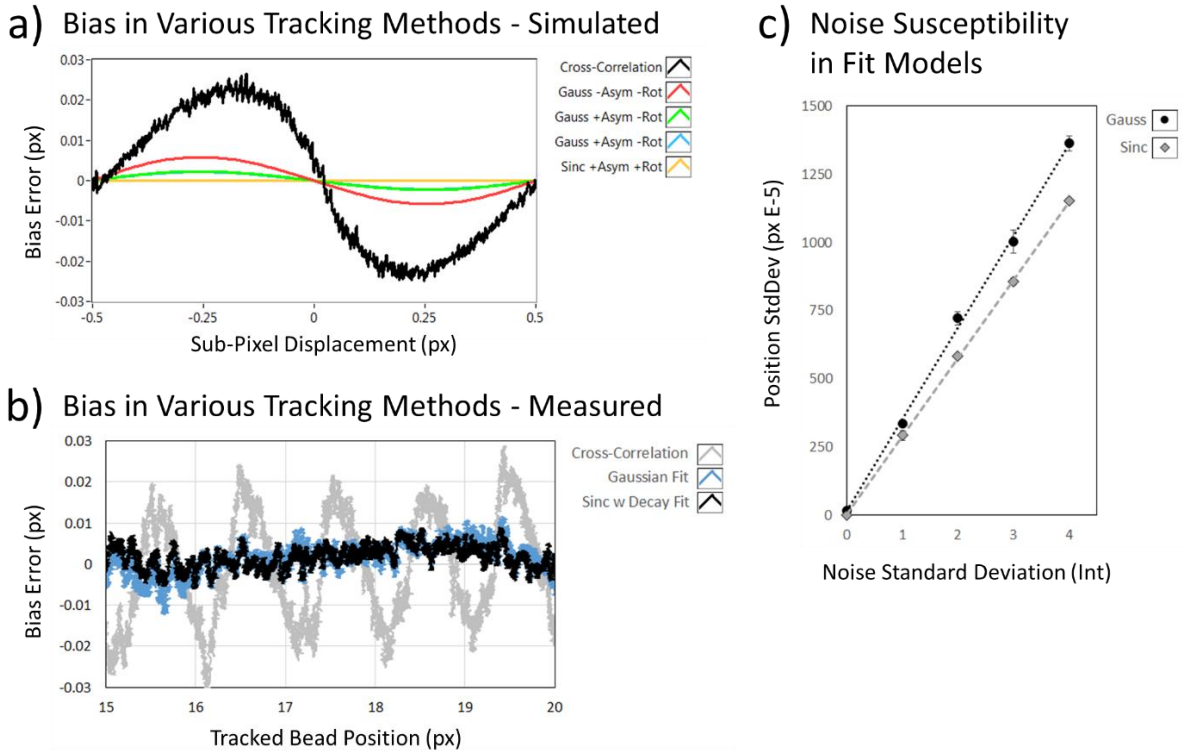

Figure 4.10 – Tracking Methods Compared: Pixel Bias and Noise
a) Simulated results of tracking a representative model bead image (figure 4.9b) using various tracking methods. Cross correlation yields a strong, periodic bias. A direct fit provides a dramatic improvement. Accounting for non-idealized image features such as ellipticity and rotation reduces pixel bias. **b)** Measured results of tracking a real bead using various tracking methods. Our measured results are in good agreement with our simulations. Both a Gaussian and sinc function fit reduced the pixel bias to below the noise threshold, but a sinc model yielded higher tracking precision. **c)** A simulated comparison of noise susceptibility in fit methods. Because the sinc function fits the extended ring pattern of the beads, it makes use of more of the available information in the image, resulting in a 15-20% lower standard deviation in tracking in conditions where bias is undiscernable.

model, the tracking bias was essentially identical). A direct fit with a symmetric Gaussian model improved the tracking bias substantially, and adding parameters to the Gaussian fit model for asymmetry reduced the bias further by 60%. Adding an additional parameter for rotation, however, had almost no affect. Fitting with a sinc function, even without parameters for symmetry or rotation, resulted in effectively zero bias. Although all the direct fit models we simulated yielded a pixel bias that was

already somewhat small due to the bead sizes in our particular instrument, it should be noted that with even marginally smaller bead sizes or larger degrees of asymmetry, the bias quickly increases to unacceptable levels, on par with cross-correlation tracking. In this case, the large reduction in bias that accompanies the inclusion of ellipticity parameters in a direct fit is very meaningful.

In figure 4.10b we show real tracking data obtain by sweeping a trapped bead linearly in a sample chamber, then subtracting off the best linear fit from the tracked motion to examine any deviations from the baseline. Cross-correlation techniques universally yielded a strong, periodic bias with an amplitude of about 0.02 pixels, in good agreement with the simulation. Equivalent to a peak-to-peak error of 7 nm, the bias from cross-correlation tracking data appears in force traces at high power as a distinctive oscillation. The bias error in the direct fit tracking with both Gaussian and sinc models was below the noise threshold, however tracking using the sinc model yielded results with a higher precision. This is likely because the sinc model uses more information from the bead image by fitting the rings around the central bright peak, whereas a Gaussian fit discards this information. Indeed, when adding a variable amount of Gaussian-distributed noise to the image, the sinc-function model tracks a simulated bead with 15 to 20% greater precision, as shown in figure 4.10c, and at comparable speeds. For these simulations, in order to examine the noise performance

of the two fit models independent of pixel bias, we used a symmetric bead model with a radius large enough such that bias was less than 0.001 pixels.

In summary, pixel bias presents a significant problem in applications where real-time tracking with nanometer accuracy of moving particles is required. Cross-correlation methods, though fast, are highly susceptible to peak-locking, and though direct fit methods show improved performance, they are slower, and may still exhibit peak-locking when the image becomes small enough, or for images with a large degree of ellipticity and rotation. We have presented a solution to peak-locking which enables us to track the bead images produced by our instrument at over 100 fps and without significant pixel bias, and resolve steps in bead motion down to 0.72 nanometers, which we demonstrate in section 4.6.

4.4. Noise, Stability, and Resolution in Optical Tweezers Measurements

A time-series measurement of the position of a bead within an optical trap, whether by photodiode BFPI or image-based tracking, fluctuates about a mean value, due to both detector noise and the random Brownian motion of the trapped object. Although the thermal fluctuations of Brownian motion reflect the true instantaneous position of our trapped particle at any given time, when we consider the typical goal

of a single molecule experiment to measure the small, relative changes in the extension of a DNA tether induced by a motor protein, it is clear that both Brownian motion and detector noise act in the same manner to limit the precision of this measurement. More specifically, these fluctuations dictate the bandwidth with which one can make a determination of tether length to within a certain resolution.

The root mean square of the Brownian fluctuations of a trapped particle is given by $\sqrt{k_B T/k}$ according to the equipartition theorem. Thus without averaging successive data points, a change in tether extension ΔL results in a statistically significant change in measured bead position only when $\Delta L \geq \sqrt{k_B T/k}$, which is referred to in the case of the equality as the thermal limit [Neuman and Nagy 2008]. For typical experimental values of the trap stiffness k, this is on the order of 5 to 10 nm. One can average collected data points over a time t_{ave} to reduce the thermal limit to $\Delta L = \sqrt{k_B T/k t_{ave} f^*}$, where f^* is the lower value between the data sampling frequency f_s and the inverse autocorrelation time of the optically trapped bead $f^*_{max} = 1/\tau_{AC}$. The bead autocorrelation time limits the utility of increasing sampling rate in an optical trap to increase measurement resolution, since adjacent data points become increasingly correlated for $f_s > f^*_{max}$ [Lansdorp and Saleh 2012]. The autocorrelation time is given by $\tau_{AC} = \beta/k = 1/2\pi f_c$ where f_c is the bead's corner frequency and β is the viscous drag coefficient, both of which are defined and

discussed further in section 2.3. Thus, the maximum useful sampling frequency $f^*_{max} = k/\beta$ results in a thermal limit of resolution when averaging for a time t_{ave} of

$$\Delta L = \sqrt{\frac{k_B T \beta}{k^2 t_{ave}}}$$

This is the fundamental physical limit of resolution in a single trap optical tweezers instrument. The other sources of noise present in an optical trap detection system (shot noise, electronic noise, etc, each with a variance σ_i) add to the variance of the time series measurement of bead position, and thus increase the minimum achievable resolution threshold of a measurement:[8]

$$\Delta L = \sqrt{\frac{1}{f^* t_{ave}}\left(\frac{k_B T}{k} + \sum_i \sigma_i^2\right)}$$

In other words, each source of detector noise in an instrument increases the time over which one must average their data to reach a given level of resolution.

Our ability to average data points over time to yield greater measurement resolution is limited by two factors, the first of which is instrument drift. In addition to pointing fluctuations of the trapping laser itself, mechanical vibrations, settling of

[8] This is strictly true in the case of normally distributed noise, however still holds in approximation for other common noise distributions in instrumentation, e.g. Poisson distributed shot noise and gamma-distributed photodiode noise.

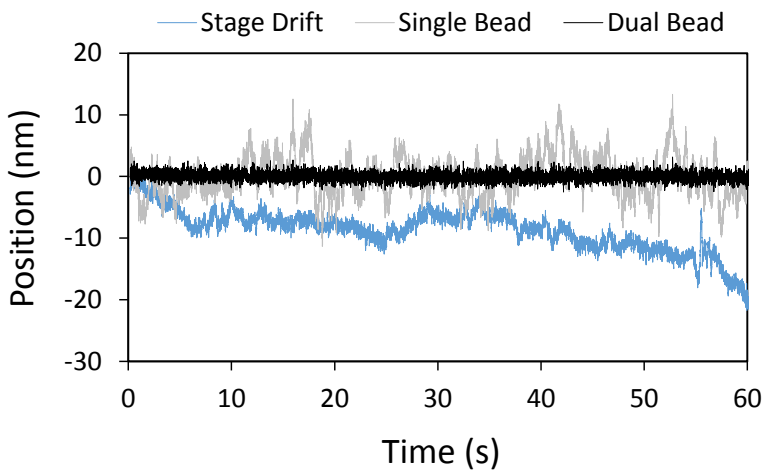

Figure 4.11 – Drift Noise in an Optical Tweezers Setup
Position measurements for a 500-nm polystyrene bead over time in the case of a bead fixed to a microscope coverslip (blue), a single bead held in a stationary optical trap (grey), and a differential measurement on a pair of beads held in stationary optical traps as described in section 2.5 (black). The fixed bead exhibits a characteristic drift on the order of 0.3 nm per second. A single trapped bead, meanwhile, exhibits large fluctuations on time scales under ~10 seconds due to laser pointing instability. A differential measurement removes these fluctuations, revealing the underlying high frequency Brownian process and detector noise.

mechanical positioning devices, and minute thermal fluctuations and varying coefficients of thermal expansion between materials all contribute to low-frequency instabilities between the various elements of an optical tweezers instrument (figure 4.11). Roughly speaking, for a drift velocity v_{drift} this requires that $t_{ave} \leq \Delta L / v_{drift}$. The second factor restricting t_{ave} is the physical time scales of the biological processes we wish to probe. It is clear that optical trapping is poorly suited to measuring molecular dynamics occurring on timescales faster than the corner frequency of the trapped reporter particle, and so it is fortunate indeed that many molecular motors process on DNA at rates of 10 to 100 Hz [Virulh Sa-yakanit et al. 2000]. Slowing down a mechanochemical process by limiting the concentration of its

catalytic substrate is also frequently employed to improve measurement resolution [Alberts et al. 2015].

Quantifying Noise in Optical Tweezers

Traditionally, noise in optical tweezers is quantified in the frequency domain by examining the power spectral density (PSD) of a trapped probe. As discussed in section 2.3, the theoretical PSD for an optically trapped particle follows a Lorentzian curve with a corner frequency $f_c = k/2\pi\beta$. Drift appears in the low frequency portion of the PSD, elevating the measured data above the expected theoretical curve. Detector noise, meanwhile, will be visible at high frequencies ($> k/\beta$) where the contributions to the PSD from the bead itself are minimal. The integrated or cumulative PSD further gives a measure of the variance of the trapped probe.

The Allan Variance (AVAR) is a time-domain measure of the frequency stability of a system [Barnes et al. 1971], which has recently found utility in characterizing the noise and stability of optical tweezers [Czerwinski et al. 2009; Gibson et al. 2008; Otto et al. 2010]. The AVAR is defined as

$$\sigma^2(\tau) = \frac{1}{2}\langle (x_{i+1} - x_i)^2 \rangle_\tau$$

where x_i represents the average of an interval of data over a time τ. The squared differences between means of neighboring intervals of length τ are averaged, and half this calculated value represents the AVAR for one time interval τ. For a time series data array of N points sampled with an average spacing Δt, τ can range from Δt to $\lfloor N/2 \rfloor$ through integer multiples of Δt. AVAR, or its square root the Allan Deviation (ADEV), is plotted as a function of τ, usually on a log-log scale, in what is known as a "sigma-tau" plot. The minimum of the sigma-tau plot represents the timeframe over which an averaged data series is most correlated, and precisely visualizes the point at which the low frequency deviations due to instrument drift overcome the benefits of longer averaging times to increase measurement resolution. In practice, there are several ways this formula can be applied to a finite data set, which we discuss further later in this section.

The AVAR for an optically trapped sphere has an analytic expression if we assume an infinite data series [Lansdorp and Saleh 2012; Vanvliet and Handel 1982], which is given by

$$\sigma^2(\tau) = \frac{2k_B T\beta}{k^2\tau}\left(1 + \frac{2\beta}{k\tau}e^{-\frac{k\tau}{\beta}} - \frac{\beta}{2k\tau}e^{-\frac{2k\tau}{\beta}} - \frac{3\beta}{2k\tau}\right)$$

the square root of which (the ADEV) is visualized for several different values of the trap stiffness in figure 4.12. For each trap stiffness, the corresponding corner frequency is indicated by a vertical dashed line. The peak of the ADEV scales with the

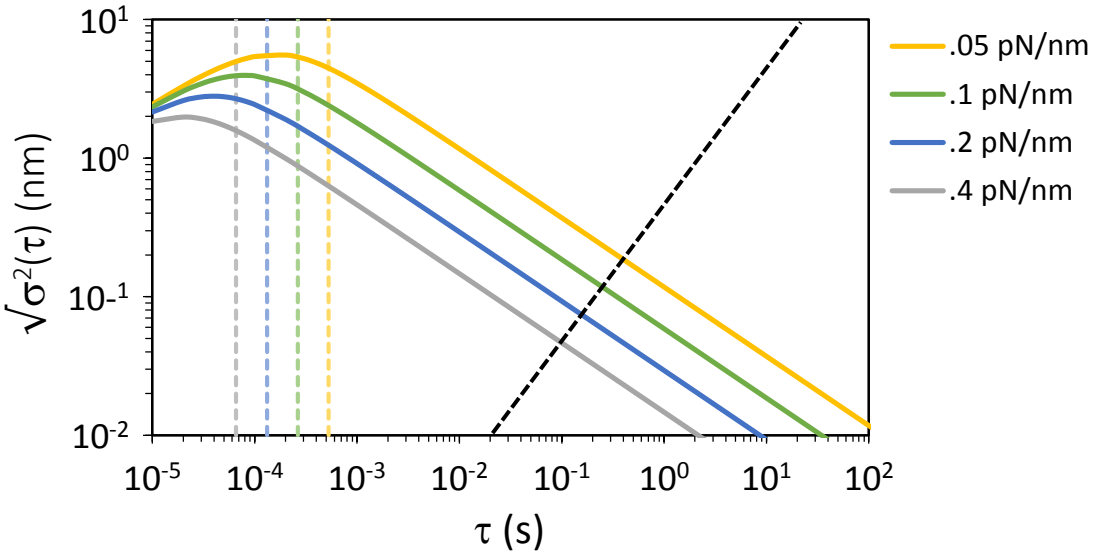

Figure 4.12 – Allan Deviation of an Optically Trapped Microsphere
The sigma-tau plot of the Allan Deviation (ADEV, square root of the Allan Variance) is shown for several values of the trap stiffness. For each trap stiffness, the corresponding corner frequency is indicated by a dashed line. The black dashed line displays the ADEV of a linear drift of 0.5 nm/s.

autocorrelation time as approximately $\tau_{max} = 1.89\,\beta/k$. For values of τ well below τ_{max}, the behavior of the ADEV reflects the rate at which the particle diffuses, and so the ADEV decreases for smaller time intervals over which the particle position becomes increasingly unchanged. For values of τ well above τ_{max}, the ADEV approaches that of the thermal limit, decreasing as $1/\sqrt{\tau}$. The ADEV of a hypothetical drift of 0.5 nm/s, meanwhile, is shown by the black dashed line. Thus for data obtained from an optical trapping instrument, of which drift is an inescapable part, the sigma-tau plot of the ADEV will reach a minimum after which the ADEV rises with larger values of τ, as it is increasingly dominated by the random rate of drift.

There are two subtleties to note when applying this formula to a finite set of data: the first is with regards to how the data is divided up into intervals of length τ,

and the second is with regards to which values of τ are chosen for calculation. The "standard" AVAR uses non-overlapping intervals of τ, so we have for the first pair of intervals x_1 and x_2 the data points $(1, \dots, n)$ and $(n+1, \dots, 2n)$, respectively, and for the second pair x_2 and x_3 the points $(n+1, \dots, 2n)$ and $(2n+1, \dots, 3n)$, etc. The overlapping AVAR, in contrast, uses every possible consecutive interval of length τ, so while the first pair of intervals is the same as above, the second pair would be given by $(2, \dots, n+1)$ and $(n+2, \dots, 2n+1)$, etc. This more fully utilizes the available data and reduces the statistical error of the resulting calculation.

While this can be done for all possible values of τ ($\tau = n\Delta t$ where $n = 1, 2, \dots \lfloor N/2 \rfloor$) there is a large degree of statistical correlation in the AVAR error for neighboring τ's, particularly as τ increases, which is problematic for data fitting. Sampling τ on a base-2 log scale (i.e. $n = 1, 2, 4, 8, \dots$), referred to as an octave scale, reduces the correlation between adjacent data points while providing adequate sampling to extract the important features of the data [Lansdorp and Saleh 2012]. For the data presented below, we used fully overlapping intervals and sampled τ on an octave scale. One should note that regardless of whether standard or overlapping intervals are chosen and how τ is sampled, the largest values of τ on a sigma-tau plot will possess significant statistical error. However, one can obtain a statistically robust measure of the AVAR over any specific time scale by obtaining a data recording for a total time that is much longer than the largest τ of interest.

Power Spectral Density and Allan Deviation Measurements

To examine the performance of our instrument with respect to noise, resolution, and stability, we calculated the PSD, integrated PSD, and ADEV for a 500-nm bead held with our instrument in a stationary optical trap, and for which the position data was determined via image tracking as described in sections 2.5 and 4.3. We compare image tracking data for a differential measurement using a dual bead configuration to the data from a single trapped bead, both using image tracking (figure 4.13a), and back focal plane interferometry on a separate optical trapping instrument (figure 4.13b). Data was taken in all cases with the trap(s) at 400 mW laser power in the sample plane, corresponding to a trapping stiffness of 0.4 pN/nm. The frame rate for the image data was 350 Hz, while the BFPI data was sampled at 1 kHz without averaging. Data was taken for 100 seconds.

From the PSD in figure 4.13a, it is clear that the primary effect of making a differential measurement in our image tracking technique is to reduce low frequency noise (drift) occurring on timescales of 0.1 seconds and longer. The noise observed in the single bead measurement in the region of 0.1 to 1 seconds, the predominant component of which is likely laser pointing instability, is almost entirely eliminated in the differential measurement. As seen in the integrated PSD plot in figure 4.13a, this reduction in low frequency noise lowers the integrated spectral power by more than two orders of magnitude over the experimental bandwidth of interest.

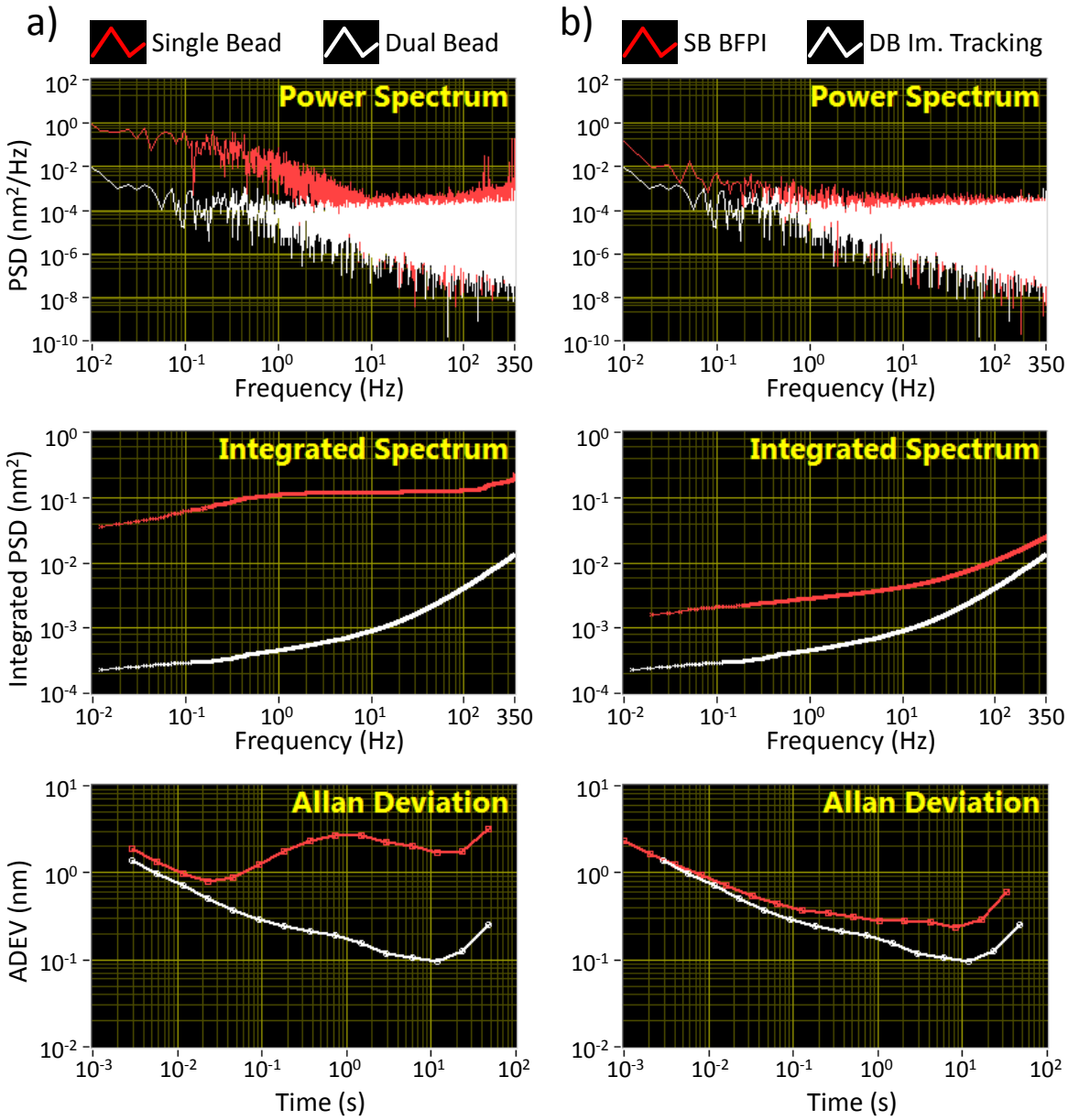

Figure 4.13 – Power Spectral Density and Allan Deviation Measurements
a) The power spectral density (PSD), integrated PSD, and Allan Deviation (ADEV) for our instrument, for position time series data from both a single bead configuration (red) and dual beam differential configuration (white) obtained through image tracking. The frequency domain plots highlight a two order of magnitude reduction in integrated spectral power for the differential measurement, while the time domain measurement highlights the stability of the instrument out to ten seconds. The ADEV data further confirms the capability of the instrument for resolving sub-nanometer changes in bead position. b) For the same measures as in (a), we compare our dual bead (DB) image tracking technique with back focal plane interferometry using a single bead (SB) (data was obtained from a different optical tweezers instrument using the same trap stiffness and a similar (1 kHz), acquisition rate). Our image tracking technique shows clear performance advantages at low frequencies, illustrating that this implementation can exhibit superior drift-resistance to BFPI.

The time domain data of the ADEV, meanwhile, shows that our system is quite stabile with regards to drift, with the ADEV decreasing steadily with increased tau to a value just below 1 angstrom at 10 seconds. The presence of two distinct local minima in the single bead tracking data suggest two independent sources of instability occurring at different frequencies. The first rise occurring around 0.1 seconds is likely, as previously mentioned, laser pointing instability, as this is almost completely eliminated by the differential measurement and so it is a noise source that couples into both traps uniformly. Past 1 second, the ADEV for the single bead begins decreasing again as pointing fluctuations are averaged towards the mean laser position. The second ADEV rise occurring around 10 seconds is likely a physical drift of the instrument components which affects the distance between the two traps in the sample plane, and thus affects both the single and dual bead measurements.

In figure 4.13b, we plot the dual bead differential tracking data from figure 4.13a against data obtained from a separate optical tweezers instrument using BFPI for a single trapped bead. To compare data obtained under similar conditions, we maintained the same trap stiffness (0.4 pN/nm) for both measurements, and limited the photodiode acquisition rate to 1 kHz. The power spectral data highlights the remarkable drift resistance conferred to the BFPI technique through its use of a Fourier plane. Remarkably, our differential image tracking technique is shown here to

measure bead displacement relative to its trapping center with a low-frequency stability that can match, or even better, the performance of BFPI.

4.5. Laser-Trap-Induced Heating Near a Gold Surface

The large laser intensities present at the focus of an optical trap present a potential threat to sensitive biological specimens through heating [Liu et al. 1995], and the standard trapping wavelength of 1064 nm has accordingly been chosen for its low absorption in water. However, even a minor temperature change can have a profound effect on the rate of an enzymatic process [Sizer 1943], and thus cannot be neglected. Temperature additionally affects the hydrodynamics of bead motion [Millen et al. 2014] and must therefore be considered in spectrum-based calibrations of trap stiffness for best accuracy. For these reasons, laser-induced heating has been thoroughly addressed in standard optical tweezers instruments, in which a 1064-nm laser is assumed to trap a micron-sized polystyrene microsphere in water, potentially near a glass surface.

Though the temperature increase in an optical trap was originally assumed to occur predominantly through direct laser heating of the trapped dielectric particle, it was shown by Peterman et al. [Peterman et al. 2003] that the most important contribution to trap-induced heating in standard trapping configurations is through

absorption of the trapping laser by the surrounding medium. Temperature was measured in this case via the power spectrum of a trapped bead, which is affected through the thermal energy $k_B T$ and the temperature-dependent viscosity of water. They measured a temperature increase of ~8 ºC/W at the laser trap focus with only a minor dependence on bead size, and observed a modest heat-sinking effect in the proximity of a glass surface due its marginally higher heat conductivity. They did not calibrate their measurements against a known temperature series, however, leaving room to question the accuracy of their model-based conclusions. Regardless, the order of magnitude of the effect is small considering the typical optical trapping powers on the order of several hundred mW.

Fluorescence thermometry is another method for measuring temperature in fluid samples, and, like Brownian motion analysis, can provide information on micron spatial scales without the use of an invasive probe [Lou et al. 1999]. The technique exploits the known temperature dependence of the emission properties of a fluorescent dye or nanoparticle, such as emission peak wavelength, fluorophore lifetime, or quantum yield [Vetrone et al. 2010]. Rhodamine B (RhB), a common and widely available fluorophore, is frequently used for this purpose. The intensity of RhB emission increases with lowered temperature, changing by more than a factor of 2 between 50 and 10 ºC [Karstens and Kobs 1980; Natrajan and Christensen 2009]. Ebert et al. used fluorescence ratio thermometry to measure laser-induced heating in

an optical trap consisting of two counter-propagating, divergent beams operating at 1064 nm, and found a maximum temperature increase at the trapping center of ~13 ºC/W [Ebert et al. 2007], in reasonable agreement with Peterman et al..

With the goal of performing optical trapping experiments near metallic surfaces, the potential for laser-induced heating must be considered anew. Gold films and nanoparticles have garnered intense interest due to their unique combination of a large negative component of the dispersion constant leading to plasmonic effects in the visible spectrum, and resistance to oxidation leading to a high compatibility with biological buffers. These features make gold films and plasmonic nanostructures prime candidates for integration with optical trapping. The plasmon-enhanced absorption of NIR wavelengths by gold nanoparticles has been studied, primarily in the context of photothermal therapy as a cancer treatment [Pattani and Tunnell 2012], however the temperature increase caused by a 1064-nm focused laser trap near a flat gold surface or film has not been measured.

We used Rhodamine B as a temperature-sensitive probe to examine the laser-induced heating effects of an optical trap near a flat gold surface. In order to calibrate the fluorescence emission intensity with temperature, we built a temperature control system for our microscope fluid chambers from a thermoelectric Peltier device (Hebei I.T. TEC1-12710) controlled with a variable power supply (figure 4.14a). To measure the device's temperature as a function of applied voltage, we embedded a thermistor

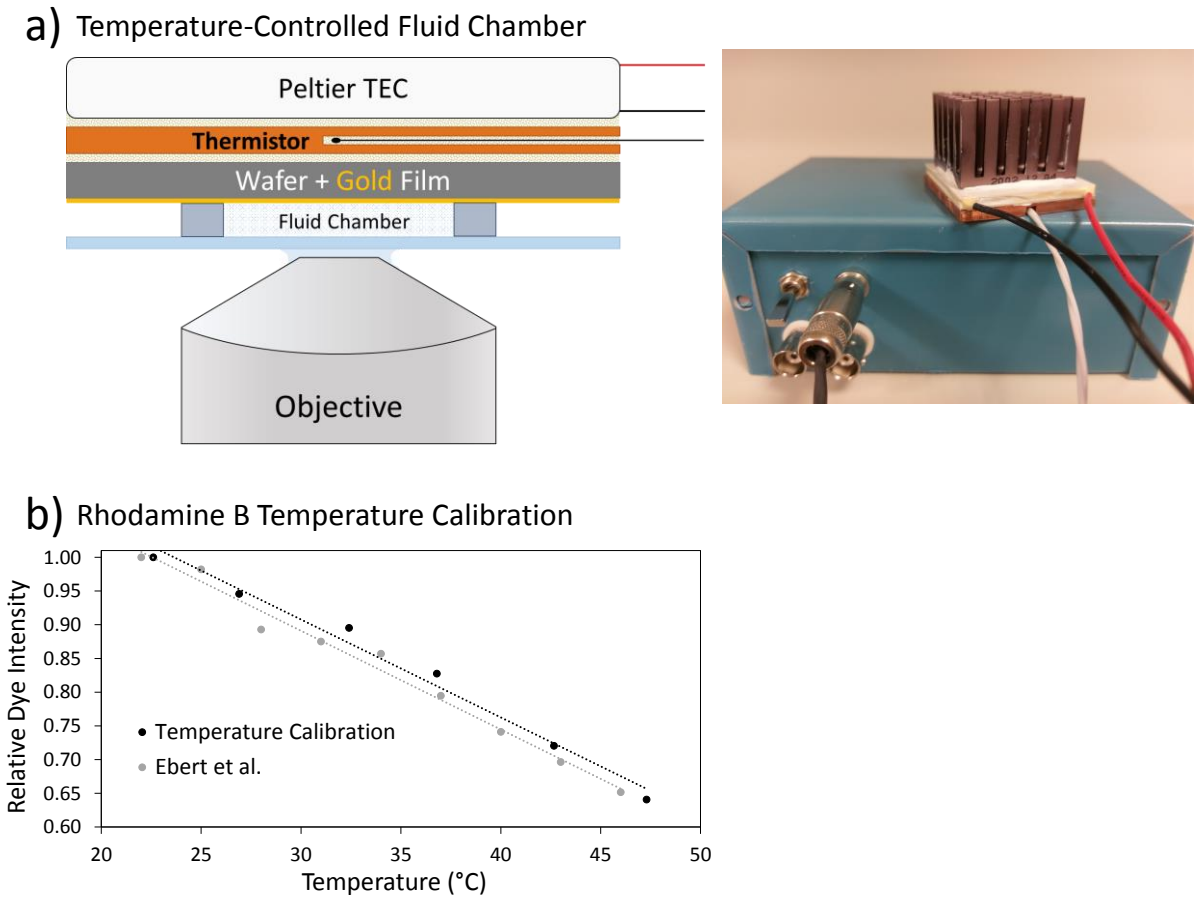

Figure 4.14 – Fluorescence Intensity vs. Temperature Calibration of Rhodamine B
a) A thermoelectric Peltier device to control temperature within a fluid chamber. A diagram (left, not to scale) shows the assembly (image, right) mounted on a scope. Temperature at the hot side of the TEC was monitored as a function of voltage applied to the TEC by a thermistor embedded in a thin copper block with thermal paste. The block was fixed between the TEC and the sample with thermal paste. The fluid cell was composed of a wafer with a 100-nm evaporated gold film and a microscope coverslip. **b)** The results of the temperature calibration show good agreement with previously published values.

with a known temperature coefficient of resistance into a thin copper block and fixed this to the heating side of the Peltier device with thermally conductive paste. We then applied this device to the back side of a fluid chamber mounted on our optical trapping setup. Our fluid chamber was built between a standard silicon wafer with a 100-nm evaporated gold film on the interior surface, and a microscope coverslip

spaced by two strips of double-sided tape. The large thermal conductivity of Silicon and gold allowed our temperature control device to heat the fluid in the flow cell chamber.

We introduced into our flow cell a 10 μm solution of RhB diluted in water, and varied the temperature via the Peltier device from the room temperature of 22.6 ºC up to 47.3 ºC, in a temperature and humidity-controlled room[9]. We allowed the system to equilibrate for several minutes between each temperature measurement. Fluorescence was generated by a 555 nm laser (CrystaLaser model#) emitting 2.0 mW of power and collected on an EMCCD camera (Andor iXon Ultra 897) with 50 ms exposures. Our calibration results, shown in figure 4.14b, compare very well against the data obtained by Ebert et al. for the same dye. The relative intensity of fluorescence emission was found to vary from our room temperature reading by -1.45 ± 0.09 percent per degree Celsius.

Following calibration, we investigated the temperature changes induced by our optical trap when focused at the gold-water interface. An example fluorescence image frame, converted to a temperature distribution map, is shown in figure 4.15a and the corresponding line scan along the vertical direction is shown in figure 4.15b. From similar data collected at varying laser powers, we obtained the maximum temperature

[9] We chose to stop at 50 ºC and did not test the limits of the Peltier device, however by all indications it can achieve significantly higher temperatures.

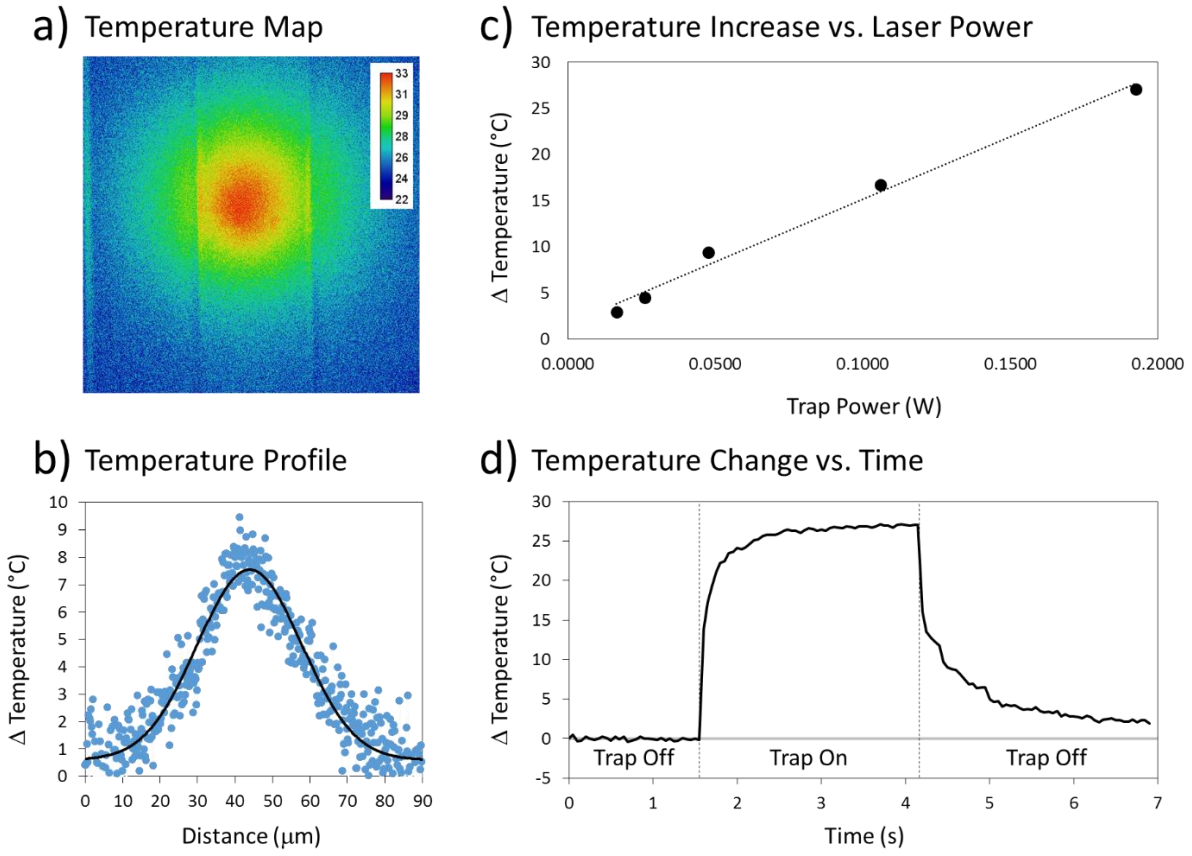

Figure 4.15 – Laser-Induced Heating Near a Gold Surface
a) Temperature map obtained via fluorescence ratio thermometry showing the heat flow from irradiation with a trapping laser. **b)** A line profile of the temperature map in (a) shows the steady-state heat distribution extends tens of microns from the laser focus. **c)** Temperature increase as a function of trapping power. A slope of 136 ± 8 ºC/W was obtained. **d)** Time evolution of the maximum temperature shows a rapid rise time on the order of milliseconds when the laser is turned off, and a significantly slower dissipation rate when the laser is turned off.

increase as a function of trap power shown in figure 4.15c. We observed a temperature increase of 136 ± 8 ºC/W, which, not unexpectedly, is significantly higher than the values of 8 to 13 ºC/W reported previously for a water and glass chamber. This is attributed to the increased optical absorption of the trapping laser by the gold film.

Heat is produced in metals when incident electromagnetic radiation couples into available electronic or vibrational states in the material to produce excited states which then dissipate through lattice phonons [Brown and Arnold 2010]. To first order, the rate of heat generated by an electromagnetic wave incident on a metal will be proportional to the optical absorption, as metals have very low quantum yields [Govorov and Richardson 2007]. Thus generated, the heat distribution in a material is then subject to the heat equation

$$\rho C_p \frac{\partial T}{\partial t} = \nabla(k\nabla T) + Q$$

which relates the temperature distribution T caused by a heat source Q to the material density ρ, specific heat capacity C_p, and thermal conductivity k. For most heat source distributions Q, this requires a numerical solution.

By dimensional analysis [Sparks 1976] we can note the characteristic time constant $\tau_l = l^2 \rho C_p / k$ which suggests the time for heat to diffuse a distance of ~1 μm should be ~1 μs in gold and ~1 ms in water. Since our fluorescence signal is measuring the temperature of the water surrounding the gold surface, the 1 ms timescale is most relevant, and indeed we find a time constant of ~50 ms for the temperature distribution to reach a steady state over a distance of several tens of microns when the laser is turned on (figure 4.15d). The long characteristic length constant and short characteristic time constant are both reflective of gold's high

thermal conductivity of ~315 W/m·K, over 500 times greater than water. The specific heat capacity per unit volume, ρC_p, is meanwhile only about 1.7 times smaller in gold than in water, and so the difference in thermal conductivity between gold and water should dominate their respective heat distributions for an equivalent heat source Q. However, the absorption of 1064 nm light by gold and by water is of course quite different.

We can estimate the fraction of plane wave light intensity absorbed by a gold film for 1064 nm light at a normal angle of incidence. Gold has an absorption coefficient α of 7.8x10^5 cm^{-1} at 1064 nm, resulting in a skin depth $1/\alpha$ of 12.8 nm, so with a 100-nm film we can safely assume that essentially all the light not reflected at the water-gold boundary is quickly absorbed. The fraction of absorbed light is given by $1 - |r^2|$, where r is the reflection coefficient equal to $(n-1)/(n+1)$. The refractive index n is equal to $\sqrt{\epsilon}$. The Drude model works reasonably well to give the permittivity ϵ when the frequency ω of the light incident on a metal satisfies the condition $\omega_\tau \ll \omega \ll \omega_P$, where ω_τ is the damping (or collision) frequency and ω_P is the plasma frequency. From the equation of motion of a free electron in a metal, the Drude model gives

$$\epsilon = 1 - \frac{{\omega_p}^2}{\omega^2 - i\omega\omega_\tau}$$

From this we can obtain an approximate absorption fraction of $2\omega_\tau/\omega_p$ that is independent of wavelength [Lin 1999]. From the values for gold ω_p = 9.062 eV and ω_τ = 0.070 eV [Ingram et al. 1990] we confirm that at 1064 nm (1.17 eV), ω marginally satisfies our stipulated conditions, and we arrive at an absorption fraction of 0.015. This is remarkably close to the actual value of 0.027 [Polyanskiy 2016] given the simplicity of the model.[10]

Though the shape of the focused laser incident on the gold surface (and thus the shape of the heat source distribution Q) is not a uniform plane wave, this is a reasonable approximation given that the characteristic length scale of the steady-state heat distribution (figure 4.14b) is large with respect to the beam diameter [Sparks 1976]. For the case of an absorption coefficient of 0.034 and a uniform NIR (785 nm) optical intensity across a beam diameter of ~500 nm incident on a gold-water interface, the steady-state solution to the heat equation has been solved numerically in COMSOL, with an obtained value of $\Delta T \approx$ 120 °C/W [Chen et al. 2015], in good agreement with our results for a very similar heat source.

This level of heat generation is potentially problematic. Confirming our postulate that the shape of the heat source is not critical as long as it is small with respect to the characteristic length scale of the heat distribution, we found that the maximum

[10] Meanwhile, the absorption of the same plane wave by water follows the Beer-Lambert Law with an absorption coefficient of 0.61 cm^{-1} (around 6 orders of magnitude less than gold), leading to an absorption fraction on the order of $5x10^{-5}$ through the focal volume.

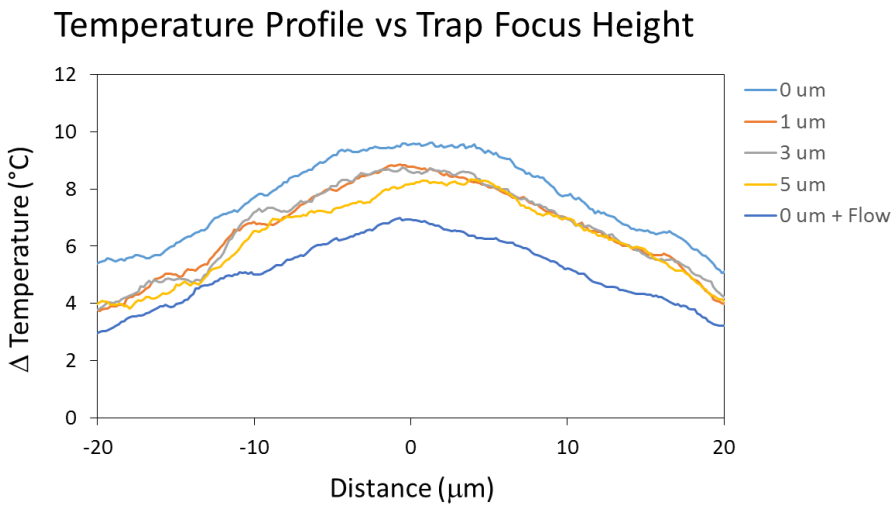

Figure 4.16 – Heating vs Focal Height
Temperature profiles are shown with the laser focused between 0 and 5 μm above the gold surface, with minimal variation. Turning on a flow of 50 μL/hour lowered the peak temperature by 27%.

temperature varied minimally when the focal distance from the gold surface was varied between 0 and 5 μm (figure 4.16). However, the differing time constants for heating and cooling displayed in figure 4.15d suggest that the rate of heat dissipation to the surrounding fluid is exacerbatory, which is confirmed by a 27% reduction in peak temperature change when a modest flow of 50 μL/hour was induced in our fluid chamber. Additionally, one may see further temperature reduction by using the Peltier device described previously as an active cooler applied to the back of the flow cell, and by circulating cooled water through the flow cell. It may also be worth investigating other substrates such as silver, or other trapping wavelengths to reduce the laser absorption if integration with metallic structures is to be achieved.

4.6. Instrument Data

Step Size Measurements

Resolving small changes in the position of an optically-trapped particle relative to the trap center is the bottom line for an optical tweezers instrument, and is one of the most informative characterizations that can be performed as it reflects the cumulative effects of all instrument parameters that influence measurement accuracy and precision, including tracking precsion, instrument stability, and all sources of measurement noise. Though individual aspects of an instrument may exhibit high precision, the full step size measurement is only as good as its weakest link.

Image-based particle tracking has been demonstrated to be capable of determining the position of an object fixed to a coverslip to within a few angstroms [Huhle et al. 2015]. Several other groups have applied image-based tracking to optically trapped particles rather than stationary particles and demonstrated particle localization to within a few nanometers. For example, Towrie et al. used centroid tracking and the equipartition theorem to determine force in an optical trap over a period of four seconds, however their method cannot measure bead displacement relative to the trap center or make force measurements at high bandwidth and is thus unsuitable for most single molecule experiments [Towrie et al. 2009]. Otto et al. have also demonstrated that they can determine the absolute position of an optically-trapped particle with low error, potentially with a resolution of 1 nm as predicted by

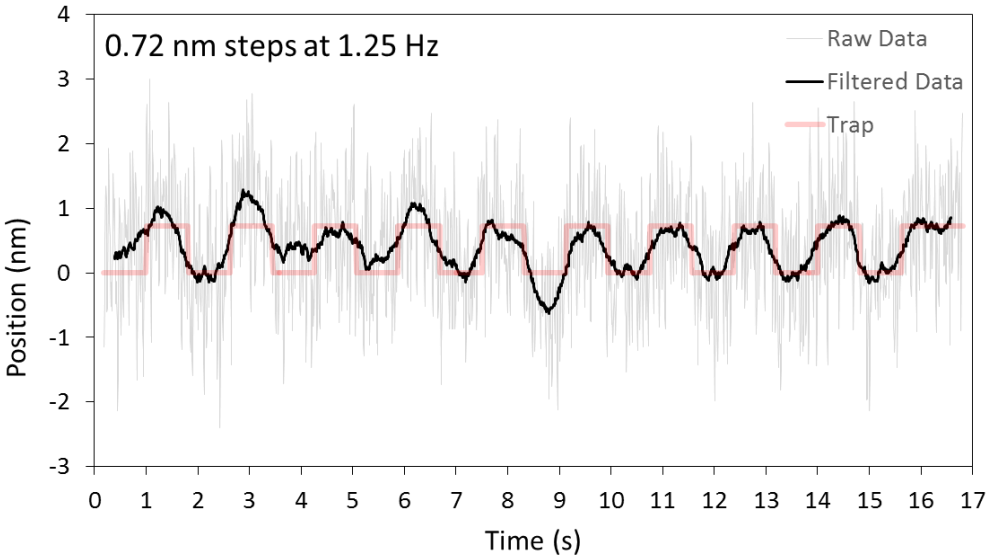

Figure 4.17 – Resolution of 0.72 Nanometer Steps
An untethered bead was caught in each trap. One trap was held stationary as a reference, and the second trapped was moved in steps of 0.72 nanometers every 0.8 seconds. Bead position was tracked according to sections 2.5 and 4.3.

Allan variance, however they give no method for measuring relative displacement to the trap center, or force [Otto et al. 2011]. In fact, no one has demonstrated an effective, image-based method for determining the relative position of a bead within an optical trap with accuracy and speed, due to the difficulties in knowing the true location of the drifting trap center at any given time.

In section 2.5, we showed for the first time that image-based tracking can determine the position of an optically-trapped particle relative to its trap center to within one nanometer, which was done as we moved a trapped bead across a distance of 16 microns via an AOD. Here, we show the minimum detectable bead displacement this technique can resolve. We held a reference bead in one trap, and stepped a second bead in the other trap in a square wave motion and tracked its

position using the methods described in section 2.5 and 4.3. Shown in figure 4.17, we are able to clearly resolve 0.72-nanometer steps. In the future, this measurement can be repeated with a pair of tethered beads stretched to high force. The rigid linker between the two beads reduces the amplitude of Brownian fluctuations and greatly improves signal to noise ratio, and is expected to yield even higher step resolution.

Stretching DNA

Chromosomal DNA is densely packed within the nuclei of eukaryotic cells[11], coiled tightly around proteins that regulate cellular activity and gene expression [Killian et al. 2012]. The mechanical properties of DNA thus play an important role in mediating chromatin structure, and are vital to understanding the mechanisms of the many proteins that interact with or directly manipulate DNA molecules. DNA looping, for example, has recently been implicated to direct the fundamental mechanism of epigenetic inheritance [Brennan et al. 2016], and the elastic and torsional properties of DNA are known to be intimately involved in the regulation of DNA transcription [Ma et al. 2013].

DNA can be modeled as a polymer [Marko and Siggia 1995; Wang et al. 1997], with a contour length L_0, a persistence length L_p, and an elastic modulus K_0. The

[11] Laid out end-to-end, the human genome would measure around ~2 meters in length, while the mammalian cell nucleus is on the order of 10 microns in diameter.

smallest unit of the DNA polymer is the base pair, measuring 0.34 nm in length [Banfalvi 1994], and a DNA's contour length is accordingly 0.34 times its number of base pairs. Persistence length describes the characteristic length over which a polymer resists bending, and for DNA in physiological salt concentrations, it is on the order of 50 nm. DNA, therefore, is quite rigid over length scales comparable to its helical pitch (~3.5 nm), but can be considered a flexible chain when the contour length is much larger than the persistence length. In the absence of force, the behavior of a long, flexible DNA polymer is entropically dictated, due to the large number of configurations the polymer can adopt. A unit vector tangent to the DNA axis exhibits essentially a random walk through space over length scales large with respect to the persistence length. Thus, it requires force to stretch the end-to-end extension of the DNA polymer towards its true contour length L_0. As the DNA is extended and straightened under force and its available configurations are reduced, the molecule transitions into the so-called enthalpic regime, where its force-extension behavior becomes dominated by its elastic modulus K_0. Wang et al. [Wang et al. 1997] extended a force-extension model by Marko and Siggia [Marko and Siggia 1995] to develop a force-extension relationship that describes DNA well through both the low-force entropic regime, and the high-force enthalpic regime:

$$F = \left(\frac{k_B T}{L_P}\right)\left[\frac{1}{4(1 - x/L_0 + F/K_0)^2} - \frac{1}{4} + \frac{x}{L_0} - \frac{F}{K_0}\right]$$

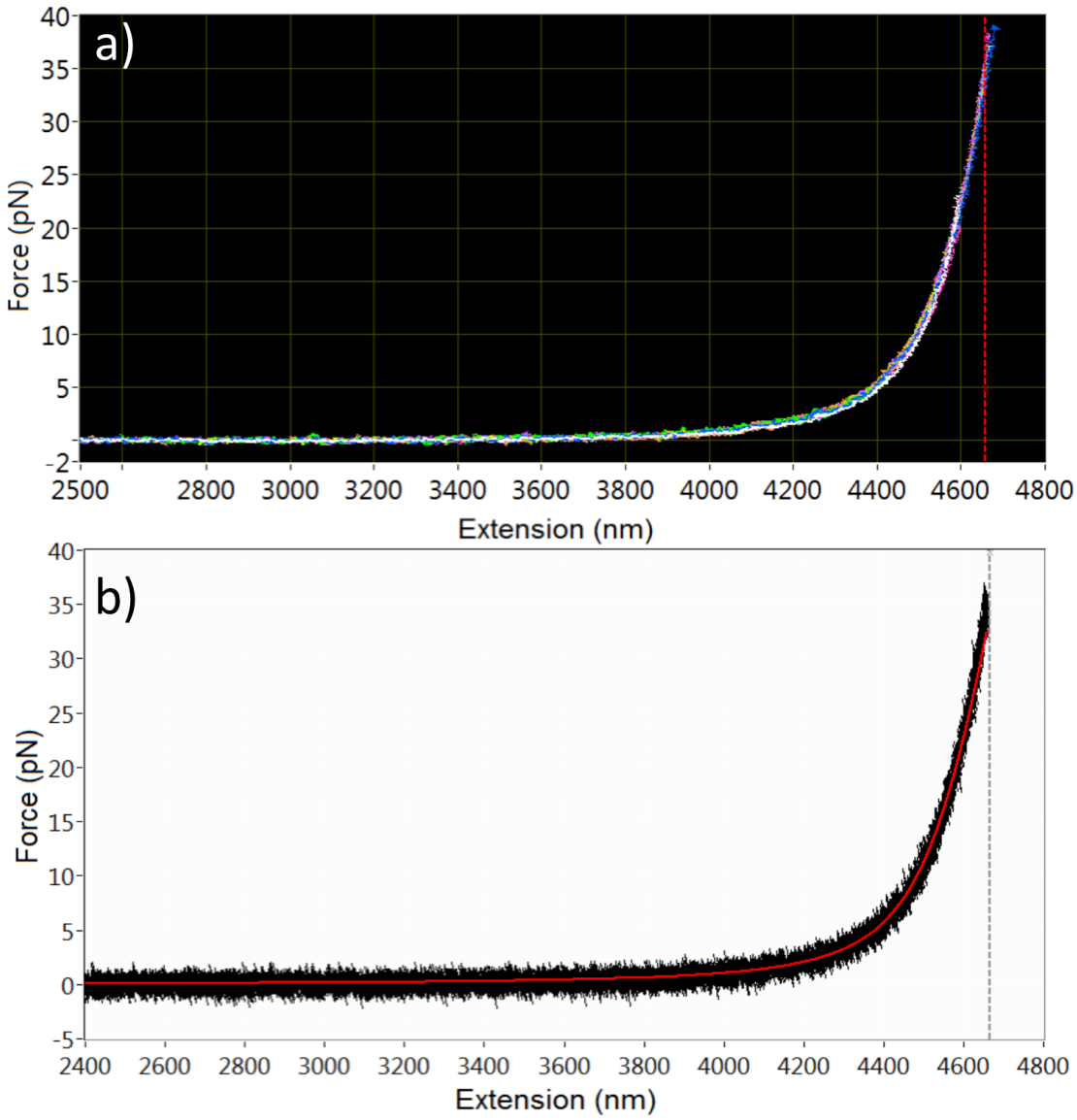

Figure 4.18 – Force-Extension Curves for 13.7 kbp DNA

a) Force-Extension curves are shown for ten stretching traces of the 13.7 kbp template described in section 3.2. The contour length of 4659 nm is indicated in red. **b)** A selected raw trace is shown unfiltered with the modified Marko-Siggia model prediction overlaid in red for L_P = 50 nm, L_0 = 4659 nm, and K_0 = 1300.

We obtained force-extension data for the 13.7 kbp template described in section 3.2, by forming a dumbbell tether and stretching under conditions of constant trap power and constant velocity in 150 mmol salt (phosphate buffered saline). The results of ten traces are shown in figure 4.18a. The red dash indicates the contour length

calculated from the template length to be 4659 nm. Figure 4.18b shows the raw, unfiltered data from one selected trace. The theory overlay in red indicates the prediction for the modified Mark-Siggia model using L_P = 50 nm, L_0 = 4659 nm and K_o = 1500.

The traces were fit to the modified Marko-Siggia model to extract fit parameters for persistence length (51.4 ± 2.7 nm), contour length (13740 ± 20 bp), and elastic modulus (1559 ± 161 pN). The results are shown in figure 4.19, where error bars represent the standard deviation obtained from the fit covariance matrix. The persistence length of DNA at the physiological salt concentration used here is generally quoted to be approximately 50 nm, in good agreement with our results,

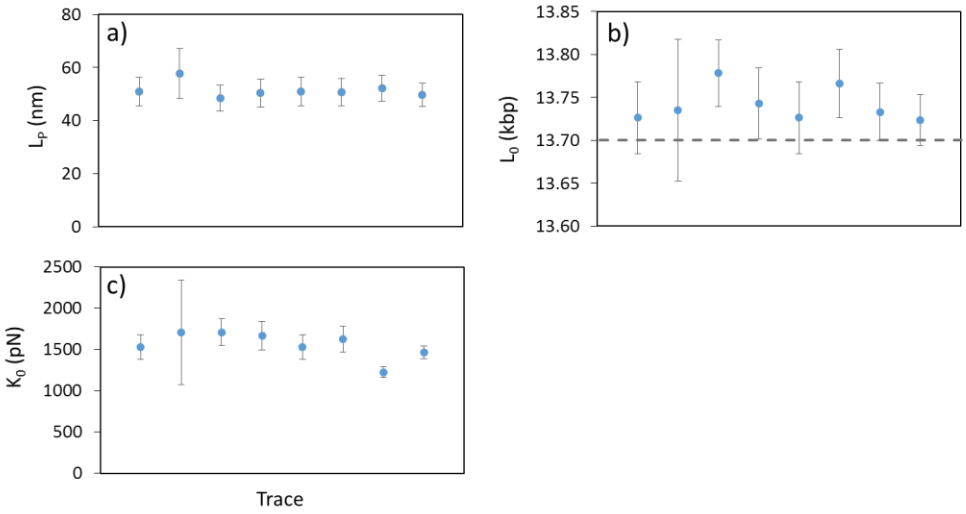

Figure 4.19 – Fit Parameters from DNA Elasticity Model
The DNA stretching curves from figure 4.15 were fit with the modified Marko-Siggia model and parameters for persistence length (L_P), contour length (L_0), and elastic modulus (K_0) were determined. Error bars represent the standard deviation from the fit covariance matrix. a) L_P was found to be 51.4 ± 2.7 nm, on the high end but within the range reported by the literature. b) L_0 was found to be 13740 ± 20 bp, with an expected value of 13702 bp. c) K_0 was found to be 1559 ± 161 pN, significantly higher than the values of 1100-1300 pN typically reported, however a large error in this parameter is expected due to the force range and sample size of our data.

however reported values in the literature are between 43 and 50 nm [Brinkers et al. 2009; Brunet et al. 2016; Manning 2006]. Our length is also slightly higher than the expected value of 13702 bp, but within error. Our measured elastic modulus is significantly higher than the typical values of 1100-1300 pN reported in the literature [Wang et al. 1997], however there is generally a large error in this parameter as it is heavily reliant on high-force data for its accuracy. Few of our traces went above 30 pN.

Unzipping DNA

DNA unzipping describes the mechanical disruption of the DNA double helix into its two constituent strands by breaking the hydrogen bonds between complementary nucleobases that hold the strands together. Unzipping has become a powerful technique for studying protein-DNA interactions [Hall et al. 2009], owing to the fact that a bound protein alters the energy landscape in a manner that is detectable through unzipping, with nearly base-pair resolution. The force-extension relationship for an unzipping trace can be predicted well with a basic statistical mechanical treatment [Bockelmann et al. 1998], taking into account the different base-pairing energies for A:T and G:C, the hydrogen bond stacking energies of neighboring base pairs, the energy in the unpaired bases that have been disrupted, and the tension in the DNA arms of the unzipping fork.

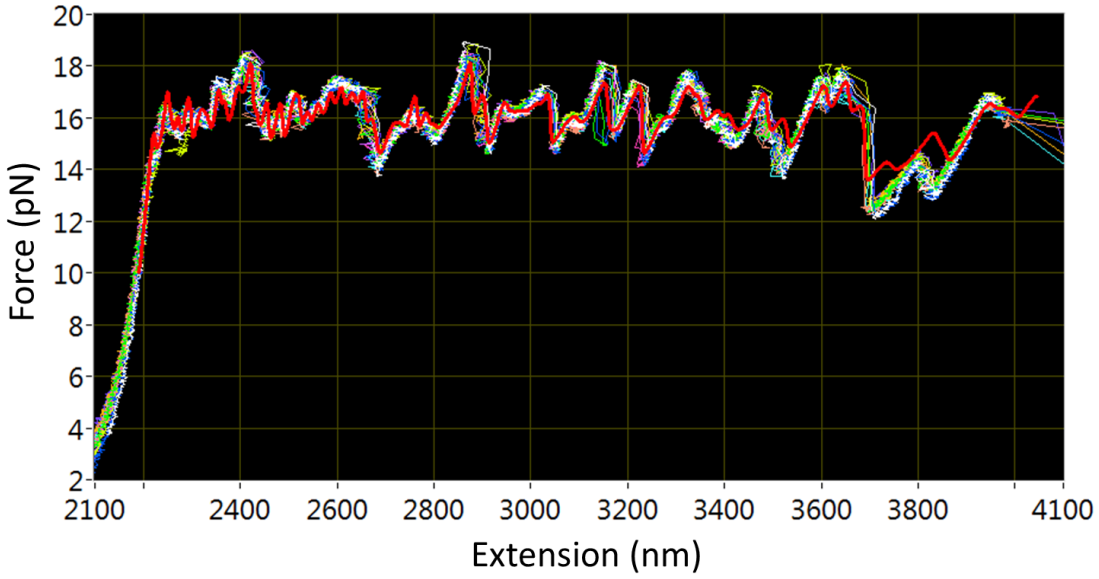

Figure 4.20 – Unzipping a 2 kb DNA Template
A 1980-bp DNA template was mechanically unzipping in our dual optical trap, and the force-extension relationship was obtained. Ten traces are displaced, with the theoretically-predicts value overlaid in red.

We used our instrument to unzip through a 1980-bp DNA template and performed image-tracking to determine the force-extension relationship of the DNA through the unzipping process. Results for ten traces are shown in figure 4.20, along with the expected theoretical outcome in red. The data is in excellent agreement with the theory, highlighting the high degree of accuracy of our calibration and detection techniques. The data were obtained at a constant trap stiffness of 0.15 pN/nm, and a constant trap velocity of 20 nm/s. The average displacement of the bead from the trap center during unzipping was 80 nm, well within the trap's linear range.

The data we have obtained validates the ability of this instrument to make sensitive, accurate, and precise single-molecule measurements of force and displacement on biological templates with nanometer resolution using image tracking.

5. Conclusion and Future Directions

In summary, we have built an advanced, high-resolution optical tweezers instrument that incorporates time-shared dual trapping, single-molecule fluorescence, and image-based position detection in an entirely free-standing[12] setup. We have developed a set of techniques and algorithms that allow us to resolve sub-nanometer steps of trapped particles relative to their trapping centers, a feat which has never been accomplished using image-based tracking. Furthermore, we have implemented these capabilities in an entirely reflection-based setup, without the use of a second microscope objective. We have also made the first temperature measurements of optical trap heating near a gold surface. To realize a highly-versatile and integration-ready instrument, we have developed a novel, extra-objective oblique illumination (EOOI) technique that enables ultra-darkfield illumination and simultaneous optical trapping in opaque samples, as well as simultaneous fluorescence imaging. We have developed a set of robust and efficient protocols for generating several types of fluorescently-labeled DNA templates, and a novel flow-cell design in order to label DNA containing multiple tagged sites with quantum dots under force. Finally, we have demonstrated high-quality data on biological templates via the stretching and unzipping of DNA using our instrument.

[12] I.e., not built around a commercial microscope body.

Real-Time Detection and Feedback

Our image tracking has, as a proof of concept, been implemented on our available equipment which is not specialized for high speed video microscopy. Our position and force measurements are thus made in post-processing, and our acquisition rates are limited to a few hundred Hz. Our immediate next steps are to implement a system for high-speed image acquisition and processing in order to achieve high-resolution position detection on-setup and in real time. We have purchased a high-speed CMOS camera (Mikrotron EoSens CL), a high-intensity LED illumination source (Thorlabs Solis-445C, 7 Watts at 445 nm) and an LED driver (Thorlabs DC2200) capable of providing 10.0 A, 50 V, and modulating the LED output as a square wave at up to 100 kHz. The camera can acquire the cropped region of interest which contains our traps at up to 80 kHz, however the maximum rate of acquisition we are interested in is 10 kHz. The bright illumination is necessary to achieve a good signal-to-noise ratio at short exposure times.

Data processing and synchronization will be the most significant technical challenge. The Camera Link protocol our camera uses for transferring data will not limit our acquisition rate, however for real-time image tracking at kHz frame-rates, parallel, high-speed processing of the acquired image data is a necessity. This is generally accomplished either by implementing tracking algorithms on a CUDA-enabled GPU [van Loenhout et al. 2012], or using embedded FPGA processing

[Towrie et al. 2009] to build a so-called "smart camera." Because of our familiarity with FPGAs and the central role our current FPGA plays in our instrument, we chose the FPGA implementation for real-time image processing. We purchased an FPGA frame grabber (National Instruments PCIe-1473R) which will enable us to build an embedded system for high-speed, parallel image processing.

Beyond embedded particle tracking, the processed image data also needs to be integrated and synchronized with the optical trapping instrument to enable high-performance feedback and control tasks, in which the trap powers and positions are modulated in response to bead position. Feedback is necessary for performing experiments under conditions of constant force, and is thus a standard feature of high-end optical tweezers. We have purchased I/O integration hardware to build a digital bus between our image processing FPGA and our trap control FPGA, which will enable us to synchronize bead position tracking with instrument control for high-speed feedback with microsecond precision. Our goal for this system is to enable nanometer resolution while maintaining feedback rates of 1 kHz or higher. Once realized, this system will be, to our knowledge, the first incidence of a high-bandwidth force clamp by video microscopy. Additionally, this system will enable on-the-fly calibrations of trap stiffness, improving the accuracy of instrument measurements.

Future Experiments and Integration

Full integration of optical trapping with advanced microfluidics has long been sought after in the study of protein-DNA interactions, due to the ability of microfluidics to control and dynamically modify the chemical environment [Grier 2003]. Unfortunately, the physical and optical requirements imposed by the presence of the second objective used to detect trapped particle motion preclude the use of many of the more advanced flow cell types. Designing flow cells that are thin enough to accommodate the short working distances of high-NA objectives, transparent enough to permit high-resolution force and position detection, and compatible with long-term exposure to biological buffers and salt concentrations, is an ongoing challenge in the field [Brewer and Bianco 2008]. Consequently, combinations of optical tweezers and microfluidics either sacrifice functionality of the optical tweezers by eliminating high-resolution detection [Enger et al. 2004], or limit the microfluidic device to one of only a few types and configurations [Gross et al. 2010; Whitesides 2006].

In the near future, we plan to capitalize on our instrument's flexibility in accommodating large and non-transparent sample-side devices by integrating optical trapping of biological constructs with advanced microfluidic flow cells. The instrument opens the door to many flow cell designs and substrates that were previous excluded from viability, potentially making this powerful combination much

easier to realize and easier to work with. We are currently planning studies on transcription and replication that would take advantage of microfluidics to build up more complex protein-DNA systems and measure their behaviors using both high-resolution optical trapping and fluorescence. We additionally have plans to further explore the integration of optical trapping with plasmonic and nanophotonic devices fabricated on silicon.

APPENDIX

Alignment

I: Aligning the Traps to the Objective

Traditional setups are built by modifying a purchased inverted microscope to accommodate the input of a trapping laser. This takes advantage of the stable microscope bodies and state-of-the-art, precisely-aligned optics that already exist in a high-end microscope. The trapping laser need only be aligned to the existing imaging optics through an available microscope port. To ensure the optical trapping plane is co-aligned to the microscope imaging plane, the trapping laser is imaged as it reflects from a coverslip at the objective focal plane, and the laser's collimation is adjusted until its focal spot on the coverslip (and thus the sample plane) is minimized. The iris diaphragms already in place in the microscope body and coaxial with the imaging optics can be used to center the trapping laser to the objective, and various microscope ports provide modular and pre-aligned options for illumination and fluorescence excitation.

Though relatively simple to align, a caveat to this implementation is that the instrument must conform to the structures already in place, and the optical trapping capabilities are thereby made subsidiary to the imaging capabilities for which the microscope was designed. A free-standing optical trapping microscope built entirely from scratch offers tremendous flexibility in implementing specific features and

prioritizing specific aspects of a custom instrument, but presents a more significant challenge to construct and align due to the exponential increase in alignment degrees of freedom. Because no pre-existing reference frame for alignment exists, one must be chosen. We decided to forego a commercial microscope body for this instrument in order to have more flexibility and control in implementing custom features, and so that we could prioritize the optical trapping pathway. Accordingly, we chose the alignment of the trapping laser to our microscope objective as the primary reference point to which all other light pathways would be aligned.

It is important to realize when designing an alignment strategy in a free-standing instrument that any assumptions as to the positions, angles, and alignments of the individual optical elements and their mounting apertures present on the table are dangerous. As an example, we first considered aligning our laser to our objective by using a plumb-line to locate the position on the ceiling co-axial with the objective port as a point of reference. This, however, assumes that the objective holder and its threading are perfectly perpendicular to the ground, which is never the case. Instead, we assembled an alignment apparatus consisting of a pair of iris diaphragms on either end of a 10" lens tube that threads directly into our objective port on one end, and a CCD camera on the other. The diffraction rings that result from the passage of a coherent light source through an aperture are highly sensitive to small changes in the relative beam position and enable very precise alignment. Aligning the trapping laser

at its central deflection angle to this apparatus ensures that the laser will be centered and straight through the objective regardless of how it is positioned relative to the rest of the instrument and its surroundings.

The expanded and collimated trapping laser was first roughly aligned to the centers of the periscope mirrors and to the axis of the objective port before attaching the alignment apparatus. Images of the beam through the apparatus were then acquired via custom LabVIEW software which fits the intensity distributions in X and Y to a Gaussian, and overlays onto the acquired image a fixed marker in a specified position, and a live marker indicating the current Gaussian center. The alignment procedure is as follows:

1. Close the upper iris fully and set the position of the fixed marker to the center of the resulting intensity distribution as indicated by the Gaussian fit.
2. Open the upper iris fully and adjust the periscope stage **translation** until the beam profile is centered on the fixed marker
3. Repeat steps 1 and 2 until the fixed marker and live marker locations converge.
4. Close the bottom iris fully and adjust the **angle** of only the periscope mirror directly under the objective to bring the center of the resulting intensity distribution as indicated by the Gaussian fit to the location of the fixed marker.
5. Open the bottom iris fully and adjust the periscope stage **translation** until the beam is centered on the fixed marker.
6. Repeat steps 1 through 5 until all marker positions converge.

7. Close both irises simultaneously and verify that their resulting diffraction patterns and the beam profile center are all coaxial.

The alignment thus performed, the alignment apparatus was removed and replaced by the microscope objective, and a coverslip was mounted on the microscope sample stage and brought roughly into the objective focal plane. A portion of the trapping laser is reflected back into the trapping objective, and off the top surface of the dichroic mirror into the imaging pathway, and can be used to align the dichroic mirror and imaging pathways to the trapping laser. After adjusting the dichroic mirror angle, the trapping lasers must be re-aligned to the objective with the alignment apparatus, and so the whole process must be repeated iteratively until co-alignment of both optical pathways is achieved. At this point, the position of the focused laser in the microscope sample plane designates the optical center of the system, and can be used as a fixed reference for the alignment of other optical pathways such as illumination and fluorescence excitation.

II: Aligning the Microscope

After the optical traps have been aligned, the next critically important optic to align is the main dichroic mirror (see Figure 2.1), which merges the visible and infrared optical pathways. The dichroic mirror is held in a 3-axis mount which allows for both angular adjustment and translation along the axis parallel to the imaging path.

Visible-wavelength light that leaves the objective is reflected by the main dichroic and then passes through the filter wheel block, which is fixed in height by a machined mount. Being the only optical element in the illumination and imaging paths without an adjustable height, the filter wheel block serves as the second reference point of the microscope behind the objective, and designates the height of the entire illumination and imaging system. The dichroic mirror links the two, and must be freely adjustable in order co-align the system despite the accuracy limitations in the custom-machined mounts.

Notably, the upward facing surface of the main dichroic is coated with an interference film which reflects >95% of wavelengths from 400 – 700 nm and transmits 99.4% of 1064-nm light, while the bottom surface of the dichroic is uncoated. The lower surface thus reflects an order of magnitude more 1064-nm light than the upper dichroic coating, and so the imaging paths of 1064 nm light and visible light are offset from each other vertically. The alignment of the main dichroic mirror is therefore be accomplished in two steps, where first the reflected trapping laser is used to set the dichroic angle and map out the rough imaging path, and then the image of a trapped object is used to set the dichroic axial position and fine-tune the imaging alignment.

Precise alignment of the imaging path is again aided by a pair of irises, one mounted to the front of the microscope camera, and one mounted to the front of the

image-forming lens, and the heights of each are carefully measured and set to the height of the filter wheel block aperture. The camera sensor plane is then fixed at the imaging lens' focal distance by an adjustable-length lens tube. The position of the imaging assembly on the optics table and main dichroic mirror are then adjusted until the image of a trapped bead passes through the centers of the lens iris, the camera iris, and the filter wheel block aperture visible on the periphery of the camera image. The trapping laser collimation can then be fine-tuned if necessary to achieve correct alignment of the trapping plane relative to the imaging plane, after which the laser and imaging paths should be re-aligned.

REFERENCES

Abbondanzieri, E. A., W. J. Greenleaf, J. W. Shaevitz, R. Landick, and S. M. Block

2005 Direct observation of base-pair stepping by RNA polymerase. Nature 438(7067):460-5.

Ahlawat, S., A. Chowdhury, A. Uppal, N. Kumar, and P. K. Gupta

2016 Use of Raman optical tweezers for cell cycle analysis. Analyst 141(4):1339-1346.

Alberts, B., A. Johnson, J. Lewis, D. Morgan, M. Raff, K. Roberts, and P. Walter

2015 Molecular Biology of the Cell, Sixth Edition. Molecular Biology of the Cell, Sixth Edition:1-1342.

Allersma, M. W., F. Gittes, M. J. deCastro, R. J. Stewart, and C. F. Schmidt

1998 Two-dimensional tracking of ncd motility by back focal plane interferometry. Biophysical Journal 74(2):1074-1085.

Alrifaiy, A., J. Borg, O. A. Lindahl, and K. Ramser

2015 A lab-on-a-chip for hypoxic patch clamp measurements combined with optical tweezers and spectroscopy- first investigations of single biological cells. Biomed Eng Online 14:36.

Banfalvi, G.

1994 DNA topology. Biochemical Education 22(2):104.

Barnes, J. A., A. R. Chi, L. S. Cutler, D. J. Healey, D. B. Leeson, T. E. Mcgunigal, J. A. Mullen, W. L. Smith, R. L. Sydnor, R. F. C. Vessot, and G. M. R. Winkler

1971 Characterization of Frequency Stability. Ieee Transactions on Instrumentation and Measurement Im20(2):105-+.

Beese, L. S., and T. A. Steitz

1991 Structural Basis for the 3'-5' Exonuclease Activity of Escherichia-Coli DNA-Polymerase-I - a 2 Metal-Ion Mechanism. Embo Journal 10(1):25-33.

Bennink, M. L., S. H. Leuba, G. H. Leno, J. Zlatanova, B. G. de Grooth, and J. Greve

2001 Unfolding individual nucleosomes by stretching single chromatin fibers with optical tweezers. Nat Struct Biol 8(7):606-10.

Berg-Sorensen, K., L. Oddershede, E. L. Florin, and H. Flyvbjerg

2003 Unintended filtering in a typical photodiode detection system for optical tweezers. Journal of Applied Physics 93(6):3167-3176.

Berg-Sorensen, K., E. J. G. Peterman, T. Weber, C. F. Schmidt, and H. Flyvbjerg

2006 Power spectrum analysis for optical tweezers. II: Laser wavelength dependence of parasitic filtering, and how to achieve high bandwidth. Review of Scientific Instruments 77(6).

Berthelot, J., S. S. Acimovic, M. L. Juan, M. P. Kreuzer, J. Renger, and R. Quidant

2014 Three-dimensional manipulation with scanning near-field optical nanotweezers. Nature Nanotechnology 9(4):295-299.

Biancaniello, P. L., and J. C. Crocker

2006 Line optical tweezers instrument for measuring nanoscale interactions and kinetics. Review of Scientific Instruments 77(11).

Bianco, P. R., L. R. Brewer, M. Corzett, R. Balhorn, Y. Yeh, S. C. Kowalczykowski, and R. J. Baskin

2001 Processive translocation and DNA unwinding by individual RecBCD enzyme molecules. Nature 409(6818):374-8.

Biebricher, A. S., I. Heller, R. F. H. Roijmans, T. P. Hoekstra, E. J. G. Peterman, and G. J. L. Wuite

2015 The impact of DNA intercalators on DNA and DNA-processing enzymes elucidated through force-dependent binding kinetics. Nature Communications 6.

Bird, R. E., K. D. Hardman, J. W. Jacobson, S. Johnson, B. M. Kaufman, S. M. Lee, T. Lee, S. H. Pope, G. S. Riordan, and M. Whitlow

1988 Single-Chain Antigen-Binding Proteins. Science 242(4877):423-426.

Bockelmann, U., B. Essevaz-Roulet, and F. Heslot

1998 DNA strand separation studied by single molecule force measurements. Physical Review E 58(2):2386-2394.

Brau, R. R., P. B. Tarsa, J. M. Ferrer, P. Lee, and M. J. Lang

2006 Interlaced optical force-fluorescence measurements for single molecule biophysics. Biophysical Journal 91(3):1069-1077.

Brennan, L. D., R. A. Forties, S. S. Patel, and M. D. Wang

2016 DNA looping mediates nucleosome transfer. Nature Communications 7.

Brewer, L. R., and P. R. Bianco

2008 Laminar flow cells for single-molecule studies of DNA-protein interactions. Nature Methods 5(6):517-525.

Brinkers, S., H. R. C. Dietrich, F. H. de Groote, I. T. Young, and B. Rieger

2009 The persistence length of double stranded DNA determined using dark field tethered particle motion. Journal of Chemical Physics 130(21).

Brown, Matthew S., and Craig B. Arnold

2010 Fundamentals of Laser-Material Interaction and Application to Multiscale Surface Modification. 135:91-120.

Brunet, A., C. Tardin, L. Salome, P. Rousseau, N. Destainville, and M. Manghi

2016 Dependence of DNA Persistence Length on Ionic Strength of Solutions with Monovalent and Divalent Salts: A Joint Theory-Experiment Study. Biophysical Journal 110(3):403a-403a.

Burger, R., D. Kurzbuch, R. Gorkin, G. Kijanka, M. Glynn, C. McDonagh, and J. Ducree

2015 An integrated centrifugo-opto-microfluidic platform for arraying, analysis, identification and manipulation of individual cells. Lab on a Chip 15(2):378-381.

Butterfield, J., W. L. Hong, L. Mershon, and M. Vershinin

2013 Construction of a High Resolution Microscope with Conventional and Holographic Optical Trapping Capabilities. Jove-Journal of Visualized Experiments (74).

Capitanio, M., R. Cicchi, and F. S. Pavone

2007 Continuous and time-shared multiple optical tweezers for the study of single motor proteins. Optics and Lasers in Engineering 45(4):450-457.

Carter, A. R., G. M. King, and T. T. Perkins

2007 Back-scattered detection provides atomic-scale localization precision, stability, and registration in 3D. Optics Express 15(20):13434-13445.

Casabella, S., P. Scully, N. Goddard, and P. Gardner

2016 Automated analysis of single cells using Laser Tweezers Raman Spectroscopy. Analyst 141(2):689-696.

Chemla, Y. R.

2010 Revealing the base pair stepping dynamics of nucleic acid motor proteins with optical traps. Phys Chem Chem Phys 12(13):3080-95.

Chen, Z. X., X. N. Shan, Y. Guan, S. P. Wang, J. J. Zhu, and N. J. Tao

2015 Imaging Local Heating and Thermal Diffusion of Nanomaterials with Plasmonic Thermal Microscopy. Acs Nano 9(12):11574-11581.

Cheng, W., S. G. Arunajadai, J. R. Moffitt, I. Tinoco, and C. Bustamante

2011 Single-Base Pair Unwinding and Asynchronous RNA Release by the Hepatitis C Virus NS3 Helicase. Science 333(6050):1746-1749.

Comstock, M. J., T. Ha, and Y. R. Chemla

2011 Ultrahigh-resolution optical trap with single-fluorophore sensitivity. Nature Methods 8(4):335-U82.

Comstock, M. J., T. Ha, and Y. R. Chemla

2011 Ultrahigh-resolution optical trap with single-fluorophore sensitivity. Nature Methods 8(4):335-40.

Cooper, G.M.

2014 The Cell: A Molecular Approach. Sixth Edition. By Geoffrey M. Cooper and Robert E. Hausman. Sunderland (Massachusetts): Sinauer Associates. $142.95. xxv + 832 p.; ill.; index. ISBN: 978-0-87893-964-0. [A Companion Website is available.] 2013. The Quarterly Review of Biology 89(4):399-399.

Czerwinski, F., A. C. Richardson, and L. B. Oddershede

2009 Quantifying Noise in Optical Tweezers by Allan Variance. Optics Express 17(15):13255-13269.

Daly, M., V. G. Truong, and S. N. Chormaic

2016 Evanescent field trapping of nanoparticles using nanostructured ultrathin optical fibers. Optics Express 24(13):14470-14482.

Dylla-Spears, R., J. E. Townsend, L. L. Sohn, L. Jen-Jacobson, and S. J. Muller

2009 Fluorescent marker for direct detection of specific dsDNA sequences. Anal Chem 81(24):10049-54.

Ebert, S., K. Travis, B. Lincoln, and J. Guck

2007 Fluorescence ratio thermometry in a microfluidic dual-beam laser trap. Optics Express 15(23):15493-15499.

Enger, J., M. Goksor, K. Ramser, P. Hagberg, and D. Hanstorp

2004 Optical tweezers applied to a microfluidic system. Lab on a Chip 4(3):196-200.

Friese, M. E., H. Rubinsztein-Dunlop, N. R. Heckenberg, and E. W. Dearden

1996 Determination of the force constant of a single-beam gradient trap by measurement of backscattered light. Appl Opt 35(36):7112-6.

Fuller, D. N., G. J. Gemmen, J. P. Rickgauer, A. Dupont, R. Millin, P. Recouvreux, and D. E. Smith

2006 A general method for manipulating DNA sequences from any organism with optical tweezers. Nucleic Acids Research 34(2).

Gibson, G. M., J. Leach, S. Keen, A. J. Wright, and M. J. Padgett

2008 Measuring the accuracy of particle position and force in optical tweezers using high-speed video microscopy. Optics Express 16(19):14561-14570.

Gittes, F., and C. F. Schmidt

1998 Interference model for back-focal-plane displacement detection in optical tweezers. Optics Letters 23(1):7-9.
Govorov, A. O., and H. H. Richardson

2007 Generating heat with metal nanoparticles. Nano Today 2(1):30-38.
Grier, D. G.

2003 A revolution in optical manipulation. Nature 424(6950):810-816.
Gross, P., G. Farge, E. J. G. Peterman, and G. J. L. Wuite

2010 Combining Optical Tweezers, Single-Molecule Fluorescence Microscopy, and Microfluidics for Studies of DNA-Protein Interactions. Methods in Enzymology, Vol 475: Single Molecule Tools, Pt B 475:427-453.
Gusachenko, I., M. C. Frawley, V. G. Truong, and S. N. Chormaic

2014 Optical nanofiber integrated into an optical tweezers for particle manipulation and in-situ fiber probing. Optical Trapping and Optical Micromanipulation Xi 9164.
Hall, M. A., A. Shundrovsky, L. Bai, R. M. Fulbright, J. T. Lis, and M. D. Wang

2009 High-resolution dynamic mapping of histone-DNA interactions in a nucleosome. Nat Struct Mol Biol 16(2):124-9.
Heller, I., G. Sitters, O. D. Broekmans, G. Farge, C. Menges, W. Wende, S. W. Hell, E. J. G. Peterman, and G. J. L. Wuite

2013 STED nanoscopy combined with optical tweezers reveals protein dynamics on densely covered DNA. Nature Methods 10(9):910-U132.
Hinterdorfer, Peter, and Antoine Van Oijen

2009 Handbook of single-molecule biophysics: Springer Science & Business Media.
Huhle, A., D. Klaue, H. Brutzer, P. Daldrop, S. Joo, O. Otto, U. F. Keyser, and R. Seidel

2015 Camera-based three-dimensional real-time particle tracking at kHz rates and Angstrom accuracy. Nature Communications 6.
Huisstede, J. H. G., K. O. van der Werf, M. L. Bennink, and V. Subramaniam

2005 Force detection in optical tweezers using backscattered light. Optics Express 13(4):1113-1123.
Ingram, J. C., K. W. Nebesny, and J. E. Pemberton

1990 Optical-Constants of the Noble-Metals Determined by Reflection Electron-Energy Loss Spectroscopy. Applied Surface Science 44(4):293-300.
Inman, J., S. Forth, and M. D. Wang

2010 Passive torque wrench and angular position detection using a single-beam optical trap. Opt Lett 35(17):2949-51.
Inman, J. T., B. Y. Smith, M. A. Hall, R. A. Forties, J. Jin, J. P. Sethna, and M. D. Wang

2014 DNA Y structure: a versatile, multidimensional single molecule assay. Nano Lett 14(11):6475-80.
Ishijima, A., H. Kojima, T. Funatsu, M. Tokunaga, H. Higuchi, H. Tanaka, and T. Yanagida

1998 Simultaneous observation of individual ATPase and mechanical events by a single myosin molecule during interaction with actin. Cell 92(2):161-171.
Jannasch, A., A. F. Demirors, P. D. J. van Oostrum, A. van Blaaderen, and E. Schaffer

2012 Nanonewton optical force trap employing anti-reflection coated, high-refractive-index titania microspheres. Nature Photonics 6(7):469-473.
Jing, P. F., J. D. Wu, G. W. Liu, E. G. Keeler, S. H. Pun, and L. Y. Lin

2016 Photonic Crystal Optical Tweezers with High Efficiency for Live Biological Samples and Viability Characterization. Scientific Reports 6.
Johnson, D. S., L. Bai, B. Y. Smith, S. S. Patel, and M. D. Wang

2007 Single-molecule studies reveal dynamics of DNA unwinding by the ring-shaped T7 helicase. Cell 129(7):1299-309.
Joo, C., H. Balci, Y. Ishitsuka, C. Buranachai, and T. Ha

2008 Advances in single-molecule fluorescence methods for molecular biology. Annual Review of Biochemistry 77:51-76.
Juan, M. L., M. Righini, and R. Quidant

2011 Plasmon nano-optical tweezers. Nature Photonics 5(6):349-356.
Karstens, T., and K. Kobs

1980 Rhodamine-B and Rhodamine-101 as Reference Substances for Fluorescence Quantum Yield Measurements. Journal of Physical Chemistry 84(14):1871-1872.
Kato, A., P. S. Albert, J. M. Vega, and J. A. Birchler

2006 Sensitive fluorescence in situ hybridization signal detection in maize using directly labeled probes produced by high concentration DNA polymerase nick translation. Biotechnic & Histochemistry 81(2-3):71-78.
Keen, S., J. Leach, G. Gibson, and M. J. Padgett

2007 Comparison of a high-speed camera and a quadrant detector for measuring displacements in optical tweezers. Journal of Optics a-Pure and Applied Optics 9(8):S264-S266.

Kessler, C.

1991 The Digoxigenin-Anti-Digoxigenin (Dig) Technology - a Survey on the Concept and Realization of a Novel Bioanalytical Indicator System. Molecular and Cellular Probes 5(3):161-205.

Keyser, U. F., B. N. Koeleman, S. Van Dorp, D. Krapf, R. M. M. Smeets, S. G. Lemay, N. H. Dekker, and C. Dekker

2006 Direct force measurements on DNA in a solid-state nanopore. Nature Physics 2(7):473-477.

Keyser, U. F., J. van der Does, C. Dekker, and N. H. Dekker

2006 Optical tweezers for force measurements on DNA in nanopores. Review of Scientific Instruments 77(10).

Killian, J. L., M. Li, M. Y. Sheinin, and M. D. Wang

2012 Recent advances in single molecule studies of nucleosomes. Curr Opin Struct Biol 22(1):80-7.

Knauert, M. P., and P. M. Glazer

2001 Triplex forming oligonucleotides: sequence-specific tools for gene targeting. Hum Mol Genet 10(20):2243-51.

Koch, S. J., A. Shundrovsky, B. C. Jantzen, and M. D. Wang

2002 Probing protein-DNA interactions by unzipping a single DNA double helix. Biophys J 83(2):1098-105.

La Porta, A., and M. D. Wang

2004 Optical torque wrench: angular trapping, rotation, and torque detection of quartz microparticles. Phys Rev Lett 92(19):190801.

Landenberger, B., H. Hofemann, S. Wadle, and A. Rohrbach

2012 Microfluidic sorting of arbitrary cells with dynamic optical tweezers. Lab on a Chip 12(17):3177-3183.

Lansdorp, B. M., and O. A. Saleh

2012 Power spectrum and Allan variance methods for calibrating single-molecule video-tracking instruments. Review of Scientific Instruments 83(2).

Lansdorp, B. M., S. J. Tabrizi, A. Dittmore, and O. A. Saleh

2013 A high-speed magnetic tweezer beyond 10,000 frames per second. Review of Scientific Instruments 84(4).

Lee, S., and S. Hohng

2013 An Optical Trap Combined with Three-Color FRET. Journal of the American Chemical Society 135(49):18260-18263.

Lin, X.E.

1999 Laser Pulse Heating. Particle Accelerator Conference, New York, 1999, pp. 1429-1431.

Linpinsel, J. L., and G. L. Conn

2012 General protocols for preparation of plasmid DNA template, RNA in vitro transcription, and RNA purification by denaturing PAGE. Methods Mol Biol 941:43-58.

Liu, Y., D. K. Cheng, G. J. Sonek, M. W. Berns, C. F. Chapman, and B. J. Tromberg

1995 Evidence for Localized Cell Heating Induced by Infrared Optical Tweezers. Biophysical Journal 68(5):2137-2144.

Lou, J. F., T. M. Finegan, P. Mohsen, T. A. Hatton, and P. E. Laibinis

1999 Fluorescence-based thermometry: Principles and applications. Reviews in Analytical Chemistry 18(4):235-284.

Ma, J., L. Bai, and M. D. Wang

2013 Transcription Under Torsion. Science 340(6140):1580-1583.

Malagnino, N., G. Pesce, A. Sasso, and E. Arimondo

2002 Measurements of trapping efficiency and stiffness in optical tweezers. Optics Communications 214(1-6):15-24.

Mangeol, P., and U. Bockelmann

2008 Interference and crosstalk in double optical tweezers using a single laser source. Review of Scientific Instruments 79(8).

Manning, G. S.

2006 The persistence length of DNA is reached from the persistence length of its null isomer through an internal electrostatic stretching force. Biophysical Journal 91(10):3607-3616.

Marko, J. F., and E. D. Siggia

1995 Stretching DNA. Macromolecules 28(26):8759-8770.

Mehta, A. D., R. S. Rock, M. Rief, J. A. Spudich, M. S. Mooseker, and R. E. Cheney

1999 Myosin-V is a processive actin-based motor. Nature 400(6744):590-3.

Meiners, J. C., and S. R. Quake

1999 Direct measurement of hydrodynamic cross correlations between two particles in an external potential. Physical Review Letters 82(10):2211-2214.

Millen, J., T. Deesuwan, P. Barker, and J. Anders

2014 Nanoscale temperature measurements using non-equilibrium Brownian dynamics of a levitated nanosphere. Nature Nanotechnology 9(6):425-429.
Moffitt, J. R., Y. R. Chemla, D. Izhaky, and C. Bustamante

2006 Differential detection of dual traps improves the spatial resolution of optical tweezers. Proc Natl Acad Sci U S A 103(24):9006-11.
Moffitt, J. R., Y. R. Chemla, S. B. Smith, and C. Bustamante

2008 Recent advances in optical tweezers. Annual Review of Biochemistry 77:205-228.
Molloy, J. E.

1998 Optical chopsticks: Digital synthesis of multiple optical traps. Methods in Cell Biology, Vol 55 55:205-216.
Natrajan, V. K., and K. T. Christensen

2009 Two-color laser-induced fluorescent thermometry for microfluidic systems. Measurement Science and Technology 20(1).
Neuman, K. C., and S. M. Block

2004 Optical trapping. Review of Scientific Instruments 75(9):2787-2809.
Neuman, K. C., and A. Nagy

2008 Single-molecule force spectroscopy: optical tweezers, magnetic tweezers and atomic force microscopy. Nature Methods 5(6):491-505.
Otto, O., F. Czerwinski, J. L. Gornall, G. Stober, L. B. Oddershede, R. Seidel, and U. F. Keyser

2010 Real-time particle tracking at 10,000 fps using optical fiber illumination. Optics Express 18(22):22722-22733.
Otto, O., J. L. Gornall, G. Stober, F. Czerwinski, R. Seidel, and U. F. Keyser

2011 High-speed video-based tracking of optically trapped colloids. Journal of Optics 13(4).
Pattani, V. P., and J. W. Tunnell

2012 Nanoparticle-mediated photothermal therapy: a comparative study of heating for different particle types. Lasers Surg Med 44(8):675-84.
Perkins, T. T., S. R. Quake, D. E. Smith, and S. Chu

1994 Relaxation of a single DNA molecule observed by optical microscopy. Science 264(5160):822-6.
Peterman, E. J. G., F. Gittes, and C. F. Schmidt

2003 Laser-induced heating in optical traps. Biophysical Journal 84(2):1308-1316.

Polyanskiy, M.N.

2016 Refractive index database, Vol. 2016.

Rigby, P. W., M. Dieckmann, C. Rhodes, and P. Berg

1977 Labeling deoxyribonucleic acid to high specific activity in vitro by nick translation with DNA polymerase I. J Mol Biol 113(1):237-51.

Roche, P. J.

2006 Preparation of template DNA and labeling techniques. Methods Mol Biol 326:9-16.

Roy, R., S. Hohng, and T. Ha

2008 A practical guide to single-molecule FRET. Nature Methods 5(6):507-16.

Shivashankar, G. V., G. Stolovitzky, and A. Libchaber

1998 Backscattering from a tethered bead as a probe of DNA flexibility. Applied Physics Letters 73(3):291-293.

Sischka, A., C. Kleimann, W. Hachmann, M. M. Schafer, I. Seuffert, K. Tonsing, and D. Anselmetti

2008 Single beam optical tweezers setup with backscattered light detection for three-dimensional measurements on DNA and nanopores. Rev Sci Instrum 79(6):063702.

Sischka, A., C. Kleimann, W. Hachmann, M. M. Schafer, I. Seuffert, K. Tonsing, and D. Anselmetti

2008 Single beam optical tweezers setup with backscattered light detection for three-dimensional measurements on DNA and nanopores. Review of Scientific Instruments 79(6).

Sizer, I. W.

1943 Effects of temperature on enzyme kinetics. Advances in Enzymology and Related Subjects of Biochemistry 3:35-62.

Soltani, M., J. Lin, R. A. Forties, J. T. Inman, S. N. Saraf, R. M. Fulbright, M. Lipson, and M. D. Wang

2014 Nanophotonic trapping for precise manipulation of biomolecular arrays. Nat Nanotechnol 9(6):448-52.

Soni, G. V., F. M. Hameed, T. Roopa, and G. V. Shivashankar

2002 Development of an optical tweezer combined with micromanipulation for DNA and protein nanobioscience. Current Science 83(12):1464-1470.

Sparks, M.

1976 Theory of Laser-Heating of Solids - Metals. Journal of Applied Physics 47(3):837-849.

Stock, K. D., and R. Heine

2000 Spectral characterization of InGaAs trap detectors and photodiodes used as transfer standards. Metrologia 37(5):449-452.

Svoboda, K., C. F. Schmidt, B. J. Schnapp, and S. M. Block

1993 Direct observation of kinesin stepping by optical trapping interferometry. Nature 365(6448):721-7.

Tasara, T., B. Angerer, M. Damond, H. Winter, S. Dorhofer, U. Hubscher, and M. Amacker

2003 Incorporation of reporter molecule-labeled nucleotides by DNA polymerases. II. High-density labeling of natural DNA. Nucleic Acids Research 31(10):2636-2646.

Thalhammer, G., C. McDougall, M. P. MacDonald, and M. Ritsch-Marte

2016 Acoustic force mapping in a hybrid acoustic-optical micromanipulation device supporting high resolution optical imaging. Lab on a Chip 16(8):1523-32.

Towrie, M., S. W. Botchway, A. Clark, E. Freeman, R. Halsall, A. W. Parker, M. Prydderch, R. Turchetta, A. D. Ward, and M. R. Pollard

2009 Dynamic position and force measurement for multiple optically trapped particles using a high-speed active pixel sensor. Review of Scientific Instruments 80(10).

van der Horst, A., and N. R. Forde

2010 Power spectral analysis for optical trap stiffness calibration from high-speed camera position detection with limited bandwidth. Opt Express 18(8):7670-7.

van Loenhout, M. T. J., I. De Vlaminck, B. Flebus, J. F. den Blanken, L. P. Zweifel, K. M. Hooning, J. W. J. Kerssemakers, and C. Dekker

2013 Scanning a DNA Molecule for Bound Proteins Using Hybrid Magnetic and Optical Tweezers. Plos One 8(6).

van Loenhout, M. T. J., J. W. J. Kerssemakers, I. De Vlaminck, and C. Dekker

2012 Non-Bias-Limited Tracking of Spherical Particles, Enabling Nanometer Resolution at Low Magnification. Biophysical Journal 102(10):2362-2371.

van Rosmalen, M. G. M., A. S. Biebricher, D. Kamsma, A. Zlotnick, G. J. L. Wuite, and W. H. Roos

2015 DNA-Induced Viral Assembly Studied in Real-Time by Optical Tweezers, Acoustic Force Spectroscopy and Atomic Force Microscopy. Biophysical Journal 108(2):170a-170a.

Vanvliet, C. M., and P. H. Handel

1982 A New Transform Theorem for Stochastic-Processes with Special Application to Counting Statistics. Physica A 113(1-2):261-276.

Vetrone, F., R. Naccache, A. Zamarron, A. J. de la Fuente, F. Sanz-Rodriguez, L. M. Maestro, E. M. Rodriguez, D. Jaque, J. G. Sole, and J. A. Capobianco

2010 Temperature Sensing Using Fluorescent Nanothermometers. Acs Nano 4(6):3254-3258.

Virulh Sa-yakanit, Ed, Leif Ed Matsson, and Hans Ed Frauenfelder

2000 Proceedings of the first workshop on biological physics 2000: World Scientific Publishing.

Visscher, K., S. P. Gross, and S. M. Block

1996 Construction of multiple-beam optical traps with nanometer-resolution position sensing. Ieee Journal of Selected Topics in Quantum Electronics 2(4):1066-1076.

Volpe, G., G. Kozyreff, and D. Petrov

2007 Backscattering position detection for photonic force microscopy. Journal of Applied Physics 102(8).

Wang, J., E. Palecek, P. E. Nielsen, G. Rivas, X. H. Cai, H. Shiraishi, N. Dontha, D. B. Luo, and P. A. M. Farias

1996 Peptide nucleic acid probes for sequence-specific DNA biosensors. Journal of the American Chemical Society 118(33):7667-7670.

Wang, M. D., M. J. Schnitzer, H. Yin, R. Landick, J. Gelles, and S. M. Block

1998 Force and velocity measured for single molecules of RNA polymerase. Science 282(5390):902-7.

Wang, M. D., H. Yin, R. Landick, J. Gelles, and S. M. Block

1997 Stretching DNA with optical tweezers. Biophysical Journal 72(3):1335-1346.

Wang, M. D., H. Yin, R. Landick, J. Gelles, and S. M. Block

1997 Stretching DNA with optical tweezers. Biophys J 72(3):1335-46.

Weber, P. C., D. H. Ohlendorf, J. J. Wendoloski, and F. R. Salemme

1989 Structural Origins of High-Affinity Biotin Binding to Streptavidin. Science 243(4887):85-88.

Whitesides, G. M.

2006 The origins and the future of microfluidics. Nature 442(7101):368-373.
Woerdemann, Mike

2012 Structured light fields : applications in optical trapping, manipulation, and organisation.
Xie, C., M. A. Dinno, and Y. Q. Li

2002 Near-infrared Raman spectroscopy of single optically trapped biological cells. Opt Lett 27(4):249-51.
Yang, A. H., S. D. Moore, B. S. Schmidt, M. Klug, M. Lipson, and D. Erickson

2009 Optical manipulation of nanoparticles and biomolecules in sub-wavelength slot waveguides. Nature 457(7225):71-5.
Yanisch-Perron, C., J. Vieira, and J. Messing

1985 Improved M13 phage cloning vectors and host strains: nucleotide sequences of the M13mp18 and pUC19 vectors. Gene 33(1):103-19.
Ye, F., R. P. Badman, J. T. Inman, M. Soltani, J. L. Killian, and M. D. Wang

2016 Biocompatible and High Stiffness Nanophotonic Trap Array for Precise and Versatile Manipulation. Nano Letters 16(10):6661-6667.
Yin, H., M. D. Wang, K. Svoboda, R. Landick, S. M. Block, and J. Gelles

1995 Transcription against an applied force. Science 270(5242):1653-7.
Zhang, Y., K. J. Liu, T. L. Wang, I. M. Shih, and T. H. Wang

2012 Mapping DNA Quantity into Electrophoretic Mobility through Quantum Dot Nanotethers for High-Resolution Genetic and Epigenetic Analysis. Acs Nano 6(1):858-864.
Zhu, Z. R., J. Chao, H. Yu, and A. S. Waggoner

1994 Directly Labeled DNA Probes Using Fluorescent Nucleotides with Different Length Linkers. Nucleic Acids Research 22(16):3418-3422.
Zhu, Z. R., and A. S. Waggoner

1997 Molecular mechanism controlling the incorporation of fluorescent nucleotides into DNA by PCR. Cytometry 28(3):206-211.
Zohar, H., and S. J. Muller

2011 Labeling DNA for single-molecule experiments: methods of labeling internal specific sequences on double-stranded DNA. Nanoscale 3(8):3027-39.